Materials Today: Proceedings 42 (2021) 2656–2659

Contents lists available at ScienceDirect

Materials Today: Proceedings

journal homepage: www.elsevier.com/locate/matpr

Recovery of copper from Waste PCB boards using electrolysis

Sourav Choubey [a], Prerna Goswami [a], Shina Gautam [b]

[a] Institute of Chemical Technology, Matunga, Mumbai, India
[b] Shroff S.R. Rotary Institute of Chemical Technology, Ankleshwar, India

ARTICLE INFO

Article history:
Available online 2 February 2021

Keywords:
E-Waste
Electrolysis
Metal extraction

ABSTRACT

Utilizing Electrical and Electronic products has imbibed into the habitual activity of every human being. This has lead to the increase in the yield of E-Waste. Due to the Existence of toxic substances in E-Waste, it needs to be handled carefully as it has adverse impact on the environment. The improper disposal of Electrical and Electronic Waste has caused some metals to accumulate in the air which degrades the atmosphere. Hence proper disposal or recycling of the scrapped Electrical and Electronic products is mandatory and of major concern for research. The E-Waste contains several materials like Gold, Silver, Copper, Iron. . .etc. Extraction of all these metals from the scrapped electrical and Electronic Products in an environment friendly manner is of utmost importance. Electro chemical, Pyrometallurgical, Hydrometallurgical and Bioleaching are the most efficient methods to extract metals. The principal metal present in the scraped electronic products is copper. In this research work, printed circuit boards of Desktop Computers are used to extract metals from them. The electrolysis process is carried out with selective anode and cathode to extract copper from it. The current density is optimized to get maximum extraction efficiency of copper.

Selection and peer-review under responsibility of the scientific committee of the 3rd International Conference on Materials Engineering & Science.

1. Introduction

Advancement in technology has triggered the habit of people to quickly adopt the new things over the old ones which indeed accelerates the generation of E-Waste. 53.6 Mt of E-Waste has been generated globally in 2019 and it is estimated to go up to 74.7 Mt by 2030 [1]. Soaring generation of E-Waste has waved way to the demand of proper disposal of the Waste. In several countries E-Waste is dealt with incineration, landfilling, blazing and junking in the open atmosphere [2]. These improper handling of waste has given rise to the destructive Environmental impacts due to the Presence of several heavy metals in the E-Waste [3]. Polybrominated diphenyl ethers (PBDEs, tri-to hepta-BDEs) and Dechlorane Plus (DP) were found in several samples of Soil, Sediments and Road dust in Guiyu, an E-Waste recycling town of China [4]. The bleak outcome of the presence of PBDE and DP in environment [5] is the damaging effect it causes on the overall health which cannot be disregarded.

The E-Waste contains several metals which includes some precious metals like Au, Ag and Pd. Extraction of these metals not only upgrades the issue of environment but also replenishes the natural resources and boosts the economy. The collected scrap Electrical and Electronic products from industries as well as domestic consumers should undergo pretreatment process before being used for the extraction of metals. The Pretreatment process includes Manual Desegregation, Dismantling, Shredding and crushing. Fig. 1 **(a)** Shows the Pretreatment Process of E-Waste. Dismantling is done at the dismantling temperature of 180 °C. The component wise extraction of metal can be done to get more extraction efficiency of the metal [6–8]. After the dismantling process components can be segregated according to the metals to be recovered. The scrapped PCB Boards or Components is grinded to the size of (1–2) mm by Shredding and Crushing processes [9].

In the past and recent researches, several methods have been applied to extract metals from E-Waste. Some of these methods being used for the metal extraction are Electro chemical, Pyrometallurgical, Hydrometallurgical and Bioleaching [10–12] as shown in Fig. 1 **(b).** Several researches have been done to extract metals from Grinded Metal powder using the above mentioned process amongst which the highest extraction efficiency recorded is by Electrolysis process [13–15].

https://doi.org/10.1016/j.matpr.2020.12.596
2214-7853/
Selection and peer-review under responsibility of the scientific committee of the 3rd International Conference on Materials Engineering & Science.

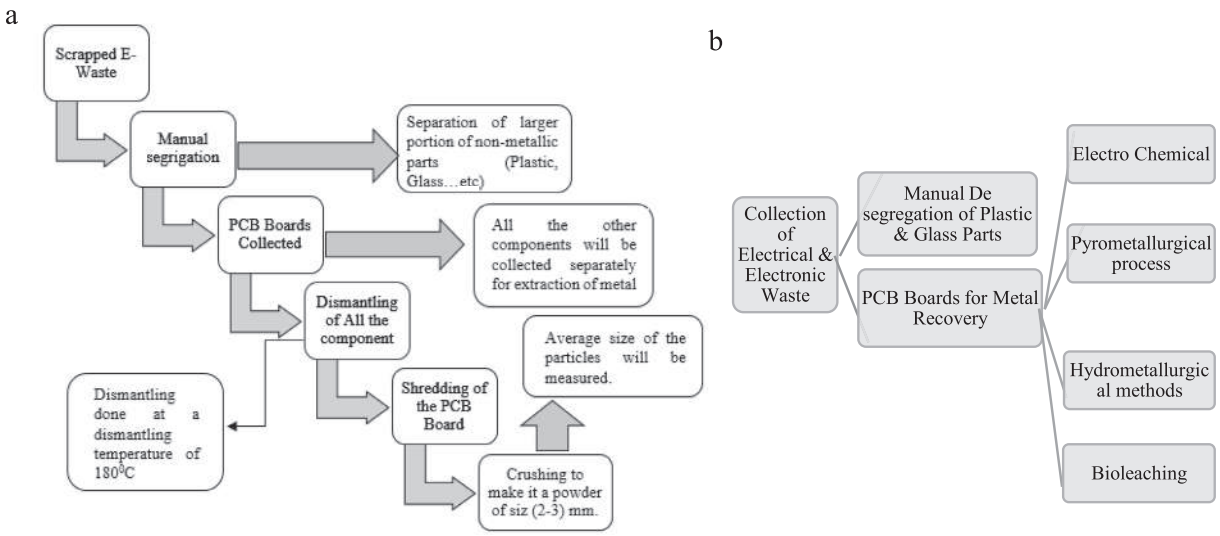

Fig. 1. (a) Pretreatment process of E-Waste (b) Methods of Metal Extraction.

2. Material and process

2.1. Separation of Plastic and metal

The grinded E-Waste powder contains Plastic, ferrous and non-ferrous metals. Density separation method [16] is used to separate the Metallic and nonmetallic parts. For separation of ferrous and nonferrous metals Electromagnetic separator [17] is used. After segregation of ferrous and nonferrous metal powders, the metal powder is selected based on the metals to be extracted. In this research work nonferrous metal powder was selected for recovery of copper.

2.2. Sample preparation

For experimental purpose 8 gm of nonferrous metal was taken. The metal powder was dissolved into H_2SO_4 and stirred at 80 °C temperature for 4 h. The solution was filtered and 40 ml of aquaregia (30 ml HCl and 10 ml HNO_3) was added to the filtered solution. The solution was stirred for 60 min at a temperature of 80 °C. The Atomic absorption spectrometry (AAS) analysis was done for the solution. The following reaction took place:

$$HNO_{3\,(aq)} + 3\,HCl_{\,(aq)} \rightarrow NOCl_{\,(g)} + Cl_{2\,(g)} + 2\,H_2O \quad \text{(i)}$$

$$H_2SO_4 + HCl \rightarrow H_2O + Cl_2 + SO_2 \quad \text{(ii)}$$

$$Cu + Cl_2 \rightarrow CuCl_2 \quad \text{(iii)}$$

$$CuCl_2 + H_2SO_4 \rightarrow CuSO_4 + HCl \quad \text{(iv)}$$

2.3. Electrolysis

The sample was taken for electrolysis. To extract Cu from the solution, electrolysis process was carried out in a cubic reactor of size 12 cm × 8 cm × 7 cm as shown in Fig. 2. Iron Anode and Copper cathode were used for electrolysis. The anode and cathode chambers were separated by an anti-acid filter cloth [8]. The calculated cell potential was maintained for the experimental analysis.

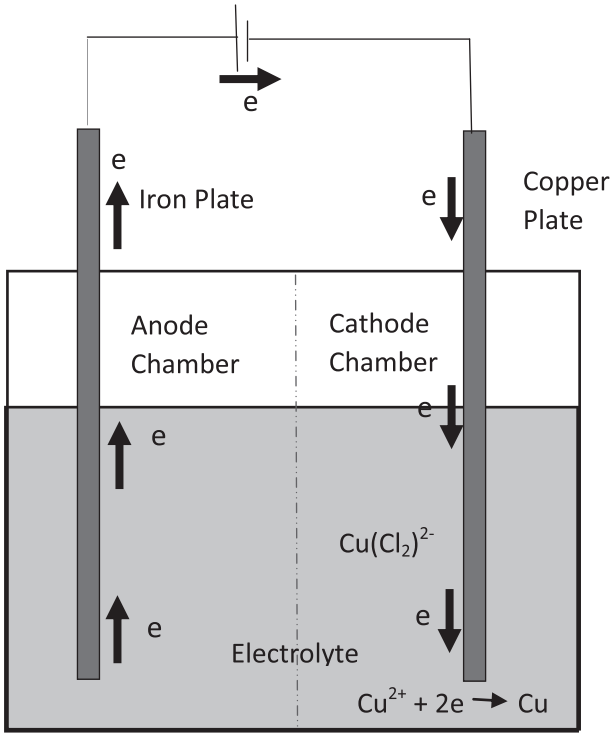

Fig. 2. Electrolysis Process.

3. Analysis and calculations

3.1. Sample Analysis

AAS Analysis for six metals were done for the all the samples. The Analysis report shown in the Table 1.

As shown in Table 1. The initial sample contains 7186 mg/L of Cu whereas the rest of the elements are less as compared to Cu. After the separation and acid leaching process the sample contained 6838.51 mg/L of Cu. The electrolysis process was carried out at Cu recovery potential for 30 min. The remaining electrolyte was tested and 6725.55 mg/L of copper was recovered from it. The sticky metal powders accumulated at the cathode were collected

Table 1
AAS Analysis of samples.

SR.NO.	SAMPLE ID	COPPER	ZINC	CHRMOIUM	NICKEL	LEAD	IRON
UNIT		mg/L	mg/L	mg/L	mg/L	mg/L	mg/L
1	A	7186	112.45	BDL	261.48	292.02	863.64
2	B	6838.51	82.39	BDL	218.6	28.43	26.44
3	C	112.96	5.07	0.2056	1.3	5.29	19.34

Where
A: Initial E-Waste Sample
B: Sample before Electrolysis
C: Sample after Electrolysis
BDL: Below the Detection Limit

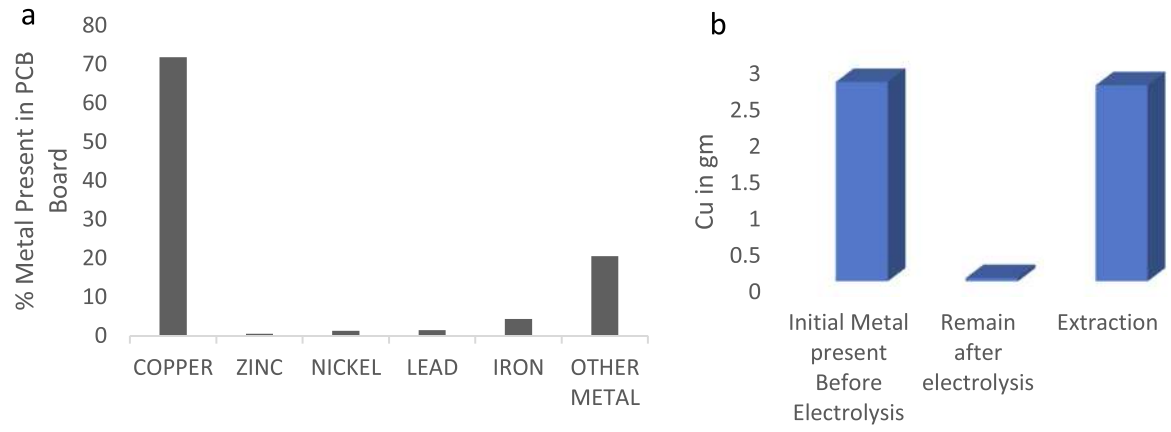

Fig. 3. (a) % of Metal Present in PCB Board (b) Metal Extraction from initial to final after electrolysis.

and washed. After the AAS Analysis of the extracted metal powder it was confirmed that the extracted metal was Cu powder.

3.2. Calculations

The Extraction rate of metals can be calculated using the following formula

- % E = (X – Y) / X × 100 %

  Where,

  E = % Metal Extraction Efficiency
  X = Initial Metal Present in the sample (gm)
  Y = After Electrolysis metal present (gm) in the electrolyte
- From the above formula it is observed that the Cu recovery in this case is 98%. The extracted copper is collected from the cathode chamber.

It is evident from Fig. 3 **(a)** that the presence of Cu is high in Printed circuit Board which is approximately around 70%. The composition of Cu in the sample is high as compared to other metals. The initial amount of Cu present in PCB Board was 2.874 gm out of which 2.69 gm was extracted and 0.05 gm remained as shown in the Fig. 3(b).

4. Effect of pH in electrolysis

As the electrolyte contains several concentrated acidic solution so the pH is a great factor to be considered. The pH must be maintained between 2 and 3 for the electrolysis so that the recovery efficiency is maximum. NaOH is added to the solution to maintain the pH at the desirable limit.

5. Conclusion

Existence of copper is at the higher side in PCB Board compared to the other elements. It is always preferable to consider the selective components for the selective separation of a metal for getting better extraction rate. The preparation of electrolyte is paramount for the extraction. pH for the electrolyte should be between 2 and 3. Electrodes needs to be selected considering the metal to be extracted. The Cell potential has to maintained throughout the electrolysis process.

CRediT authorship contribution statement

Sourav Choubey: Conceptualization, Methodology, Formal analysis, Writing - original draft. **Prerna Goswami:** Supervision, Writing - review & editing, Visualization. **Shina Gautam:** Supervision.

Declaration of Competing Interest

The authors declare that they have no known competing financial interests or personal relationships that could have appeared to influence the work reported in this paper.

References

[1] V. Forti, C.P. Baldé, R. Kuehr, G. Bel. The Global E-Waste Monitor 2020: Quantities, flows and the circular economy potential, International Telecommunication Union (ITU) and International Solid Waste Association (ISWA), Bonn/Geneva/Rotterdam, 2020.
[2] J. Ruan, Z. Xu, Constructing environment-friendly return road of metals from e-waste: Combination of physical separation technologies, Renew. Sustain. Energy Rev. 54 (2016) 745–760.
[3] G.H. Xing, J.K.Y. Chan, A.O.W. Leung, S.C. Wu, M.H. Wong, Environmental impact and human exposure to PCBs in Guiyu, an electronic waste recycling site in China, Environ. Int. 35 (1) (2009) 76–82.

[4] N.a. Li, X.-W. Chen, W.-J. Deng, J.P. Giesy, H.-L. Zheng, PBDEs and Dechlorane Plus in the environment of Guiyu, Southeast China: A historical location for E-waste recycling (2004, 2014), Chemosphere 199 (2018) 603–611.
[5] M. Sorais, M.J. Mazerolle, J.-F. Giroux, J. Verreault, Landfills represent significant atmospheric sources of exposure to halogenated flame retardants for urban-adapted gulls, Environ. Int. 135 (2020) 105387.
[6] J. Cui, H.J. Roven, Chapter 20- Electronic Waste, Waste A handbook for Management, 2011, Pages 281-296.
[7] X. Yi, Y. Qi, F. Li, J. Shu, Z. Sun, S. Sun, M. Chen, S. Pu, Effect of electrolyte reuse on metal recovery from waste CPU slots by slurry electrolysis, Waste Manage. 95 (2019) 370–376.
[8] F. Li, M. Chen, J. Shu, M. Shirvani, Y. Li, Z. Sun, S. Sun, Z. Xu, K. Fu, S. Chen, Copper and gold recovery from CPU sockets by one-step slurry electrolysis, J. Cleaner Prod. 213 (2019) 673–679.
[9] C.D. Tran, S.P. Salhofer Process in informal end-processing of E-Waste generated from personal computers in Vietnam, Journal of Material Cycles and Waste Management volume 20, pages1154–1178(2018).
[10] S. Sthiannopkao, M.H. Wong, Handling E-Waste in developed and developing countries: initiatives, practices, and consequences, Sci. Total Environ. 463–464 (2013) 1147–1153.
[11] D. Kaliyaraj, M. Rajendran, V. Angamuthu, A.R. Antony, M. Kaari, S. Thangavel, G. Venugopal, J. Joseph, R. Manikkam, Bioleaching of heavy metals from printed circuit board (PCB) by Streptomyces albidoflavus TN10 isolated from insect nest, Bioresour. Bioprocess. 6 (1) (2019), https://doi.org/10.1186/s40643-019-0283-3.
[12] W. Liu, J. Xu, J. Han, F. Jiao, W. Qin, Z. Li, Kinetic and Mechanism Studies on Pyrolysis of Printed Circuit Boards in the Absence and Presence of Copper, ACS Sustainable Chem. Eng. 7 (2) (2019) 1879–1889.
[13] X. Liu, Q. Tan, Y. Li, Z. Xu, M. Chen, Copper recovery from waste printed circuit boards concentrated metal scraps by electrolysis, Front. Environ. Sci. Eng. 11 (5) (2017).
[14] D. Yang, Y. Chu, J. Wang, M. Chen, J. Shu, F. Xiu, Z. Xu, S. Sun, S. Chen, Completely separating metals and nonmetals from waste printed circuit boards by slurry electrolysis, Sep. Purif. Technol. 205 (2018) 302–307.
[15] S. Zhang, Y. Li, R. Wang, Z. Xu, B. Wang, S. Chen, M. Chen, Superfine copper powders recycled from concentrated metal scraps of waste printed circuit boards by slurry electrolysis, J. Cleaner Prod. 152 (2017) 1–6.
[16] M. Bauer, M. Lehner, D. Schwabl, H. Flachberger, L. Kranzinger, R. Pomberger, W. Hofer, Sink–float density separation of post-consumer plastics for feedstock recycling, Journal of Material Cycles and Waste Management, https://doi.org/10.1007/s10163-018-0748-z
[17] R. Jujun, Q. Yiming, X.u. Zhenming, Environment-friendly technology for recovering nonferrous metals from e-waste: Eddy current separation, Resour. Conserv. Recycl. 87 (2014) 109–116.

Journal of Environmental Chemical Engineering 9 (2021) 105496

Contents lists available at ScienceDirect

Journal of Environmental Chemical Engineering

journal homepage: www.elsevier.com/locate/jece

Characterisation of Hazardous Waste Landfill Leachate and its Reliance on Landfill Age and Seasonal Variation: A Statistical Approach

Pratibha Gautam [a,b], Sunil Kumar [a,b,*]

[a] Academy of Scientific and Innovative Research (AcSIR), Ghaziabad 201002, India
[b] CSIR-National Environmental Engineering Research Institute (CSIR-NEERI), Nehru Marg, Nagpur 440020, India

ARTICLE INFO

Editor: Dr. GL Dotto

Keywords:
Leachate
Hazardous waste landfills
Characterisation
ANOVA
Post hoc analysis

ABSTRACT

Leachate generated due to disposal industrial solid waste into common hazardous waste landfills (HWLs), has high potential to contaminate nearby soil and groundwater and hence its catchment and treatment are crucial for sustainable solid waste management. This research is emphasised on creating an extensive data set generated from analysing three hazardous waste landfills of age 2-year, 11-year and 20-year for a duration of one year to characterise the leachate and to create an in-depth understanding about the effect of landfill age and seasonal variation on leachate characteristics. Results in the form of descriptive statistics showed the simultaneous occurrence of high chemical oxygen demand (COD) (up to 35,000 mg/l) and high concentration of total dissolved solids (TDS) (up to 3,00,000 mg/l), ammoniacal nitrogen (up to 2300 mg/l) and heavy metals. Statistical analysis through ANOVA and Post Hoc analysis indicated that the age of landfill significantly affects the leachate characteristics and for most of the parameters, the concentrations were found to increase till middle age and then subside towards maturity of landfill. In contrast to this, for seasonal variation, less significant influence was observed on the leachate characteristics. Although the concentration of different parameters was found to vary every month, no specific pattern or effect on seasonal variation could be traced from the data.

1. Introduction

Rapid increase in population and consequent urbanisation and industrialisation in the last few decades have resulted in generation of huge quantities of solid waste (municipal and industrial) [1,2], and major part of which unfortunately ends up in landfills [3,4]. The industrial waste, which is immensely hazardous in nature when dumped into the landfills, undergoes various physical and chemical changes and leads to the generation of leachate [5]. This leachate is characterised by dark brown or black colour with very high concentration of chemical oxygen demand (COD), ammoniacal nitrogen, heavy metals and other organic and inorganic pollutants. It has high potential to contaminate nearby soil and groundwater, if not collected and treated [6–9]. Therefore, leachate management is an important aspect of solid waste management and all the hazardous waste landfills (HWLs) and most of municipal landfills (MWLs) are equipped with leachate collection system for its safe collection, which is then sent for on-site or off-site treatment [10]. Major advance treatment technologies used for leachate (more specifically HWL leachate) include ozone based processes (like ozone in alkaline medium, ozone with hydrogen peroxide, ozone with UV & hydrogen peroxide and catalytic ozonation), Chemical based process (like Fenton oxidation process, persulfate with heat, persulfate with Fe(II) and persulfate oxidation), electrolysis based process (like electrochemical oxidation, electrocoagulation and electro Fenton), photo assisted processes (photo assisted Fenton process, persulfate with UV, ozone with UV, peroxide with UV, photocatalysis and photoelectrochemical) and other miscellaneous processes (like wet air oxidation, hydrodynamic cavitation, ultrasound assisted processes and catalyst assisted processes) [11].

As any kind of treatment depends on characteristics of the influent, it is essential to understand the major characteristics of leachate so that an appropriate system can be designed for its treatment [12]. Leachate characteristics depend on many parameters, such as properties of the parent waste dumped in landfill, operational condition of landfill and its interaction with the external environment [13,14]. As municipal waste landfills (MWLs) contain a considerable fraction of biodegradables, the age of landfill defines degree of waste decomposition and hence characteristics of leachate get considerably dependent on landfill age but in case of hazardous waste landfill, the scenario is completely different. Industrial solid waste is pre-treated before dumping and also it doesn't

* Corresponding author at: Academy of Scientific and Innovative Research (AcSIR), Ghaziabad 201002, India.
E-mail address: s_kumar@neeri.res.in (S. Kumar).

https://doi.org/10.1016/j.jece.2021.105496
Received 7 January 2021; Received in revised form 4 April 2021; Accepted 10 April 2021
Available online 20 April 2021

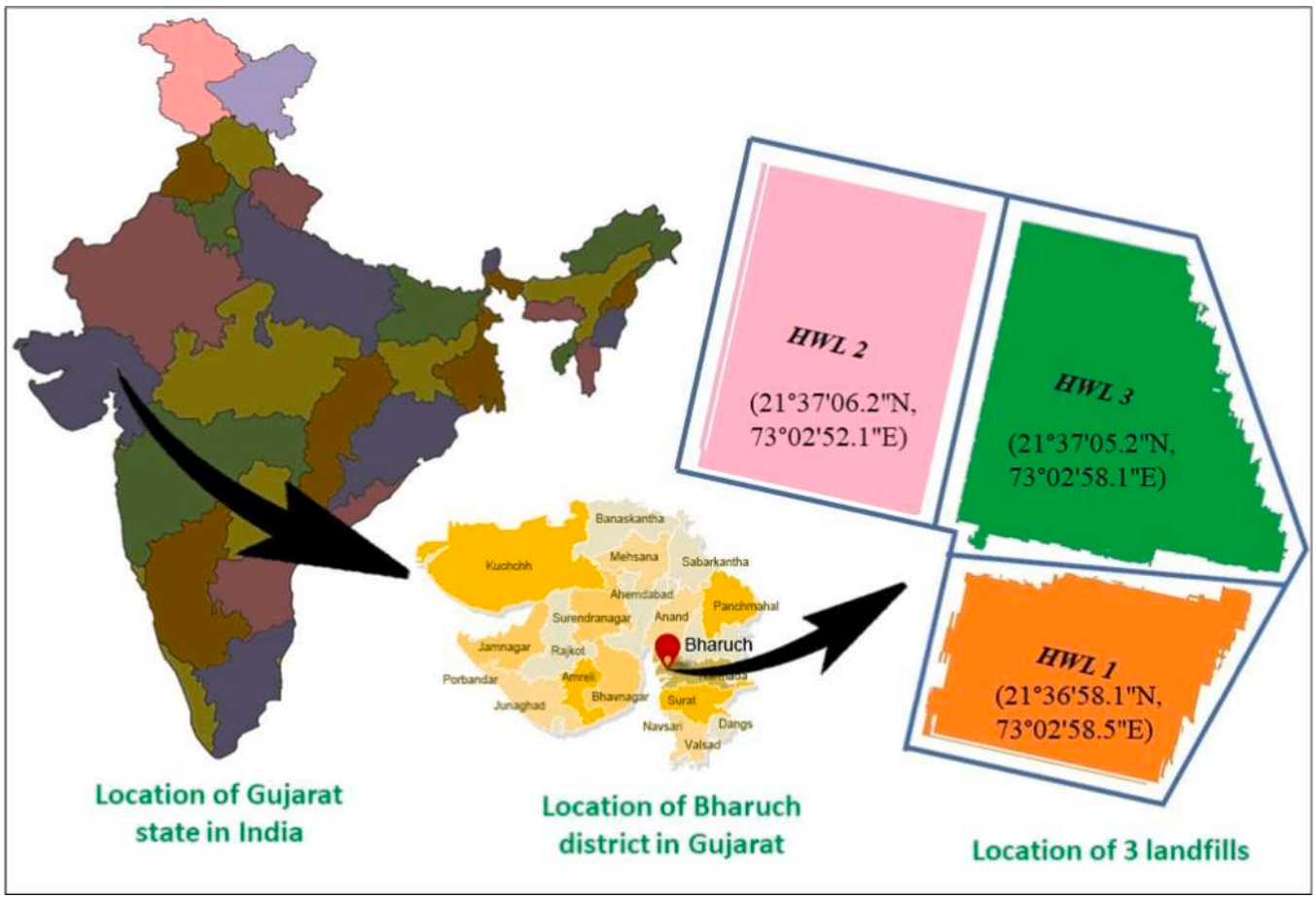

Fig. 1. Location of landfills.

contain (or negligible) any biodegradable fraction. Therefore, the process inside the landfills and characteristics of leachate are entirely different in both kinds of landfills. Leachate produced from HW landfills is multiple fold more toxic than the leachate produced from MW landfills [15] and therefore the biodegradability of the former category is comparatively very low than the later one. Hence, the results and conclusions of previous research on treatment of MW landfill leachate cannot be directly applied on treatment of HW landfill leachate. Many researchers have carried out the characterisation studies for MWL leachate [16–18] but almost negligible efforts have been made for the characterisation of leachate produced from HWLs (almost none in last two decades). It is reported that the characteristics of leachate (produced from MWLs) varies with the age of landfill [19] and it is also dependent on the seasonal variation [20,21], but no such studies are available for HWL leachate to give comprehension about its association with other factors that are very well established or studied for MWLs.

In order to bridge this gap, one of the objectives of this study was to prepare a database for characterisation of the leachate produced from different HWLs. As the leachate characteristics are directly influenced by the type of waste disposed in the landfills, three landfills from the same project site were selected so that the comparable results can be obtained. The exhaustive dataset compiled in this study can be used as a supporting document or database to understand the characteristics of HWL leachate in a broader aspect and accordingly design the treatment system. The results obtained from this part of the research can also be used for comparative assessment study between MWL and HWL leachate. Additionally, the research output will also be useful in observing the trends in HWL leachate and would provide an opportunity to explore the mechanism behind it. Another objective of the study was to assess the effect of landfill age and seasonal variation on the characteristics of leachate produced from hazardous waste landfills. The conclusions were arrived based on the statistical tools like ANOVA and post hoc analysis which made the conclusion more convincing and easily acceptable. No such detailed and dedicated study for HWL leachate is available in last two decades, thus the results of this study will give researchers an insight the recent times to HWL and the characteristic behaviour of the leachate produced.

2. Material and methodology

2.1. Study area and sampling plan

Gujarat is a state in India which is pioneering in industrial sector and thus has maximum number of HWLs to accommodate huge quantities of industrial waste being produced in the state. The study area (district) was Bharuch, where the landfills under study are located. To study the effect of 'landfill age' on leachate characteristics, three landfills of different age were identified and named as HWL1 (age 20 year), HWL 2, (age 11 year) and HWL3 (age 2 year), and the leachate samples were collected from all the three landfills. HWL1 (21°36′58.1″N, 73°02′58.5″E), a closed landfill, has an area of 36,000 m^2 with a capacity to dump 0.6 million tons of waste. HWL2 (21°37′06.2″N, 73°02′52.1″E), which is still operating, has an area of 93,000 m^2 with 1.7 million tons waste dumping capacity and HWL 3 (21°37′05.2″N, 73°02′58.1″E), is also still operating and has 12,000 m^2 area with a capacity to accommodate 1.45 million tons of industrial waste. In general, wastes identified as "Hazardous Waste" under "Hazardous and Other Wastes (Management and Transboundary Movement) Rules, 2016" are dumped into these landfills which mainly contain the process sludge from industries, effluent treatment plant (ETP) sludge,

Table 1
List of parameters under the study.

Parameters	Methods	Instrument/ Apparatus	Make and Model No
pH	IS:3025(P-11) 83Re.02	pH Metre	Make: EUTECH Model: PC 2700
Colour	IS:3025 (Part 4)	UV-spectrophotometer	Make: SHIMADZU Model: UV-1800
Oil and grease	APHA (22nd Ed) 5220- / IS 3025 (Part 39)	Separating funnel	NA (Glassware)
Chemical oxygen demand (COD)	APHA (22nd Ed) 5200-B	Open Reflux method	Make: SPECTRALAB Model: 2015-M
Biological oxygen demand (BOD)	APHA (22nd Ed) 5210-B / IS 3025 (Part 44) 1993	Incubator	Make: Cintex
Total Nitrogen (TN)	APHA (22nd Ed) 4500-N-B	UV Spectrophotometer	Make: SHIMADZU Model: UV-1800
Total Kjeldahl Nitrogen (TKN)	APHA (22nd Ed) 4500-C / IS 3025 (Part 34)	Kjeldahl's apparatus	NA (Glass Assembly)
Ammoniacal Nitrogen (AMM NIT)	APHA (22nd Ed) 4500-C / IS 3025 (Part 34)	Titrimetric Method	NA (Glass Assembly)
Total Phosphorus (TP)	APHA-4500-P. C	UV spectrophotometer	Make: SHIMADZU Model: UV-1800
Total Hardness (TH)	EDTA Titration Method	Titrimetric	NA (Glass Assembly)
Total Alkalinity (TA)	TITRATION METHOD	Electrometric Titrator	NA (Glass Assembly)
Total Dissolved Solid (TDS)	IS:3025 (Part 17)/ APHA (22nd Ed) 2540 C	Hot Air Oven	Make: BIOTECH Model: BTI-20
Total Suspended Solid (TSS)	IS:3025 (Part 17)/ APHA (22nd Ed) 2540 D	Hot Air Oven	Make: BIOTECH Model: BTI-20
Chloride (Cl)	IS:3025 (Part 24)	Erlenmeyer flask	NA (Glass Assembly)
Sulphide	APHA (22nd Ed) 4500-S2 F	Glass assembly	NA (Glass Assembly)
Sulphate (SO_4^{2-})	APHA 4500-SO4 E	UV Spectrophotometer	Make: SHIMADZU Model: UV-1800
Total Phenol (TPh)	IS:3025(P-43)92. Re. 03	UV Spectrophotometer	Make: SHIMADZU Model: UV-1800
Metals			
Arsenic (As)	APHA 3111-AS-B	HG-AAS	Make: Shimadzu Model: AA-7000
Boron (B)	APHA (22nd Ed) 4500-B C.	AAS	Make: Shimadzu Model: AA-7000
Barium (Ba)	AAS- APHA (22nd Ed) 3113-B	AAS	Make: Shimadzu Model: AA-7000
Calcium (Ca)	EDTA Titration Method	Titrimetric	NA (Glass Assembly)
Cadmium (Cd)	APHA-3111- B	AAS	Make: Shimadzu Model: AA-7000
Chromium (Cr)	AAS- APHA (22nd Ed) 3111-B	AAS	Make: Shimadzu Model: AA-7000
Copper (Cu)	APHA 3111-CU-B	AAS	Make: Shimadzu Model: AA-7000
Iron (Fe)	IS:3025(Part-53)–2003	AAS	Make: Shimadzu Model: AA-7000
Mercury (Hg)	APHA-3111-HG-B	HG-AAS	Make: Shimadzu Model: AA-7000
Potassium (K)	IS:3025 (Part 45)	AAS	Make: Shimadzu Model: AA-7000
Magnesium (Mg)	EDTA Titration Method	Titrimetric	NA (Glass Assembly)
Sodium (Na)	IS:3025 (Part 45)	Flame Photometer	Make: ESICO Model: 1385
Zinc (Zn)	AAS- APHA (22nd Ed) 3113-B	AAS	Make: Shimadzu Model: AA-7000
Lead (Pb)	AAS- APHA (22nd Ed) 3113-B	AAS	Make: Shimadzu Model: AA-7000
Nickel (Ni)	AAS- APHA (22nd Ed) 3113-B	AAS	Make: Shimadzu Model: AA-7000

contaminated barrels, contaminated bags and other type of hazardous waste being produced from more than two thousand industries. The type of industries from where the waste is generated is similar to all the three landfills as HWL 3 is the extension of HWL2 and HWL 2 is the extension of HWL 1, and the industry type includes pesticides and insecticides sector, fertiliser sector, pharmaceutical industries, common effluent treatment plants, specialty chemicals sector, dyes and pigment sector and many more. Locations of these landfills are shown in Fig. 1.

With an aspiration to study the effect of seasonal variation, leachate samples were withdrawn at monthly frequency for a duration of one year. Individual landfill usually has multiple leachate wells and samples were drawn from all the wells. During the sampling, necessary care was taken to avoid any dilution of samples through rainwater and samples were stored in refrigerator at 4 ℃ to avoid any change in the characteristic during analysis.

2.2. Parameter under study and analytical methods

As the constituents of leachate primarily depend on the composition of parent material [22], generally, the characteristics of HWL leachate are not uniform. The type and number of industries which send waste to landfills varies according to location and therefore a uniform criterion cannot be defined for all HWLs. Based on the previous studies and consent to operate given to these landfills, 32 parameters were identified which are summarised with their standard method of analysis in Table 1, where term IS, APHA, UV and AAS stands for Indian Standards, American Public Health Association, Ultraviolet and Atomic Absorption Spectrometer, respectively.

Table 2
Descriptive statistics of leachate characteristics.

Parameter	HWL	N	Mean	SD	Min	Max
AMM NIT (mg/l)	HWL1	12	1.6 E3	60.9	1.5 E3	1.7 E3
	HWL2	12	2.3 E3	84.5	2.2 E3	2.5 E3
	HWL3	12	2.2 E3	247.3	1.8 E3	2.6 E3
BOD (mg/l)	HWL1	12	4.8E3	254.9	4.3E3	5.3E3
	HWL2	12	1.3E4	409.6	1.2E4	13837.4
	HWL3	12	1.1E4	929.5	9.7E3	1.3E4
COD (mg/l)	HWL1	12	1.5E4	816.8	1.3 E4	1.6 E4
	HWL2	12	3.9E4	1663.6	3.4 E4	4.0 E4
	HWL3	12	3.5E4	2300.4	3.2 E4	3.8 E4
CHLORIDE (mg/l)	HWL1	12	6.3 E4	7517.6	5.0 E4	7.6 E4
	HWL2	12	1.3 E5	14164.1	1.0 E4	1.6 E5
	HWL3	12	1.3 E5	26828.4	6.5 E4	1.7E5
COLOUR (Pt-Co)	HWL1	12	3.1E3	616.0	2.2 E3	3.9 E3
	HWL2	12	9.5 E3	1242.3	7.8 E3	1.1 E4
	HWL3	12	9.2 E3	1596.0	6.7 E3	1.2 E4
OILGREASE (mg/l)	HWL1	12	4.9	1.0	2.3	6.1
	HWL2	12	6.2	0.5	5.3	7.0
	HWL3	12	6.1	0.9	4.2	7.6
pH	HWL1	12	7.4	0.1	7.2	7.5
	HWL2	12	7.7	0.1	7.5	7.8
	HWL3	12	7.4	0.2	7.2	7.7
SULPHATE (mg/l)	HWL1	12	1.6E4	2266.6	1.3 E4	2.0 E4
	HWL2	12	3.3 E4	5795.2	2.0 E4	4.1 E4
	HWL3	12	2.6 E4	5622.4	1.9 E4	3.7 E4
SULPHIDE (mg/l)	HWL1	12	317.9	43.7	231.5	365.7
	HWL2	12	598.9	113.3	411.5	709.7
	HWL3	12	458.9	112.0	293.0	576.0
TA (mg/l)	HWL1	12	6.5 E3	949.9	5.2 E3	7.6 E3
	HWL2	12	1.0 E4	2029.1	7.8 E3	1.4 E4
	HWL3	12	8.6 E3	2794.1	3.7 E3	1.2 E4
TDS (mg/l)	HWL1	12	1.5E5	9058.6	1.2 E5	1.5 E5
	HWL2	12	3.0E5	16464.0	2.6 E5	3.2 E5
	HWL3	12	2.8E5	19040.4	2.6 E5	3.1 E5
TH (mg/l)	HWL1	12	6.7E3	1115.1	5.2 E3	8.5 E3
	HWL2	12	8.2 E3	2550.4	3.2 E3	1.2 E4
	HWL3	12	9.8 E3	2063.2	6.9 E3	1.3 E4
TKN (mg/l)	HWL1	12	2.3E3	83.6	2.2E3	2.5E3
	HWL2	12	3.1E3	141.6	2.9E3	3.3 E3
	HWL3	12	2.7E3	429.9	2.2E3	3.5 E3
TN (mg/l)	HWL1	12	3.9 E3	215.9	3.6 E3	4.1 E3
	HWL2	12	4.0 E3	254.2	3.5 E3	4.3 E3
	HWL3	12	3.4 E3	382.6	3.0 E3	4.1 E3
TOTAL PHENOL (mg/l)	HWL1	12	16.7	6.3	12.1	35.5
	HWL2	12	26.5	2.4	21.9	31.5
	HWL3	12	22.4	5.3	10.8	30.1
TOTAL PHOSPHORUS (mg/l)	HWL1	12	35.1	12.7	22.0	68.3
	HWL2	12	35.8	10.5	25.4	57.7
	HWL3	12	30.1	7.4	14.0	41.3
TSS (mg/l)	HWL1	12	1.4 E3	115.8	1.2 E3	1.6 E3
	HWL2	12	1.6 E3	57.7	1.5 E3	1.7 E3
	HWL3	12	1.6 E3	165.1	1.3 E3	1.9 E3
Metals						
Calcium (mg/l)	HWL 1	12	7.9 E2	120.134	6.0 E2	9.4 E2
	HWL 2	12	1.1 E3	352.933	7.1 E2	1.8 E3
	HWL 3	12	1.2 E3	208.773	9.7 E2	1.5 E3
Cadmium (mg/l)	HWL 1	12	0.318	0.159	0.059	0.511
	HWL 2	12	0.573	0.394	0.006	0.924
	HWL 3	12	0.411	0.297	0.003	0.706
Chromium (mg/l)	HWL 1	12	0.637	0.321	0.214	1.220
	HWL 2	12	0.902	0.541	0.529	2.146
	HWL 3	12	0.628	0.426	0.241	1.811
Copper (mg/l)	HWL 1	12	0.771	0.312	0.146	1.130
	HWL 2	12	2.685	0.831	1.656	4.858
	HWL 3	12	1.172	0.833	0.176	3.232
Iron (mg/l)	HWL 1	12	5.656	1.498	1.885	7.539
	HWL 2	12	6.547	1.888	2.042	9.526
	HWL 3	12	4.134	1.600	1.201	8.218
Potassium (mg/l)	HWL 1	12	3.2 E3	1142.500	2.1 E3	6.4 E3
	HWL 2	12	3.7 E3	370.249	3.0 E3	4.6 E3
	HWL 3	12	4.7 E3	829.520	2.6 E3	5.9 E3
Magnesium (mg/l)	HWL 1	12	1.1 E3	229.131	7.2 E2	1.4 E3
	HWL 2	12	1.1 E3	529.107	3.6 E2	1.9 E3
	HWL 3	12	1.8 E3	473.251	1.0 E3	2.6 E3
Sodium (mg/l)	HWL 1	12	4.1 E4	2448.329	3.7 E4	4.5 E4

(*continued on next page*)

Table 2 (*continued*)

Parameter	HWL	N	Mean	SD	Min	Max
	HWL 2	12	4.7 E4	4027.842	4.2 E4	5.5 E4
	HWL 3	12	4.5 E4	2977.727	4.0 E4	5.0 E4
Zinc (mg/l)	HWL 1	12	1.586	2.257	0.362	8.315
	HWL 2	12	2.335	2.061	0.768	6.151
	HWL 3	12	0.475	0.482	0.155	1.682
Nickel (mg/l)	HWL 1	12	2.737	1.774	0.163	6.625
	HWL 2	12	4.807	2.828	0.132	9.087
	HWL 3	12	4.254	2.398	0.053	6.857
Lead (mg/l)	HWL 1	12	2.380	1.209	0.707	5.622
	HWL 2	12	3.670	2.207	0.295	8.599
	HWL 3	12	3.363	1.934	0.941	7.601

2.3. Statistical methods

As the datasheets gathered for all three landfills were very exhaustive, different statistical tools were used for data analysis, deriving useful information and concluding the extract. One single landfill has multiple wells and therefore for a single month also, multiple readings were obtained from a single landfill for single parameter. Hence, for describing general characteristics, data were compiled in one single sheet for all the three landfills with a tool "descriptive Statistics" [23] provided in Minitab which contains mean, standard deviation, minimum and maximum value obtained. To analyse the effect of age and seasonal variation, first ANOVA was performed to statistically analyse if these parameters have significant impact on any leachate characteristic. The parameters for which the significant impact was observed through ANOVA, Post hoc analysis was carried out for them to study the cause of impact or nature of variation [24].

3. Results and discussion

3.1. Leachate characterisation

All the three identified landfills (HWL1, HWL2 and HWL3) were monitored for a duration of 12 months starting from August 2018 to July 2019 and leachate samples were withdrawn at monthly frequency. Parameters as mentioned in Table 1 were analysed for all the samples and their results are summarised in Table 2. Descriptive statistics of this data include standard deviation (SD), mean, standard error, minimum value (min) and maximum value (max). This data was further analysed to study the impact of landfill age and seasonal variation. Few characteristic parameters are also analysed in the form of boxplot (Fig. 2).

As presented in Table 2, the average value of pH for all the landfills was in neutral range which repudiates the requirement of leachate neutralisation before its treatment which is usually the first step at any effluent treatment plant having other subsequent processes including different secondary (biological) treatment processes. Various other technologies for leachate treatment include coagulation-flocculation, Fenton process, electrocoagulation process and hybrid processes like photo-electro-Fenton with biological oxidation and other hybrid processes like electrocoagulation with biofiltration etc. [25–28]. The reason behind neutral pH is that all the waste before dumping in landfill is neutralised if it is acidic or basic in nature. Mean COD value for leachate of young landfill (HWL3, age = 2 year) varied from 32.1 g/l to 38.8 g/l (against the discharge standard of 0.25 g/l) whereas for same landfill, mean BOD values fell in the range 9.75–13.4 g/l (against the discharge standard of 0.03 g/l), which point towards a BOD/COD ratio of 0.30–0.34, implying low biodegradability of the leachate. For the same landfill leachate, chloride values were varying from 65 to 173 g/l (against the discharge standard of 1 g/l) along with very high TDS values ranging from 260 to 317 g/l (against the discharge standard of 2.1 g/l). Such high TDS values in association with high COD make this leachate slightly unfit for direct biological treatment whereas high chloride and high TDS implies good conductivity in the medium indicating the suitability of electrolytic processes for its treatment. For the same landfill leachate, the presence of considerable phenol concentration (10.8 mg/l to 30.1 mg/l) (against the discharge standard of 1 mg/l), high ammoniacal nitrogen (1.85–2.62 g/l) (against the discharge standard of 0.05 g/l), elevated sulphide concentrations (ranging from 293 mg/l to 576 mg/l) and significant number of other pollutants exhibited a complex pollutant matrix where the presence of one pollutant might affect the measurement, treatment and removal of the other pollutants. The reference for discharge standards of treated leachate has been taken from "Solid Waste Management Rules, 2016" [29], as no separate standards exist for HWL leachate.

In the leachate from same well, metals with high occurrence were calcium, potassium, magnesium and sodium with mean concentration equating to 1282 mg/l, 4768 mg/l, 1804 mg/l and 45,276 mg/l, respectively. Other metals with significant concentration in the same HWL leachate were nickel, lead, iron and copper with corresponding mean concentrations as 4254 μg/l, 3363 μg/l, 4134 μg/l and 1172 μg/l, respectively.

Many other heavy metals including zinc, chromium and cadmium were having mean concentration as 475 μg/l, 628 μg/l and 411 μg/l respectively, whereas few metals like arsenic, barium and mercury were found in less concentration (less than 2 μg/l, 0.1 mg/l, and 1 μg/l respectively) in all the samples and boron was less than 0.1 mg/l in most of the samples so their readings were discarded from the result sheet, although their sampling and analysis was done throughout the year for all the landfills.

Due to simultaneous occurrence of so many pollutants (Table 2) in high concentration, the output effluent demonstrated recalcitrant behaviour during the treatment. To analyse variation in characteristics, month wise distribution of few parameters (randomised selection) is shown in Fig. 3, which reveals that for certain parameters, like chromium, lead and zinc, some random variations are appearing in the graphs but there is no specific pattern for the same. In fact, no trend is evident from the fluctuation in concentration when the parameters are studied across the year, which indicated that the variations are not due to any external parameters like rain or temperature. Other principal components like COD, BOD and ammoniacal nitrogen do not exhibit any significant variation in concentration due to change in season for any of the landfills.

3.2. Analysing the effect of age on leachate characteristics

Relationship between leachate characteristics and age of the MWL has been studied by several researchers [19] and it is reported that several physico-chemical and biological transformations occur in landfill with the passage of time and lead to change in properties of leachate [30]. Whereas, in hazardous waste landfills, biodegradable fraction is very limited, and hence it is assumed that with the ageing of landfill, only physico-chemical transformations take place and influence the characteristics of leachate. To study this effect in HWLs, leachate samples from three different landfills (HWL1 of age 20 years, HWL2 of age 11years and HWL3 age 2 years) were investigated through analysis of

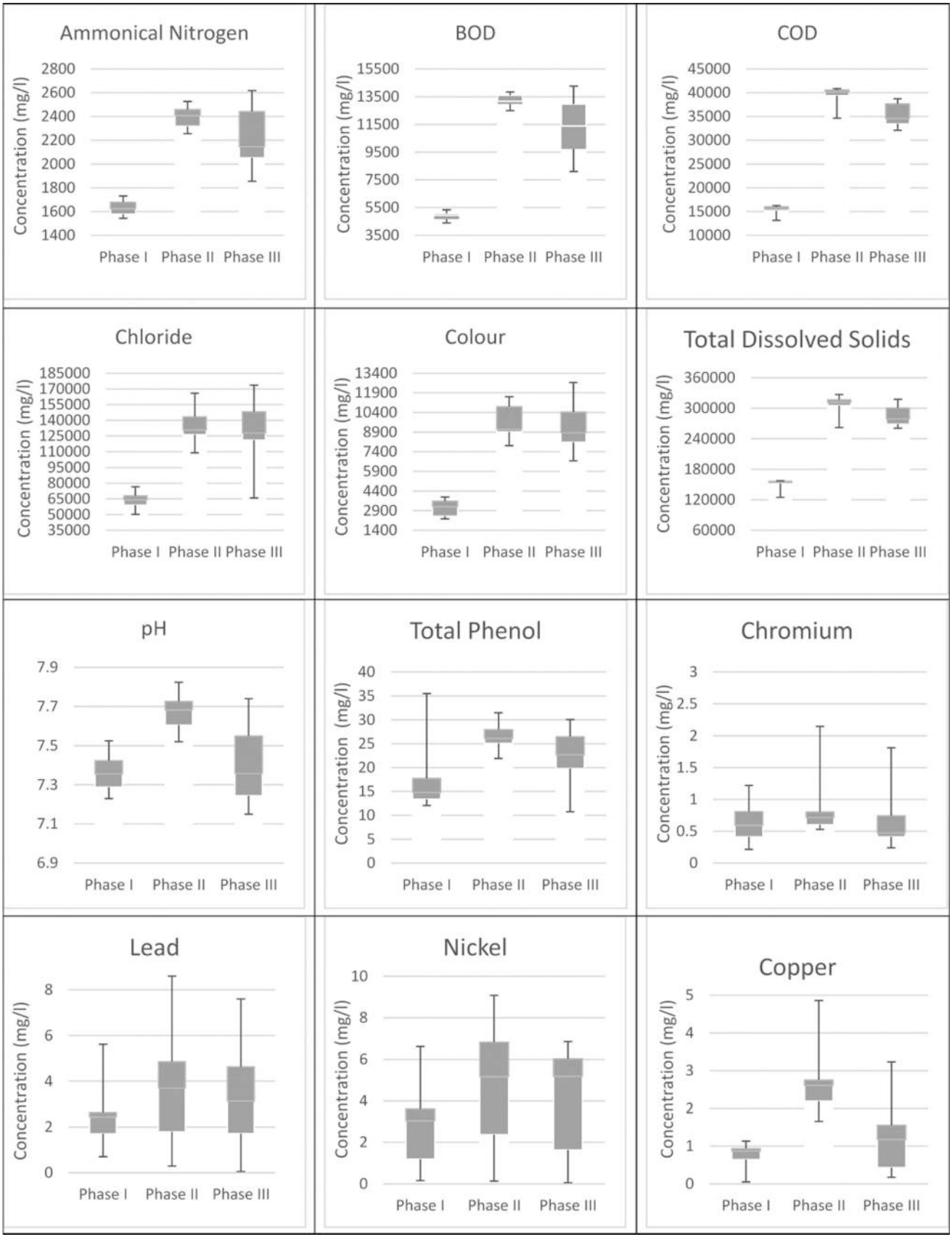

Fig. 2. Box Plot diagram for selected parameters.

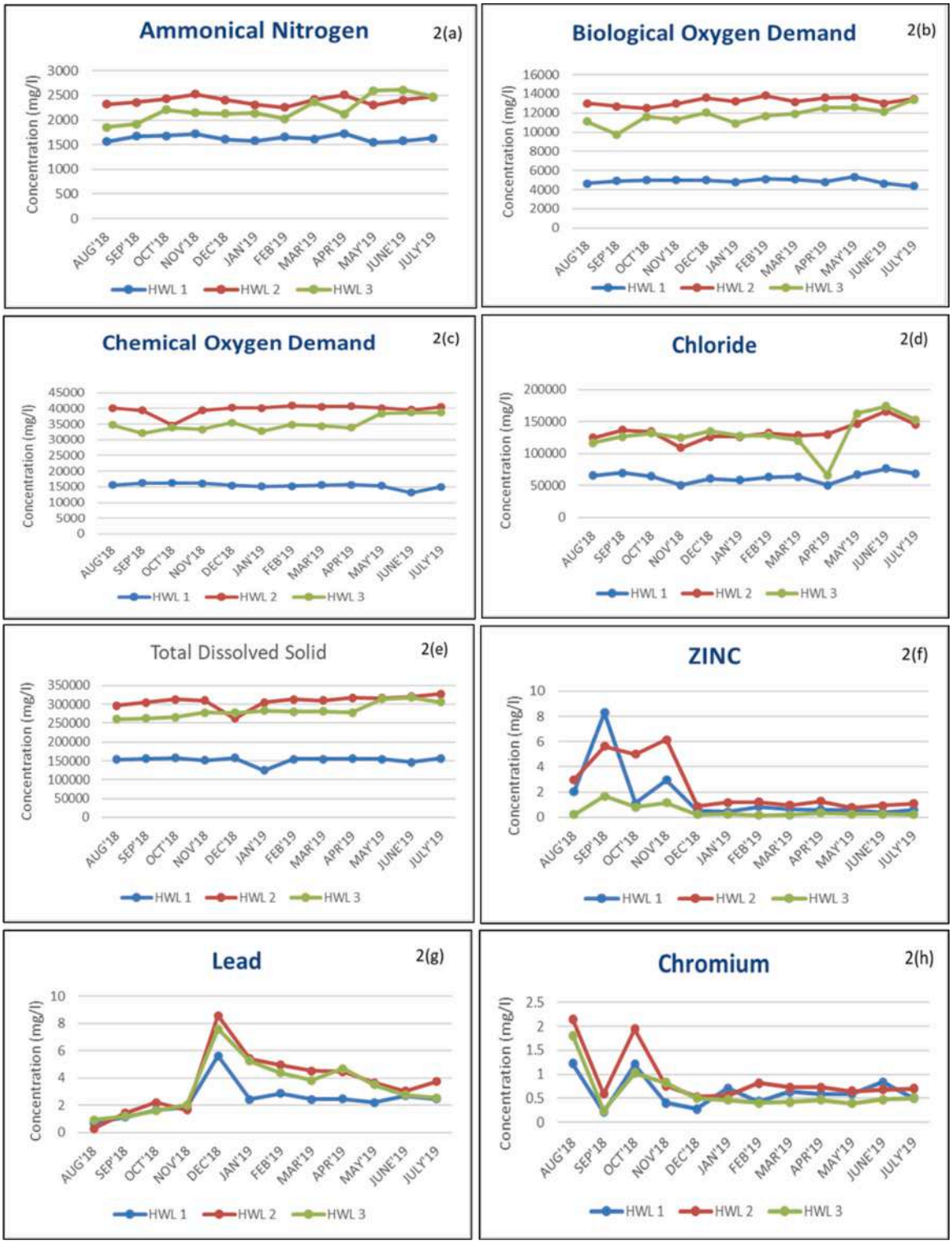

Fig. 3. Monthly variation in leachate characteristics.

variance (ANOVA) and the results are presented in Table 3. The analysis was carried out with a hypothesis that landfill age does not affect the leachate characteristics.

Results for general parameters (Table 3) showed that for total phosphorus (TP), the level of significance is 0.356 (>0.05) which means acceptance of hypothesis, implying that landfill age does not affect TP concentration in leachate.

Other general parameters except TP have *p value* lower than 0.05 which lead to rejection of hypothesis for remaining other parameters and indicated that landfill age has significant impact on these characteristic parameters. Similarly, the results for metals showed that for cadmium, chromium and lead, the level of significance is higher than 0.05 which supports the acceptance of null hypothesis and suggests that landfill age does not has significant impact on concentration of these metals. Whereas for calcium, copper, iron, potassium, magnesium, sodium and zinc, *p value* is less than 0.05, indicating rejection of null hypothesis and implying that landfill age significantly affects the occurrence of these metals in leachate.

Table 3
Effect of age on leachate characteristics (ANOVA).

Analysis of Variance (general)						
Parameters		**Sum of Square ogSquares**	**Df**	**Mean Square**	**F**	**Sig.**
AMM NIT	Between Groups	3813916	2	1906958	79	0.000
	Within Groups	792249	33	24008		
	Total	4606165	35			
BOD	Between Groups	474500000	2	237300000	649	0.000
	Within Groups	12060000	33	365564		
	Total	486600000	35			
COD	Between Groups	3993000000	2	1997000000	686	0.000
	Within Groups	95990000	33	2908856		
	Total	4089000000	35			
Chloride	Between Groups	38080000000	2	19040000000	58	0.000
	Within Groups	10750000000	33	325600000		
	Total	48830000000	35			
Colour	Between Groups	315700000	2	157900000	106	0.000
	Within Groups	49170000	33	1490051		
	Total	364900000	35			
Oil & Grease	Between Groups	12	2	6	9	0.001
	Within Groups	22	33	1		
	Total	35	35			
pH	Between Groups	1	2	0	21	0.000
	Within Groups	1	33	0		
	Total	1	35			
Sulphate	Between Groups	1823000000	2	911700000	39	0.000
	Within Groups	773700000	33	23440000		
	Total	2597000000	35			
Sulphide	Between Groups	473562	2	236781	26	0.000
	Within Groups	300157	33	9096		
	Total	773719	35			
TA	Between Groups	87610000	2	43800000	10	0.000
	Within Groups	141100000	33	4275565		
	Total	228700000	35			
TDS	Between Groups	169600000000	2	84820000000	356	0.000
	Within Groups	7872000000	33	238600000		
	Total	177500000000	35			
TH	Between Groups	57470000	2	28740000	7	0.003
	Within Groups	132100000	33	4001639		
	Total	189500000	35			
TKN	Between Groups	3384011	2	1692006	24	0.000
	Within Groups	2330646	33	70626		
	Total	5714658	35			
TN	Between Groups	2999611	2	1499805	17	0.000
	Within Groups	2834227	33	85886		
	Total	5833838	35			
Total Phenol	Between Groups	581	2	291	12	0.000
	Within Groups	799	33	24		
	Total	1380	35			
Total Phosphorus	Between Groups	232	2	116	1	0.356
	Within Groups	3582	33	109		
	Total	3814	35			
TSS	Between Groups	319849	2	159924	11	0.000
	Within Groups	483859	33	14662		
	Total	803708	35			
Analysis of Variance (metals)						
Parameter		**Sum of Squares**	**Df**	**Mean Square**	**F**	**Sig.**
Calcium	Between Groups	1634760.662	2	817380.331	13.431	0.000
	Within Groups	2008378.825	33	60859.964		
	Total	3643139.487	35			

(*continued on next page*)

Table 3 (*continued*)

Analysis of Variance (general)						
Parameters		**Sum of Square ogSquares**	**Df**	**Mean Square**	**F**	**Sig.**
Cadmium	Between Groups	0.401	2	0.201	2.240	0.122
	Within Groups	2.954	33	0.090		
	Total	3.355	35			
Chromium	Between Groups	0.580	2	0.290	1.506	0.237
	Within Groups	6.356	33	0.193		
	Total	6.937	35			
Copper	Between Groups	24.452	2	12.226	24.743	0.000
	Within Groups	16.306	33	0.494		
	Total	40.758	35			
Iron	Between Groups	35.718	2	17.859	6.404	0.004
	Within Groups	92.024	33	2.789		
	Total	127.742	35			
Potassium	Between Groups	14361803.637	2	7180901.818	10.112	0.000
	Within Groups	23435439.683	33	710164.839		
	Total	37797243.319	35			
Magnesium	Between Groups	3524181.071	2	1762090.536	9.500	0.001
	Within Groups	6120641.826	33	185473.995		
	Total	9644822.897	35			
Sodium	Between Groups	208828259.916	2	104414129.958	10.077	0.000
	Within Groups	341931484.132	33	10361560.125		
	Total	550759744.048	35			
Zinc	Between Groups	21.003	2	10.501	3.292	0.050
	Within Groups	105.280	33	3.190		
	Total	126.283	35			
Nickel	Between Groups	27.554	2	13.777	2.446	0.102
	Within Groups	185.867	33	5.632		
	Total	213.421	35			
Lead	Between Groups	10.891	2	5.446	1.622	0.213
	Within Groups	110.799	33	3.358		
	Total	121.690	35			

To further analyse the nature of variation and to understand that which landfill has significant variation in means, Post Hoc analysis was performed with subset of alpha as 0.05 and harmonic mean sample size of 12. Results of Post Hoc analysis (displaying means for groups in homogeneous subsets) for all the identified parameters are collectively represented in Table 4. Post Hoc analysis for ammoniacal nitrogen indicated that there is a significant difference among the mean values of ammoniacal nitrogen for HWL3, HWL2 and HWL1. A detailed analysis of variation in means disclosed that the concentration of ammoniacal nitrogen increases up to a certain age of landfill (from HWL3 of 2 years to HWL2 of 11 years) and then decreases significantly with further aging of landfill (HWL1, age 20 years) which is in contrast with the trends reported in MWL (no decrease in concentration with time) [13]. The reason behind such trend in MWLs is that in young age, amino acids undergo deamination whereas in later age, the nitrogenous fraction of biodegradable waste undergoes hydrolysis and fermentation, which results in consistent occurrence of ammoniacal nitrogen in leachate [31]. Post Hoc analysis for BOD, COD, sulphate, sulphide, TDS and TKN exhibited the similar trend where corresponding means are significantly different in HWL1, HWL2 and HWL3. Akin to Ammoniacal nitrogen, the mean values of BOD, COD, sulphate, sulphide, TDS and TKN first showed an increasing trend (from age of HWL3 to HWL2) and then decreased significantly with an increase in age (HWL1).

It is also witnessed that in most of the cases after reaching the peak, the concentration of these parameters in later stage (age>20 years) falls down even below than its value in the initial years (2 years). BOD, COD, sulphate, sulphide, TDS and TKN are also considered as principal components in effluent and the analysis of their reliance on landfill age indicated that at middle age (10–15 years), the concentration of these parameters was at the peak.

Post Hoc analysis for chloride showed that there was no significant difference between mean values of chloride for HWL3 (2 years) and HWL2 (11 years), whereas, the mean chloride value in HWL1 was significantly different from HWL2 and HWL3. Further analysis of means indicated that up to an age of 11 years (HWL2), mean chloride values were in similar range (with a sluggish decline), but as the age of landfill increased (HWL1), chloride values experienced a sharp decline. A similar trend was observed for colour, oil and grease, total phenol and TSS, where the values corresponding to HWL3 and HWL2 were not significantly different but as the landfill age increased (HWL1), there was a sharp decline.

Post Hoc analysis of total nitrogen depicted that the mean values of TN for young landfill (HWL3) were significantly different from HWL2 and HWL1, whereas no significant difference was observed for TN mean values between HWL2 and HWL 1.

A careful study of the means showed that up to an age corresponding to HWL2, the mean value considerably increased but after that it remained in the same range with a slight decline. From the results, it can be summarised that TN values in a HWL increases with the landfill age up to middle age (10–15 years) and afterwards it becomes stabilised with a minor decline.

Post Hoc analysis for pH showed that there was no significant difference in the mean pH values between youngest (HWL3) and oldest (HWL1) landfill whereas the mean values for HWL 2 were significantly different from HWL1 and HWL3. Study of the means showed that it remained in neutral range (between 7 and 8) for all the ages but in middle age (11 years), the pH increased slightly and with the passage of years it again came down to the initial values.

Post Hoc analysis for total alkalinity showed that there was a significant difference between TA mean values for HWL1 and HWL2, however, no significant difference was observed between HWL1 and HWL3. Similarly, no significant difference was observed between HWL2 and HWL3. A detailed comparison of means showed that the values of TA increased till middle age and then showed a sharp decreasing trend even beyond the initial TA concentration. Post Hoc analysis for total hardness (TH) showed a completely different trend. The mean values of total hardness for HWL3 and HWL1 were significantly different whereas no significant difference was observed between HWL1 and HWL2 and similarly between HWL2 and HWL3. A comparison of means showed a decreasing trend for total alkalinity with an increase in landfill age.

Table 4
Post Hoc analysis (Effect of landfill age).

HWL	N	Ammoniacal Nitrogen			BOD			COD		
		1	2	3	1	2	3	1	2	3
HWL 1	12	1632.337			4886.383			1.540E4		
HWL 3	12		2217.000			1.174E4			3.509E4	
HWL 2	12			2394.101			1.321E4			3.969E4
Sig.		1.000	1.000	1.000	1.000	1.000	1.000	1.000	1.000	1.000
HWL	**N**	**Sulphate**			**Sulphide**			**TDS**		
		1	**2**	**3**	**1**	**2**	**3**	**1**	**2**	**3**
HWL 1	12	1.603E4			317.908			1.518E5		
HWL 3	12		2.657E4			458.875			2.837E5	
HWL 2	12			3.333E4			598.847			3.080E5
Sig.		1.000	1.000	1.000	1.000	1.000	1.000	1.000	1.000	1.000
HWL	**N**	**TKN**			**Chloride**			**Colour**		
		1	**2**	**3**	**1**	**2**		**1**	**2**	
HWL 1	12	2379.661			6.307917E4			3105.801		
HWL 3	12		2740.000			1.302942E5			9211.541	
HWL 2	12			3130.460		1.337214E5			9550.724	
Sig.		1.000	1.000	1.000	1.000	.898		1.000	.795	
HWL	**N**	**Copper**		**HWL**	**Iron**			**Zinc**		
		1	**2**		**1**	**2**		**1**	**2**	
HWL 1	12	0.770		HWL 3	4.134			0.475		
HWL 3	12	1.172		HWL 1	5.655	5.655		1.585	1.585	
HWL 2	12		2.684	HWL 2		6.546			2.334	
Sig.		.353	1.000		.080	.402		.294	.565	
HWL	**N**	**Potassium**		**Magnesium**		**HWL**		**Sodium**		
		1	**2**	**1**	**2**			**1**	**2**	
HWL 1	12	3249.834		1115.897		HWL 1		41392.072		
HWL 2	12	3753.511		1169.309		HWL 3			45276.375	
HWL 3	12		4768.542		1804.708	HWL 2			47179.698	
Sig.		.321	1.000	.950	1.000			1.000	.329	
HWL	**N**	**Oil & Grease**		**Total Phenol**		**TSS**		**HWL**	**Total Nitrogen**	
		1	**2**	**1**	**2**	**1**	**2**		**1**	**2**
HWL 1	12	4.907		16.715		1442.525		HWL 3	3409.708	
HWL 3	12		6.045		22.383		1614.625	HWL 1		3932.308
HWL 2	12		6.226		26.520		1661.869	HWL 2		4083.462
Sig.		1.000	.866	1.000	.136		.637		1.000	.459
HWL	**N**	**pH**		**Total Alkalinity**		**HWL**	**Total Hardness**		**Calcium**	
		1	**2**	**1**	**2**		**1**	**2**	**1**	**2**
HWL 1	12	7.362		6589.097		HWL 1	6778.169		790.525	
HWL 3	12	7.388		8677.125	8677.125	HWL 2	8239.081	8239.081		1188.446
HWL 2	12		7.673		10404.560	HWL 3		9871.583		1282.041
Sig.		.889	1.000	.060	.139		.217	.152	1.000	0.626

"Means for groups in homogenous subsets are displayed"

Table 5
Effect of seasonal variation on leachate characteristics.

Analysis of Variance (general parameters)

		Sum of Squares	Df	Mean Square	F	Sig.
Ammoniacal Nitrogen	Between Groups	278552.203	11	25322.928	0.140	.999
	Within Groups	4327612.404	24	180317.183		
	Total	4606164.607	35			
Biological Oxygen Demand	Between Groups	5475576.375	11	497779.670	0.025	1.000
	Within Groups	481091014.935	24	20045458.956		
	Total	486566591.310	35			
Chemical Oxygen Demand	Between Groups	25263408.512	11	2296673.501	0.014	1.000
	Within Groups	4064146391.529	24	169339432.980		
	Total	4089409800.041	35			
Chloride	Between Groups	7070322595.752	11	642756599.614	0.369	.956
	Within Groups	41755270164.994	24	1739802923.541		
	Total	48825592760.746	35			
Colour	Between Groups	35114602.415	11	3192236.583	0.232	.992
	Within Groups	329785635.446	24	13741068.144		
	Total	364900237.861	35			
Oil & Grease	Between Groups	15.031	11	1.366	1.668	.142
	Within Groups	19.658	24	.819		
	Total	34.690	35			
pH	Between Groups	.308	11	.028	0.686	.739
	Within Groups	.979	24	.041		
	Total	1.286	35			
Sulphate	Between Groups	456172062.567	11	41470187.506	0.465	.907
	Within Groups	2140932280.067	24	89205511.669		
	Total	2597104342.634	35			
Sulphide	Between Groups	231585.080	11	21053.189	0.932	.528
	Within Groups	542133.853	24	22588.911		
	Total	773718.933	35			
Total Alkalinity	Between Groups	85549565.285	11	7777233.208	1.304	.281
	Within Groups	143150465.906	24	5964602.746		
	Total	228700031.190	35			
Total Dissolved Solid	Between Groups	3463101439.120	11	314827403.556	0.043	1.000
	Within Groups	174045782164.563	24	7251907590.190		
	Total	177508883603.682	35			
Total Hardness	Between Groups	95924313.556	11	8720392.141	2.236	.048
	Within Groups	93603907.398	24	3900162.808		
	Total	189528220.954	35			
Total Kjeldahl Nitrogen	Between Groups	1271572.167	11	115597.470	0.624	.790
	Within Groups	4443085.435	24	185128.560		
	Total	5714657.602	35			
Total Nitrogen	Between Groups	258828.927	11	23529.902	0.101	1.000
	Within Groups	5575008.967	24	232292.040		
	Total	5833837.894	35			
Total Phenol	Between Groups	214.757	11	19.523	0.402	.941
	Within Groups	1165.636	24	48.568		
	Total	1380.394	35			
Total Phosphorus	Between Groups	2986.944	11	271.540	7.881	.000
	Within Groups	826.958	24	34.457		
	Total	3813.902	35			
Total Suspended Solid	Between Groups	264230.096	11	24020.918	1.069	.424
	Within Groups	539477.952	24	22478.248		
	Total	803708.048	35			

Analysis of Variance (metals)

		Sum of Squares	Df	Mean Square	F	Sig.
Calcium	Between Groups	1236678.767	11	112425.342	1.121	0.388
	Within Groups	2406460.720	24	100269.197		
	Total	3643139.487	35			
Cadmium	Between Groups	2.361	11	0.215	5.180	0.000
	Within Groups	.994	24	0.041		
	Total	3.355	35			
Chromium	Between Groups	5.453	11	0.496	8.022	0.000
	Within Groups	1.483	24	0.062		
	Total	6.937	35			
Copper	Between Groups	3.382	11	0.307	.197	0.996
	Within Groups	37.377	24	1.557		
	Total	40.758	35			
Iron	Between Groups	79.264	11	7.206	3.567	0.004
	Within Groups	48.479	24	2.020		
	Total	127.742	35			
Potassium	Between Groups	14469395.673	11	1315399.607	1.353	0.257
	Within Groups	23327847.646	24	971993.652		
	Total	37797243.319	35			
Magnesium	Between Groups	5205272.507	11	473206.592	2.558	0.026
	Within Groups	4439550.390	24	184981.266		

(*continued on next page*)

Table 5 (*continued*)

Analysis of Variance (general parameters)						
		Sum of Squares	Df	Mean Square	F	Sig.
	Total	9644822.897	35			
Sodium	Between Groups	188968384.139	11	17178944.013	1.140	0.376
	Within Groups	361791359.909	24	15074639.996		
	Total	550759744.048	35			
Zinc	Between Groups	73.483	11	6.680	3.036	0.011
	Within Groups	52.801	24	2.200		
	Total	126.283	35			
Nickel	Between Groups	169.120	11	15.375	8.329	0.000
	Within Groups	44.301	24	1.846		
	Total	213.421	35			
Lead	Between Groups	100.913	11	9.174	10.597	0.000
	Within Groups	20.777	24	0.866		
	Total	121.690	35			

Although the rate, at which hardness decreased, was different in initial and later stage; up to middle age, the hardness value reduced gradually but in later stage, a sharp fall in hardness value was observed.

Post Hoc analysis for calcium showed that the mean values of calcium in HWL1 were significantly different from HWL2 and HWL3 whereas between HWL2 and HWL3, no significant difference in the mean values was observed. Study of the mean values revealed that with an increase in landfill age, Ca values were decreasing, and the decline was sharper in later years of landfill. The trend shown by calcium was validated by the results of Post Hoc analysis of TH, as they both are interrelated parameters and showing the same trend. Post Hoc analysis for copper showed that there was no significant difference between the mean values of copper for HWL3 and HWL1, whereas HWL2 mean values were significantly different from both HWL3 and HWL1. Further study of means revealed that copper concentration increased up to age of HWL2 (11 years) and then it decreased back significantly, even lower than the initial concentration. Analysis of iron showed that there was no significant difference between the mean values of iron for HWL1 and HWL3 and similarly for HWL1 and HWL2 but there was a significant difference between the mean values of HWL2 and HWL3. Overall variation of means showed that iron concentration in leachate first increased up to middle age (10–15 years) and then decreased when landfill approached the maturity (20 years). The same trend was observed in Post Hoc analysis of zinc also, where the mean values for zinc increased up to a landfill age corresponding to HWL2 (11 years) and then started to decrease as landfill age approached to 20 years.

Post Hoc analysis of potassium and magnesium showed a trend similar to calcium and total hardness but with a different slope. Results summarised in Table 4 expressed that the mean values of potassium and magnesium concentration for HWL3 significantly differed with mean values for HWL2 and HWL1. But no significant difference was observed between the mean values corresponding to HWL1 and HWL2. Study of means showed that potassium and magnesium concentrations were on a continuous decreasing path with an increase in landfill age, although the rate of decline was higher in initial age and got slower in later age, contradictory to the declining pattern of Ca and TH. Post Hoc analysis for sodium indicated that the mean values for HWL1 are significantly different from HWL2 and HWL3 whereas no significant difference was observed between the mean values of HWL2 and HWL3. Study of the mean values depicted that up to age of HWL2 (11 years) mean values increased slowly and after that it subsided sharply even beyond the initial concentration. A comparable pattern was observed for chloride also.

Overall study through ANOVA and Post Hoc analysis revealed that landfill age significantly affects the leachate's characteristics. For most of the general parameters, it was observed that up till middle age (10–15 years), mean concentration increases (although the rate of increment may be different) and during later age of landfill it started to decline (at different rate). For some parameters like TN, mean concentration becomes steady in later stage.

The possible explanation for these trends could be that with an increase in the age, the quantity of dumped material also increased and so the landfill height, which lead to increase in pressure, results into the release of various components to a peak concentration with increasing age. In the later years, landfill operation gets stopped and the pressure also gets stagnant, due to this, the concentration of majority of the parameters gets stabilised or it starts to decline. Here, one noteworthy observation is that in MSW landfills, even during post operation phase, anaerobic activities go on for a longer period which influence the release of different constituents. Also, in MSW landfills, during different phases of waste decomposition, different kind of acids are produced which influence the pH of leachate, which is a key parameter for defining the solubility of different constituents, mainly metals [32]. Both these pathways are restricted in HWL landfills because the waste dumped in landfills is neutralised first before dumping (therefore the pH of leachate is always in neutral range) and the majority of the waste is not biodegradable (thus restricting biological decomposition). The important "material alteration process" inside the HWL appears to be physical (Pressure) and chemical (release of chemical constituent and their interaction during percolation through wastes) rather than biological. Hence, the leachate characteristics of MWL and HWL may not be compared with each other. The chemical reactions occurring during the percolation are extremely complex which makes it very difficult and uncertain to predict the exact mechanism behind the nature and trends of HWL leachate.

Although there is not one specific common pattern followed by all the metals in Post Hoc analysis but the study of means shows that two dominant trends exist. A First trend exhibits an increase in metal concentration along with increase in landfill age (till middle age) and afterwards it subsides slowly. Another trend shows continuous decline in metal concentration with an increase in landfill age and total hardness also shows the similar trend. No specific reason could be analysed behind this pattern of general parameters and heavy metals concentration but with the help of trailing analysis, it is evident that landfill age has significant impact on characteristics of HWL leachate.

3.3. *Analysing the effect of seasonal variation on leachate characteristics*

To understand the effect of seasonal variation, monthly data is required and hence every month samples were drawn from different landfills and their results were analysed through ANOVA. During this analysis, age wise variation was overlooked and all the results were grouped on the basis of different months. Results of ANOVA are summarised in Table 5 which clearly shows that for majority of the parameters, the level of significance is greater than 0.05. This leads to acceptance of null hypothesis that seasonal variation does not affect the leachate characteristics for many of the parameters including ammoniacal nitrogen, COD, BOD, chloride, colour, oil and grease, pH, sulphate,

Table 6
Post Hoc analysis (Seasonal Variation).

	Total Phosphorus				Total hardness			Iron			
N	**Month**	**1**	**2**	**3**	**Month**	**1**	**2**	**Month**	**1**	**2**
3	Nov'18	20.916			July'19	5155.119		Oct'18	1.709	
3	July'19	27.811			Jan'19	6446.304	6446.304	Sept'18	4.307	4.307
3	Jan'19	28.151			Nov'18	7236.317	7236.317	July'19	5.049	5.049
3	Oct'18	28.793			Dec'18	7462.388	7462.388	May'19	5.062	5.062
3	Feb'19	29.857			March'19	8109.031	8109.031	March'19	5.378	5.378
3	April'19	31.459			Feb'19	8389.436	8389.436	April'19	5.559	5.559
3	June'19	31.806	31.806		Oct'18	8440.190	8440.190	Jan'19	5.643	5.643
3	March'19	32.479	32.479		April'19	8551.000	8551.000	Aug'18	5.677	5.677
3	May'19	33.186	33.186		June'19	8754.777	8754.777	June'19	5.882	5.882
3	Dec'18	34.357	34.357		May'19	8763.833	8763.833	Feb'19		6.082
3	Aug'18		48.898	48.898	Aug'18	10721.952	10721.952	Nov'18		6.570
3	Sept'18			55.750	Sept'18		11524.984	Dec'18		8.427
Sig.		.239	.054	.945	Sig.	.069	.127	Sig.	.051	.056

	Cadmium				Chromium			
N	**Month**	**1**	**2**	**3**	**Month**	**1**	**2**	**3**
3	August'18	0.023			September'18	0.348		
3	October'18	0.037	0.037		December'18	0.435		
3	September'18	0.059	0.059	0.059	May'19	0.545		
3	November'18	0.193	0.193	0.193	February'19	0.551		
3	January'19	0.538	0.538	0.538	July'19	0.570		
3	March'19	0.589	0.589	0.589	January'19	0.578		
3	December'18	0.603	0.603	0.603	April'19	0.594		
3	June'19	0.617	0.617	0.617	March'19	0.596		
3	July'19	0.619	0.619	0.619	November'18	0.664	0.664	
3	May'19		0.632	0.632	June'19	0.667	0.667	
3	February'19			0.644	October'18		1.389	1.389
3	April'19			0.650	August'18			1.726
Sig.			.052	.052	Sig.	.055	.903	.054	.870

	Nickel								
N	**Month**	1	2	3	4	5			
3	November'18	0.158							
3	October'18	0.528	0.528						
3	September'18	1.525	1.525	1.525					
3	August'18	2.359	2.359	2.359	2.359				
3	June'19		4.348	4.349	4.349	4.349			
3	July'19		4.501	4.501	4.501	4.501			
3	May'19			4.625	4.625	4.625			
3	April'19			5.104	5.104	5.104			
3	January'19			5.408	5.408	5.408			
3	February'19			5.483	5.483	5.483			
3	March'19				5.751	5.751			
3	December'18					7.400			
	Sig.	.699	.053	.054	.152	.261			

N	**Zinc**			**Lead**					
3	**Month**	**1**	**2**	**Month**	**1**	**2**	**3**	**4**	
3	June'19	0.512		August'18	0.647				
3	May'19	0.526		September'18	1.242	1.243			
3	December'18	0.538		October'18	1.817	1.817	1.817		
3	March'19	0.602		November'18	1.849	1.849	1.849		
3	January'19	0.618		June'19	2.833	2.833	2.833		
3	July'19	0.623		July'19	2.923	2.923	2.923		
3	February'19	0.734		May'19	3.124	3.124	3.124		
3	April'19	0.738		March'19		3.603	3.603		
3	August'18	1.759	1.759	April'19		3.889	3.889		
3	October'18	2.311	2.311	February'19			4.078		
3	November'18	3.417	3.417	January'19			4.374		
3	September'18		5.206	December'18				7.274	
	Sig.	.443	.222	Sig.	.102	.065	.083	1.000	

"Means for groups in homogenous subsets are displayed"

sulphide, total alkalinity, total dissolved solids, total kjeldahl nitrogen, total nitrogen, total phenol and total suspended solid. Similarly, for metals like calcium, copper, potassium, sodium has level of significance >0.05, which again leads to acceptance of hypothesis and implies that the seasonal variation does not has significant impact on concentration of these metals in leachate.

For certain parameters like total phosphorus, total hardness, cadmium, chromium, iron, magnesium, zinc, nickel and lead, the significance level was less than 0.05 which indicates rejection of null hypothesis and implies that these parameters have significant impact of seasonal variation. Therefore, Post Hoc analysis with subset for alpha as 0.05 and harmonic mean sample size of 3 was carried out to study this impact in detail. Results of Post Hoc analysis for these parameters are summarised in Table 6, containing means for groups in homogeneous subsets.

It can be observed from Table 6 that although the seasonal variation significantly affects the concentration of these parameters but the dependency is very random and no specific pattern could be spotted. Post Hoc analysis of heavy metals also exhibited variation in means during different months and for nickel and lead, this variation is maximum.

Similar to the general characteristics, no specific trend was observed for metals in post hoc analysis or in the study of the means. The reason

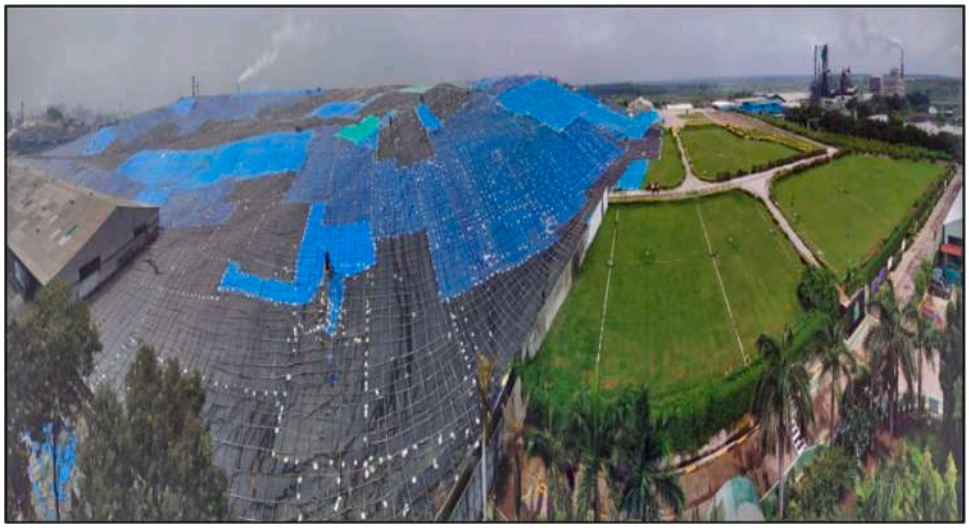

Fig. 4. Monsoon preparation at landfill.

behind this can be that the hazardous waste landfills are completely covered with HDPE liner, and all kinds of interaction of waste from external environment are minimised. After analysing the ANOVA and Post Hoc test results, it can be summarised that even though variation is observed in leachate characteristics due to the seasonal variation but no specific trend or relationship could be established between leachate characteristic and season of the year. Fig. 4 shows covering of landfill during monsoon season in order to avoid any seepage of rain water.

As the landfills remain completely covered during entire monsoon season and landfill operation was temporarily stopped at this time, direct interaction of rainwater with waste was avoided. But apart from the monsoon season, there may be sudden changes in atmospheric conditions like erratic rainfalls which may lead to change in leachate characteristics including increase or decrease in concentration of specific pollutants. These changes can occur in different seasons, and thus it can be attributed to "change due to seasonal variation" but as the frequency and intensity of such incidents are not same every year, any specific trend is not evident.

4. Conclusions

This research was dedicatedly oriented towards HWL leachate and the characterisation values indicated high and concurrent occurrence of different parameters like COD, TDS and ammoniacal nitrogen (35,000 mg/l, 300,000 mg/l, and 2300 mg/l, approximately in HWL 3) along with elevated concentration of heavy metals. Results of the statistical analysis indicated that the age of landfill has a significant impact on leachate quality although the impact is not the same for all the parameters. It was observed that the concentration of most of the pollutants first increased up to the middle age of landfill and later on either it got stabilised or it followed a decreasing trend. Few parameters (particularly in metals) showed continuous decreasing trend corresponding to an increase in landfill age. No direct impact of seasonal variation on leachate quality was observed. The concentration of different parameters was found to be varied with variation in months (seasonal variation) but they do not demonstrate any direct relationship with seasonal variation because the hazardous landfills are operated and closed in such a way that all kinds of interaction of landfill with the atmospheric condition are restricted and an enclosure is provided to the landfill through multilayer liner and cover system.

5. Future scope of the work

In the current study, for analysing the effect of seasonal variation, individual age variations were overlooked and parameter wise average readings of all the landfills were taken in account for all the months. In the next stage of the study, the effect of seasonal variation can be studied for individual landfills and then inter landfill comparison can be made to see if the seasonal variation exhibits the same behaviour for all landfill ages.

Information on funding source

This research did not receive any specific grant from funding agencies in the public, commercial, or not-for-profit sectors.

CRediT authorship contribution statement

Pratibha Gautam: Conceptualization, Methodology, Formal analysis and investigation, Writing - original draft. **Sunil Kumar:** Editing, Resources, Supervision.

Declaration of Competing Interest

The authors declare that they have no known competing financial interests or personal relationships that could have appeared to influence the work reported in this paper.

References

[1] M. Gholami, J. Torkashvand, R.R. Kalantari, K. Godini, A.J. Jafari, M. Farzadkia, Study of littered wastes in different urban land-uses: an environmental status assessment, J. Environ. Health Sci. Eng. 18 (2020) 915–924, https://doi.org/10.1007/s40201-020-00591-9.

[2] J. Torkashvand, H. Pasalari, A. Jonidi-Jafari, M. Kermani, O. Nasri, M. Farzadkia, Medical waste management in Iran and comparison with neighbouring countries, Int. J. Environ. Anal. Chem. (2020) 1–14, https://doi.org/10.1080/03067319.2020.1759570.

[3] L. Elleuch, M. Messaoud, K. Djebali, M. Attafi, Y. Cherni, M. Kasmi, A. Elaoud, I. Trabelsi, A. Chatti, A new insight into highly contaminated landfill leachate treatment using Kefir grains pre-treatment combined with Ag-doped TiO_2 photocatalytic process, J. Hazard. Mater. 382 (2020), 121119, https://doi.org/10.1016/j.jhazmat.2019.121119.

[4] D.P. Komilis, R.K. Ham, R. Stegmann, The effect of landfill design and operation practices on waste degradation behavior: a review, Waste Manag. Res. 17 (1999) 20–26, https://doi.org/10.1177/0734242X9901700104.

[5] T. Setiadi, S. Fairus, Hazardous waste landfill leachate treatment using an activated sludge-membrane system, Water Sci. Technol. 48 (8) (2003) 111–117, https://doi.org/10.2166/wst.2003.0459.

[6] E. Toufexi, V. Tsarpali, I. Efthimiou, M.S. Vidali, D. Vlastos, S. Dailianis, Environmental and human risk assessment of landfill leachate: an integrated approach with the use of cytotoxic and genotoxic stress indices in mussel and human cells, J. Hazard. Mater. 260 (2013) 593–601, https://doi.org/10.1016/j.jhazmat.2013.05.054.

[7] R. Cossu, Groundwater contamination from landfill leachate: when appearances are deceiving!, Waste Manag. 33 (2013) 1793–1794, https://doi.org/10.1016/j.wasman.2013.07.002.
[8] Y. Abu-Rukah, O. Al-Kofahi, The assessment of the effect of landfill leachate on ground-water quality-a case study. El-Akader landfill site—north Jordan, J. Arid Environ. 49 (3) (2001) 615–630, https://doi.org/10.1006/jare.2001.0796.
[9] H.N. Saleh, S. Valipoor, A. Zarei, M. Yousefi, F.B. Asghari, A.A. Mohammadi, F. Amiri, S. Ghalehaskar, A.M. Khaneghah, Assessment of groundwater quality around municipal solid waste landfill by using water quality index for groundwater resources and multivariate statistical technique: a case study of the landfill site, Qaem Shahr City, Iran, Environ. Geochem. Health 42 (2020) 1305–1319, https://doi.org/10.1007/s10653-019-00417-0.
[10] C. Pavelka, R.C. Loehr, B. Haikola, Hazardous waste landfill leachate characteristics, Waste Manag. 13 (1993) 573–580, https://doi.org/10.1016/0956-053X(93)90017-Q.
[11] P. Gautam, S. Kumar, S. Lokhandwala, Advanced oxidation processes for treatment of leachate from hazardous waste landfill: a critical review, J. Clean. Prod. 237 (2019), 117639, https://doi.org/10.1016/j.jclepro.2019.117639.
[12] M. Ghassemi, S. Quinlivan, J. Bachmaier, Characteristics of leachates from hazardous waste landfills, J. Environ. Sci. Health Part A Environ. Sci. Eng. 19 (1984) 579–620, https://doi.org/10.1080/10934528409375180.
[13] H. Luo, Y. Zeng, Y. Cheng, D. He, X. Pan, Recent advances in municipal landfill leachate: a review focusing on its characteristics, treatment, and toxicity assessment, Sci. Total Environ. 703 (2020), 135468, https://doi.org/10.1016/j.scitotenv.2019.135468.
[14] P. Kjeldsen, M.A. Barlaz, A.P. Rooker, A. Baun, A. Ledin, T.H. Christensen, Present and long-term composition of MSW landfill leachate: a review, Crit. Rev. Environ. Sci. Technol. 32 (4) (2002) 297–336, https://doi.org/10.1080/10643380290813462.
[15] R.D. Gibbons, D.G. Dolan, H. May, K. O'Leary, R. O'Hara, Statistical Comparison of leachate from hazardous, codisposal, and municipal solid waste landfills and, hazardous waste landfill leachate characteristics, Groundw. Monit. Remediat. 19 (4) (1999) 57–72, https://doi.org/10.1111/j.1745-6592.1999.tb00241.x.
[16] B.P. Naveen, D.M. Mahapatra, T.G. Sitharam, P.V. Sivapullaiah, T. V. Ramachandra, Physico-chemical and biological characterization of urban municipal landfill leachate, Environ. Pollut. 220 (2017) 1–12, https://doi.org/10.1016/j.envpol.2016.09.002.
[17] E.M. Pajooh, D. Weichgrebe, G. Cuff, Municipal landfill leachate characteristics and feasibility of retrofitting existing treatment systems with deammonification - a full scale survey, J. Environ. Manag. 187 (2016) 354–364, https://doi.org/10.1016/j.jenvman.2016.10.061.
[18] M.I. Al-Wabel, W.S. Al-Yehya, A.S. Al-Farraj, S.E. El-Maghraby, Characteristics of landfill leachates and bio-solids of municipal solid waste (MSW) in Riyadh City, Saudi Arabia, J. Saud. Soc. Agric. Sci. 10 (2011) 65–70, https://doi.org/10.1016/j.jssas.2011.03.009.
[19] B.P. Naveen, P.V. Sivapullaiah, T.G. Sitharam, Effect of aging on the leachate characteristics from municipal solid waste landfill, Jpn. Geotech. Soc. Spec. Publ. 2 (56) (2016) 1940–1945, https://doi.org/10.3208/jgssp.IND-06.
[20] Y.D. Kim, D.G. Lee, Comparative study on leachate in closed landfill sites: focusing on seasonal variations, J. Mater. Cycles Waste Manag. 11 (2009) 174–182, https://doi.org/10.1007/s10163-008-0246-9.
[21] V. Tsarpali, M. Kamilari, S. Dailianis, Seasonal alterations of landfill leachate composition and toxic potency in semi-arid regions, J. Hazard Mater. 233–234 (2012) 163–171, https://doi.org/10.1016/j.jhazmat.2012.07.007.
[22] E. Tinmaz, A. Ongen, Risks posed by unsanitary landfill leachate to groundwater quality, in: J.H. Tellam, M.O. Rivett, R.G. Israfilov, L.G. Herringshaw (Eds.), UrbanGroundwater Management and Sustainability, NATO Science Series (IV: Earth and Environmental Sciences), 74, Springer, 2006, pp. 259–268, https://doi.org/10.1007/1-4020-5175-1_21.
[23] F. Ruggeri, F. Faltin, R. Kenett, Descriptive statistics, in: Encyclopaedia of Statistics in Quality and Reliability, John Wiley & Sons, 2008, https://doi.org/10.1002/9780470061572.eqr178.
[24] K. Holm, N.J. Christman, Post hoc tests following analysis of variance, Res. Nurs. Health 8 (1985) 207–210, https://doi.org/10.1002/nur.4770080215.
[25] H. Bakraouy, S. Souabi, K. Digua, O. Dkhissi, M. Sabar, M. Fadil, Optimization of the treatment of an anaerobic pretreated landfill leachate by a coagulation-flocculation process using experimental design methodology, Process Saf. Environ. Prot. 109 (2017) 621–630, https://doi.org/10.1016/j.psep.2017.04.017.
[26] O. Dia, P. Drogui, G. Buelna, R. Dube, Hybrid process, electrocoagulation-biofiltration for landfill leachate treatment, Waste Manag. 75 (2018) 391–399, https://doi.org/10.1016/j.wasman.2018.02.016.
[27] D. Seibert, F.H. Borba, F. Bueno, J.J. Inticher, A.N. Modenes, F.R. Espinoza-Quinones, R. Bergamasco, Two-stage integrated system photo-electro-Fenton and biological oxidation process assessment of sanitary landfill leachate treatment: an intermediate products study, Chem. Eng. J. 372 (2019) 471–482, https://doi.org/10.1016/j.cej.2019.04.162.
[28] D. Seibert, H. Quesada, R. Bergamasco, F.H. Borba, L. Pellenz, Presence of endocrine disrupting chemicals in sanitary landfill leachate, its treatment and degradation by Fenton based processes: a review, Process Saf. Environ. Prot. 131 (2019) 255–267, https://doi.org/10.1016/j.psep.2019.09.022.
[29] Ministry of Environment, Forest and Climate Change: Solid Waste Management Rules, 2016, ⟨https://cpcb.nic.in/uploads/MSW/SWM_2016.pdf⟩.
[30] D. Fatta, A. Papadopoulos, M. Loizidou, A study on the landfill leachate and its impact on the groundwater quality of the greater area, Environ. Geochem. Health 21 (1999) 175–190, https://doi.org/10.1023/A:1006613530137.
[31] I.A. Talalaj, P. Biedka, I. Bartkowska, Treatment of landfill leachates with biological pretreatments and reverse osmosis, Environ. Chem. Lett. 17 (2019) 1177–1193, https://doi.org/10.1007/s10311-019-00860-6.
[32] J. Harmsen, Identification of organic compounds in leachate from a waste tip, Water Res. 17 (6) (1983) 699–705, https://doi.org/10.1016/0043-1354(83)90239-7.

Amit Kumar*, Gargi Das, Subhabrata Ray, Jay Mant Jha, Amit K. Thakur and Swapna Rekha Panda

Gas-liquid downward flow through narrow vertical conduits: effect of angle of entry and tube-diameter on flow patterns

https://doi.org/10.1515/ijcre-2020-0164
Received September 3, 2020; accepted December 5, 2020; published online February 15, 2021

Abstract: The present study investigates the flow pattern characteristics of air-water co-current down-flow in millichannels. The experiments have been performed in glass tube of diameter 0.0042 and 0.008 m. The fluids are injected through *Y* entry the included angle between the *Y* arms being 45°, 90°, 135°, and 180° (*T* Entry). The investigation reveals that the flow patterns are function of tube-diameter, and angle of fluid entry. Interestingly, stratified flow has been observed for steeper *Y* entry section at low liquid flow rates.

Keywords: downflow; entry effect; flow pattern transition; millichannel; stratified flow; two-phase flow.

1 Introduction

Gas-liquid flow phenomenon is common in various chemical, petrochemical, nuclear and power industries (Baba et al. 2012; Barnea, Luninski, and Taitel 1983; Barreto at al. 2015; Chung and Kawaji 2004; Fukano and Kariyasaki 1993; Ghanbarzadeh, Hanafizadeh, and Saidi 2012; Kawahara et al. 2002; Kreutzer et al. 2005; Kumar, Ray, and Das 2018). It is observed during process handling in condensers, cooling towers, distillation columns, boiler tubes etc. During the operation of equipment, the two phases distribute themselves in a variety of ways for different geometric and flow parameters. Knowledge of the flow distribution is essential to investigate and characterize the process for design calculations like heat and mass transfer, pumping power etc.

Currently there is a growing interest in miniaturized systems for process intensification, where scaling by numbering up approach (Biswas et al. 2015a, 2015c; Kannan, Ray, and Das 2016; Kumar et al. 2016; Kumar, Das, and Ray 2017, 2018) based on surface to volume ratio which depends on the size of the channel is highlighted (Biswas et al. 2015b). Therefore, in the present investigation we vary the conduit diameter and study gas-liquid downflow in millichannels, often used in monolith reactors (Devatine et al. 2017; Webb and Chung 2005). Downflow is the preferred orientation in industry (Saroha and Khera 2006) due to mal-distribution during up-flow in miniaturized systems, the design of fluid injection system is important. Nevertheless, only a few literature is available on gas-liquid downflow (Barnea, Shoham, and Taitel 1982; Bhagwat and Ghajar 2011, 2012; Crawford, Weinberger, and Weisman 1985; Galbiati and Andreini 1992; Kendoush and Al-Khatab 1994; Kumar et al. 2016; Kumar, Das, and Ray 2017; Milan, Borhani, and Thome 2014; Yamazaki and Yamaguchi 1979) (Table 1). Much of the discrepancies between the observations of the different researchers can be attributed to the difference in entry design and also the geometric parameters for the same entry say the length and included angle for *Y* entry, etc. Biswas and Greenfield have used a shorter entry length $200 < L_e/D < 380$ whereas Galbiati and Andreini have used $L_e/D > 1000$. Milan et al. (Milan, Borhani, and Thome 2013) have compared the influence of coaxial and ball bearing entry section on flow patterns.

In the present study, efforts have been made to understand the influence of the entry section on flow morphology during gas liquid downflow through a hydrophilic millichannel. The fluids are injected through symmetrically oriented channels of equal diameter intersecting at different angles at the junction to the main arm. Extensive experiments are performed in two different tube diameters under conditions where surface and viscous forces are comparable to its inertial and gravitational counterparts.

***Corresponding author: Amit Kumar**, Department of Chemical Engineering, Institute of Technology, Nirma University Ahmedabad, Ahmedabad, India, E-mail: amit.kumar.che.08@itbhu.ac.in. https://orcid.org/0000-0002-7405-8470
Gargi Das and Subhabrata Ray, Department of Chemical Engineering, Indian Institute of Technology Kharagpur, Kharagpur, India
Jay Mant Jha, Department of Chemical Engineering, MANIT Bhopal, Bhopal, India
Amit K. Thakur, Department of Chemical Engineering, University of Petroleum and Energy Studies, Dehradun, Uttarakhand, India. https://orcid.org/0000-0003-1048-2245
Swapna Rekha Panda, Department of Chemical Engineering, SRICT, Bharuch, Gujarat, India

Table 1: Pertinent literature showing entry effect on flow pattern in gas-liquid downflow.

Literatures	ID (mm)	Entry section	Method	Observation
(Golan and Stenning 1969)	38.1	U-bend	Visual observations	Flow patterns
(Oshinowo and Charles 1974)	25.4	U-bend	Photography	Flow patterns
(Spedding and Nguyen 1980)	45.5	*T* junction	Photography	Flow pattern
(Dvora Barnea, Shoham, and Taitel 1982)	25, 51	*T* junction	Conductance probe	Flow pattern prediction correlation
(Yamazaki and Yamaguchi 1979)	40, 80	Porous plate	Visual observations	Flow regime map
(J. Biswas and Greenfield 1985)	0.5–7.1	*Y* junction	Visual observations	Flow pattern
(Kendoush and Al-Khatab 1994)	38	*T* mixer	Direct visual observations	Flow regime map, pressure measurement
(Usui 1989)	16, 24	U-bend	Conductance probe	Local void fraction and prediction correlation
(Kim et al. 2004)	4	Porous sparger	Conductance probe	Neural network methodology, local two phase parameter, interfacial structure
(Young, Ishii, and Seok 2008)	25.4, 50.8	Porous sparger	Conductance probe	Neural network methodology, flow regime identification
(Bhagwat and Ghajar 2014)	12.7	Spiral mixer	High speed camera, Conductance probe	Local void fraction prediction correlation
(Milan, Borhani, and Thome 2013)	8.8	Ball mixer, coaxial injector	High speed camera Film thickness	Flow pattern map
(Almabrok et al. 2016)	10.16	U-bend	Probe, wire mesh sensor	Bend effects, film thickness correlations
(Qiao, Mena, and Kim 2017)	50.8	Sparger without FS, sparger with FS, 90° elbow	High speed camera, Conductance probe	Flow regime map, local two phase parameter, pressure drop analysis
(Kumar, Das, and Ray 2017)	2.5 – 12.5	*T* junction	High speed camera	Flow pattern transition correlation
Present study	2.5 – 12.5	*T* and *Y* junction	High speed camera	Flow pattern map

2 Experimentation

The experimental setup consists of fluid handling system (pump, flow meters, compressor, and valves), gas-liquid separator, and test rig (Figure 1). The test rig panel comprises glass tubes of internal diameter 4.2 and 8 mm (Eötvös number of 2.4 and 8.7 respectively) with the corresponding length to diameter (L/D) ratio being 380 and 200 respectively. In each conduit, the experiments are performed for four different *Y* inlets with included angle of 45°, 90°, 135°, and 180° (*T* Entry) Figure 2.

Clean, filtered and deionized water and air have been used as the test fluids clean water is stored in a 0.5 m^3 tank and circulated to the test section by centrifugal pump of maximum pressure 294.3 kPa. The measurement of the water flow rate has been gauged by an electromagnetic flow meter (Krohne Marshall) of range (0–1.5 m^3/h) and measurement accuracy ± 0.5%.

A dual stage reciprocating compressor is used to supply the air followed by an air filter and a pressure regulator at 1 atm (gauge) pressure and 25–32 °C temperature. A thermal mass flow meter (Siargo, China, Model no. MF5012) range 3–300 SLPM and accuracy within ± 1.5% is used to meter the air flow rate. For measurement of low air flow rate, rotameters ranging from 0–1, 0–3, and 1–5 SLPM have also been installed parallel to the mass flow meter. Three way valves direct the two phases into either of the conduits.

The experiments are carried out at superficial velocities ranging from 0.01 to 3 m/s for air and 0.1–30 m/s for water at a temperature of 25–32 °C and at a constant pressure of 1.8 atm (gauge). The water flow rate is kept constant while air flow is increased in steps of 0.1 L/min allowing sufficient time for the system to stabilize after each step. After flowing through the test section, the fluids are gravity separated and water is recirculated back to the test rig.

The flow patterns are observed at a distance of 0.8–1 m from the entry ($L/D > 180$) to ensure fully developed flow. A high speed camera (PHANTOM LC-320, M/s Vision Research) has been used to record images at the visualization section, uniformly backlit with a LED panel. The videos are recorded at a speed of 200–400 frame/s for a period of 30–60 s. This has ensured sufficient speed to reveal the prevailing flow structure and record at least five repetitions of the same flow distribution.

3 Result and discussion

We observed mainly five different types of flow pattern over the entire range of experimentation namely, stratified flow,

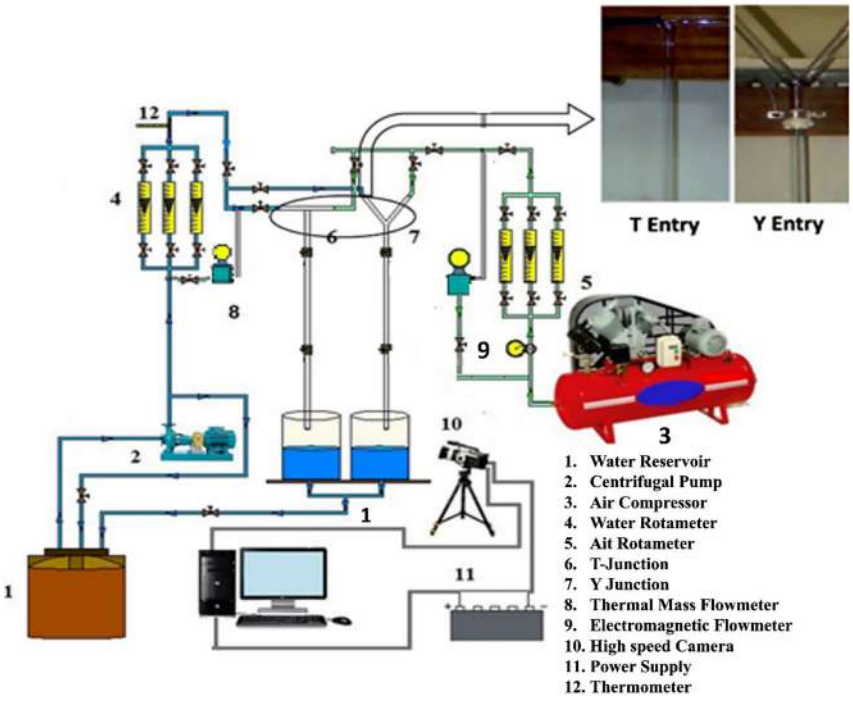

Figure 1: Schematics of the experimental setup.

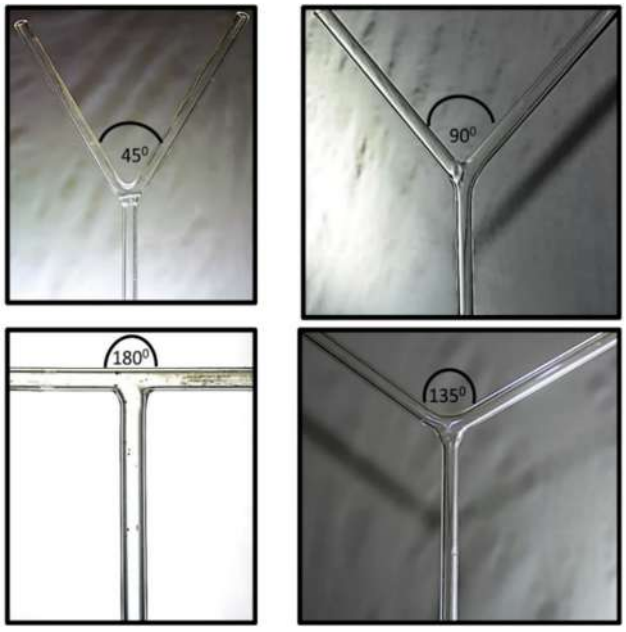

Figure 2: Different types of entry sections (D = 0.0042 mm).

falling film flow, slug flow, bubbly flow, and annular flow. Figure 3 shows the flow patterns observed in 0.0042 m tube with an Y angle of 45°, 90°, 135°, and 180°. The characteristics of all flow patterns except stratified flow are similar to the flow pattern observed by the Kumar et al. 2016, while stratified flow has been observed for Y junction only. It is characterized by smooth air water interface falling side by side through tube wall. Apart from these flow patterns, we also observe flow patterns having mixed characteristics of two prevalent flow patterns as bubbly-slug and slug-annular.

3.1 Effect of entry section

The range of existence of the different flow patterns are presented as maps plotted with liquid flow rate as ordinate

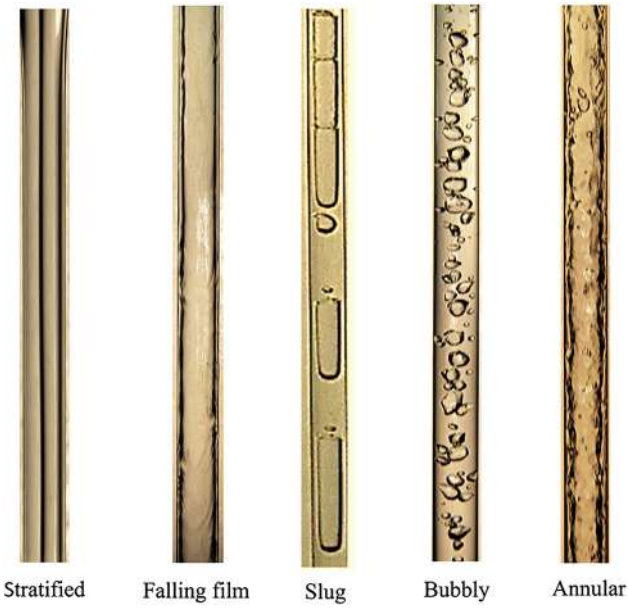

Figure 3: Different flow patterns observed in 0.0042 m tube of Y entry.

and air flow rate as abscissa. Figures 4 and 5 shows flow pattern map for 0.0042 and 0.008 m diameter conduit respectively. The figures clearly show that the flow patterns have been influenced by the change in entry section. Both the figures reveal that the flow patterns agree qualitatively for the different fluid injection systems at moderate to high velocities although the transition boundaries between the adjacent flow patterns appear to be displaced. Nevertheless, they stand along almost parallel lines in both the figures. An increase in Y angle increases the range of slug flow which is maximum for the T entry, whereas, falling film flow occurs for higher liquid flow rates at lower Y angles. This can be attributed to the greater pinching effect at the T.

The slug-annular to annular and slug to bubbly transitions appear to be only marginally influenced by the entry angle. Regardless of the angle between the fluid entry arms, annular flow occurs for low liquid and high gas flow rates and bubbly flow exist for low gas and high liquid flow rates.

At the lower liquid flow rates ($J_L < 0.03$ m/s) we observe that for two phases conflicting at right angles (included angle (γ) = 180°, T junction) the gas always flow as the central core enclosed by annular water film, the configuration termed as falling film flow.

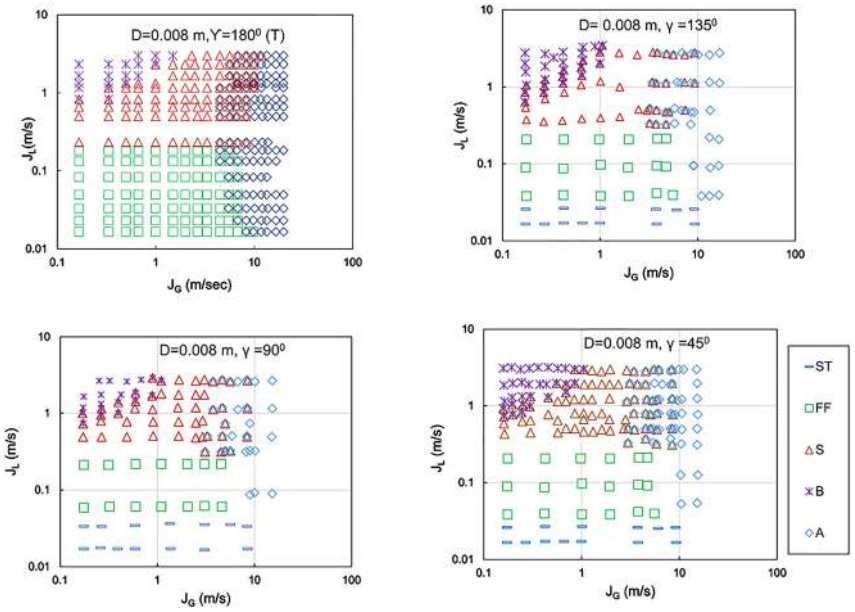

Figure 4: Flow pattern map for D = 0.008 m (B = Bubbly, S = Slug, FF = Falling film, ST = Stratified flow, SA = Slug-Annular, A = Annular).

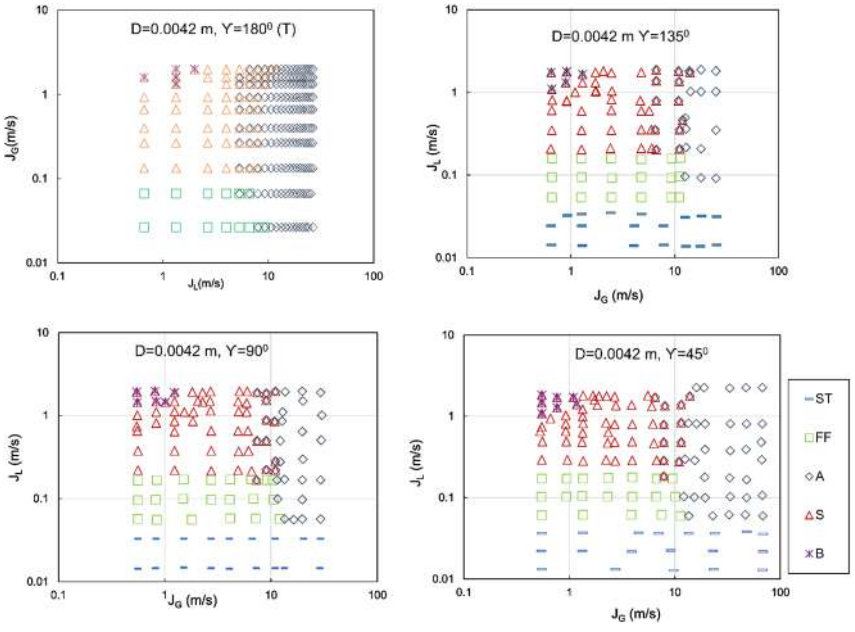

Figure 5: Flow pattern map for D = 0.0042 m (B = Bubbly, S = Slug, FF = Falling film, ST = Stratified flow, SA = Slug-Annular, A = Annular).

However, under the same flow conditions when the angle between the entry arms is changed, air and water can be made to flow side by side instead of water enclosing the gas core.

This unique flow morphology resembles stratified flow in horizontal conduits. Only one study Biswas and Greenfield 1985 [35] has reported this distribution during gas-liquid down flow but no systematic study has yet discussed the condition of existence and characteristics of stratified gas-liquid down flow.

The formation of stratified flow can be noted from Figure 6 that shows the influence of entry section on the wetting mechanism and hence the flow pattern. Water and air enter from the left and right limb of the *Y*. We observe that falling film flow can occur only when the water phase can wet the junction completely while it flows down. Attempts have also been made to understand stratified flow characteristics as a function of conduit diameter, angle of *Y* entry and phase velocities. The water flows down as a film while air is form a continuous core. In case of a *Y* junction (Figure 6a) the down flowing water needs to have sufficient inertial force resulting in an upslope climb if it has to wet the junction and initiate falling film flow. We observe that the angle of entry has a significant influence on the transition from stratified to falling film and falling film to slug flow (Figure 6). A decrease in the *Y* angle increases the region occupied by stratified flow by shifting the transition to falling film flow towards higher liquid flow rate. This always occurs at a *T* junction where the phases enter horizontally from diametrically opposite points (Figure 6b). The water stream entering to flow in the same direction and reach the opposite end of the junction. Adherence of water to the hydrophilic wall makes a complete annulus at the junction that continues to supply the downflowing annular stream.

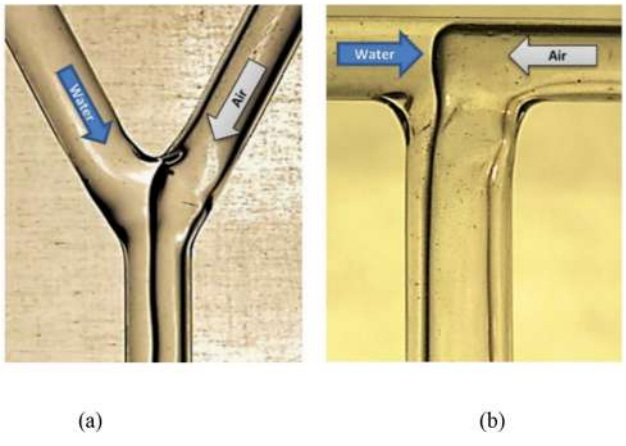

Figure 6: Formation of stratified flow at a *Y* ($\gamma = 45^{\circ}$) and falling film flow at a *T* entry ($D = 0.008$ m).

For a steep up-tilt, water drains down without wetting the junction completely and initiates stratified flow. For pronounced surface forces (low conduit diameter) and sufficient liquid inertia (higher liquid velocity), the water can wet the junction and inhibit the formation of stratified flow. Thus stratified flow forms in a conduit for *Y* angles steeper than a critical and only falling film flow is observed for 0.0025 and 0.0042 m diameter conduits. Table 2 provides a pictorial comparison of the flow configurations observed in a 0.0042 m diameter conduit for a *T* and a *Y* entry ($\gamma = 45^{\circ}$) under identical flow conditions.

For a better presentation, the flow pattern maps have been redrawn by incorporating the transition boundaries for different *Y* angles in Figure 7 (a) for a 0.0042 m conduit diameter and transition boundaries at included angles 45° and 135° in Figure 7 (b) and (c) respectively.

Table 2: A comparison of flow distributions in a 0.0042 m diameter conduit for fluid injection via a *T* and a *Y* entry ($\gamma = 45^{\circ}$) for identical phase flow rates.

J_L (m/s)	J_G (m/s)	*T* junction	*Y* junction
0.03	1.3	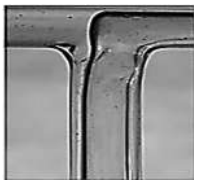	
0.3	2.9		
0.3	5.8		
0.5	1.3		
0.5	2.9		
0.5	5.6		

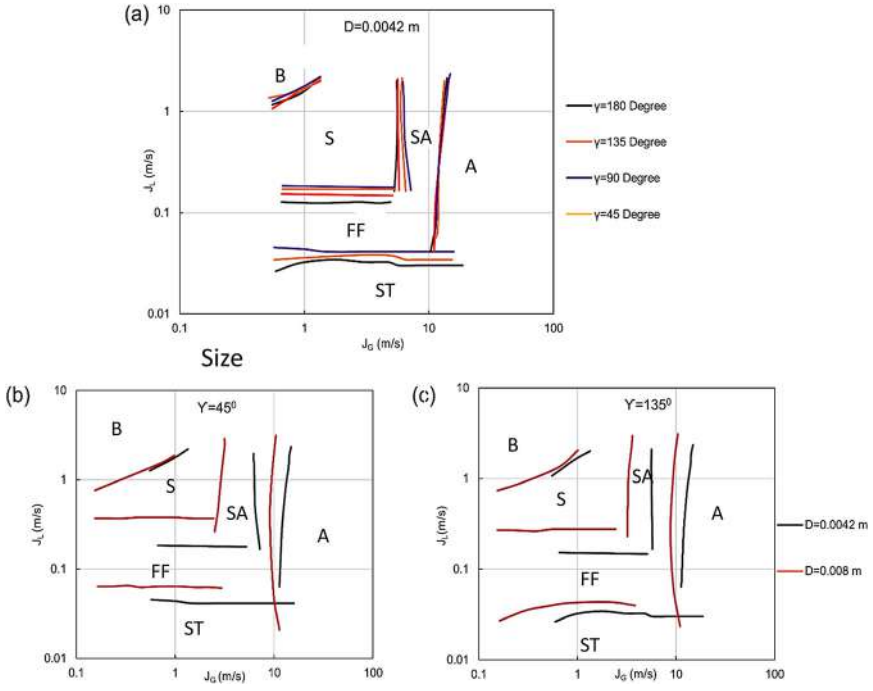

Figure 7: (a): Effect of *Y* angle on flow patterns in 0.0042 m diameter conduit (b): Effect of conduit diameter on the existence of flow patterns for a *Y* angle of 45° and (c) for a *Y* angle of 135°.

For moderate gas flow rates ($5<J_G<10$ m/s), the transition between stratified and falling film flow is primarily a function of angle of entry and relatively independent of gas flow rate.

With increasing gas velocity, the interface becomes wavy but the fluids continue to flow without mixing till a critical gas flow rate, beyond which the interfacial waviness is significantly pronounced to entrain liquid droplets. This marks the onset of slug-annular flow. The transition between stratified and slug-annular transition appear to be very sensitive to changes in gas and liquid flow rates and for very low liquid flow rate, the flow pattern shifts directly from stratified to annular flow without entering the intermittent flow regime. In this region, annular flow is wavy in nature. We can thus conclude that the width of the stratified liquid layer increases with liquid flow rate as expected while an increase in gas velocity increases the interfacial waviness, thus resulting in the formation of liquid droplets and the onset of annular flow.

3.2 Influence of tube-diameter

With a decrease in pipe diameter, the zone of existence of stratified flow on the flow pattern map shrinks towards higher gas flow rates and lower liquid flow rates.

Any disturbance on the gas-liquid interface causes the liquid to touch the pipe wall, thereby bridging the entire cross section. This flow situation is very conducive for the formation of slug and slug-annular flow and hence for small diameter pipes, slug and slug-annular flow occupy a major portion of the flow pattern map. To summaries we have observed stratified flow very low liquid flow rates ($J_L \leq 0.03$ m/s) in tubes with a *Y* entry.

This suggests that stratified downflow of the two phases may become one of the dominant flow patterns for larger diameter conduits with *Y* entry sections.

4 Conclusions

The present study addresses the effect of tube-diameter and entry section on gas-liquid downflow through millichannels. Five main types of flow patterns namely, bubbly flow, slug flow, annular flow, falling film flow and stratified flow have been observed. Falling film flow gives way to stratified flow at low liquid velocities ($J_L < 0.03$ m/s) for a *Y* entry. The range of slug flow increases with decrease of tube diameter due to the increasing influence of interfacial tension in smaller dimension and in 0.0042 m diameter conduit, we observe bubbly-slug rather than bubbly flow under the present flow conditions

The range of bubbly and slug flow is higher in case of *T* entry due to the greater pinching effect, while falling film flow occurs for higher liquid flow rates with decreasing included angle of *Y* entry.

Notation

D: diameter of conduit
J: Superficial velocity
S: Interfacial area
U: In situ velocity
Eo: Eotvos number
Re: Reynolds number

Greek symbols

ρ: Density
σ: Surface tension

Subscripts and superscripts

G: Gas
L: Liquid

Author contribution: All the authors have accepted responsibility for the entire content of this submitted manuscript and approved submission.
Research funding: None declared.
Conflict of interest statement: The authors declare no conflicts of interest regarding this article.

References

Almabrok, A. A., A. M. Aliyu, L. Lao, and H. Yeung. 2016. "International Journal of Multiphase Flow Gas/Liquid Flow Behaviours in a Downward Section of Large Diameter Vertical Serpentine Pipes." *International Journal of Multiphase Flow* 78: 25–43.

Baba, S., N. Ohtani, O. Kawanami, K. Inoue, and H. Ohta. 2012. "Experiments on Dominant Force Regimes in Flow Boiling Using Mini-Tubes." *Frontiers in Heat and Mass Transfer* 3 (4). https://doi.org/10.5098/hmt.v3.4.3002.

Barnea, D., O. Shoham, and Y. Taitel. 1982. "Flow Pattern Transition for Vertical Downward Two Phase Flow." *Chemical Engineering Science* 37 (5): 741–4.

Barnea, D., Y. Luninski, and Y. Taitel. 1983. "Flow Pattern in Horizontal and Vertical Two Phase Flow in Small Diameter Pipes." *The Canadian Journal of Chemical Engineering* 61 (5): 617–20.

Barreto, E. X., J. L. G. Oliveira, and J. C. Passos. 2015. "Frictional Pressure Drop and Void Fraction Analysis in Air-Water Two-phase Flow in a Microchannel." *International Journal of Multiphase Flow* 72: 1–10.

Bhagwat, S. M., and A. J. Ghajar. 2011. "Flow Patterns and Void Fraction in Downward Two Phase Flow." In *2011 ASME Early Career Technical Conference, Fayetteville, Arkansas, The American Society of Mechanical Engineers*, Vol. 7.

Bhagwat, S. M., and A. J. Ghajar. 2012. "Similarities and Differences in the Flow Patterns and Void Fraction in Vertical Upward and Downward Two Phase Flow." *Experimental Thermal and Fluid Science* 39: 213–27.

Bhagwat, S. M., and A. J. Ghajar. 2014. "A Flow Pattern Independent Drift Flux Model Based Void Fraction Correlation for a Wide Range of Gas-Liquid Two Phase Flow." *International Journal of Multiphase Flow* 59: 186–205.

Biswas, J., and P. F. Greenfield. 1985. "Two Phase Flow through Vertical Capillaries – Existence of a Stratified Flow Pattern." I*nternational Journal of Multiphase Flow* 11 (4): 553–63.

Biswas, K. G., G. Das, S. Ray, and J. Kumar Basu. 2015a. "Mass Transfer Characteristics of Liquid-Liquid Flow in Small Diameter Conduits." *Chemical Engineering Science* 122: 652–61.

Biswas, K. G., G. Das, S. Ray, and J. Kumar Basu. 2015b. "Mass Transfer Characteristics of Liquid-Liquid Flow in Small Diameter Conduits." *Chemical Engineering Science* 122: 652–61.

Biswas, K. G., R. Patra, G. Das, S. Ray, and J. Kumar Basu. 2015c. "Effect of Flow Orientation on Liquid-Liquid Slug Flow in a Capillary Tube." *Chemical Engineering Journal* 262: 436–46.

Chung, P. M. Y., and M. Kawaji. 2004. "The Effect of Channel Diameter on Adiabatic Two-phase Flow Characteristics in Microchannels." *International Journal of Multiphase Flow* 30 (7-8 SPEC. ISS.): 735–61.

Crawford, T. J., C. B. Weinberger, and J. Weisman. 1985. "Two-Phase Flow Patterns and Void Fractions in Downward Flow Part I: Steady-State Flow Patterns." *International Journal of Multiphase Flow* 11 (6): 761–82.

Devatine, A., H. Chaumat, S. Guillaume, B. T. Tchibouanga, F. Durán Martínez, C. Julcour, and A. M. Billet. 2017. "Hydrodynamic Study of a Monolith-type Reactor for Intensification of Gas-Liquid Applications." *Chemical Engineering and Processing: Process Intensification* 122: 277–87.

Fukano, T., and A. Kariyasaki. 1993. "Characteristics of Gas-Liquid Two-phase Flow in a Capillary Tube." *Nuclear Engineering and Design* 141: 59–68.

Galbiati, L., and P. Andreini. 1992. "Flow Pattern Transition for Vertical Downward Two-phase Flow in Capillary Tubes. Inlet Mixing Effects." *International Communications in Heat and Mass Transfer* 19 (6): 791–99.

Ghanbarzadeh, S., P. Hanafizadeh, and M. H. Saidi. 2012. "Intelligent Image-Based Gas-Liquid Two-phase Flow Regime Recognition." *Journal of Fluids Engineering* 134 (6): 061302.

Golan, L. P., and A. H. Stenning. 1969. "Two-Phase Vertical Flow Maps." In *Proceedings of the Institution of Mechanical Engineers, Conference Proceedings*, 108–14. London, England: SAGE Publications.

Kannan, A., S. Ray, and G. Das. 2016. "Liquid-Liquid Flow Patterns in Reduced Dimension Based on Energy Minimization Approach." *AIChE Journal* 62 (00): 287–94.

Kawahara, A., P. Y. Chung, and M. Kawaji. 2002. "Investigation of Two-phase Flow Pattern, Void Fraction and Pressure Drop in a Microchannel." *International Journal of Multiphase Flow* 28 (9): 1411–35.

Kendoush, A. A., and S. A. W. Al-Khatab. 1994. "Experiments on Flow Characterization in Vertical Downward Two-Phase Flow." *Experimental Thermal and Fluid Science* 9 (1): 34–8.

Kim, S., S. S. Paranjape, M. Ishii, and J. Kelly. 2004. "Interfacial Structures and Regime Transition in Co-Current Downward Bubbly Flow." *Journal of Fluids Engineering* 126 (4): 528.

Kreutzer, M. T., F. Kapteijn, J. A. Moulijn, and J. J. Heiszwolf. 2005. "Multiphase Monolith Reactors: Chemical Reaction Engineering of Segmented Flow in Microchannels." *Chemical Engineering Science* 60 (22): 5895–916.

Kumar, A., S. Bhowmik, S. Ray, and G. Das. 2016. "Flow Pattern Transition in Gas-Liquid Downflow through Narrow Vertical Tubes." *AIChE Journal* 59 (00): 215–28.

Kumar, A., G. Das, and S. Ray. 2017. "Void Fraction and Pressure Drop in Gas-Liquid Downflow through Narrow Vertical Conduits-Experiments and Analysis." *Chemical Engineering Science* 171: 117–30.

Kumar, A., S. Ray, and G. Das. 2018. "Draining Phenomenon in Closed Narrow Tubes Pierced at the Top: An Experimental and Theoretical Analysis OPEN." *Scintific Reports* 8: 14114.

Milan, M., N. Borhani, and J. R. Thome. 2013. "Adiabatic Vertical Downward Air-Water Flow Pattern Map: Influence of Inlet Device, Flow Development Length and Hysteresis Effects." *International Journal of Multiphase Flow* 56: 126–37.

Milan, M., N. Borhani, and J. R. Thome. 2014. "A New Type of Flow Structure in Cocurrent Adiabatic Vertically Downward Air-Water Flow: Membrane Flow." *International Journal of Multiphase Flow* 58: 246–56.

Oshinowo, T., and M. E. Charles. 1974. "Vertical Two-phase Flow. I Flow Pattern Correlations." *The Canadian Journal of Chemical Engineering* 52 (6): 739–49.

Qiao, S., D. Mena, and S. Kim. 2017. "Inlet Effects on Vertical-Downward Air – Water Two-phase Flow." *Nuclear Engineering and Design* 312: 375–88.

Saroha, A. K., and R. Khera. 2006. "Hydrodynamic Study of Fixed Beds with Cocurrent Upflow and Downflow." *Chemical Engineering and Processing: Process Intensification* 45 (6): 455–60.

Spedding, P. L., and V. T. Nguyen. 1980. "Regime Maps for Air Water Two Phase Flow." *Chemical Engineering Science* 35 (4): 779–93.

Usui, K. 1989. "Vertically Downward Two-phase Flow, (II): Flow Regime Transition Criteria." *Journal of Nuclear Science and Technology* 26 (11): 1013–22.

Webb, R. L., and K. Chung. 2005. "Two-Phase Flow Distribution to Tubes of Parallel Flow Air-Cooled Heat Exchangers." *Heat Transfer Engineering* 26 (4): 3–18.

Yamazaki, Y., and K. Yamaguchi. 1979. "Characteristics of Cocurrent Two-Phase Downflow in Tubes: Flow Pattern, Void Fraction, Pressure Drop." *Journal of Nuclear Science and Technology* 16 (4): 245–55.

Young, J., M. Ishii, and S. Nam. 2008. "Instantaneous and Objective Flow Regime Identification Method for the Vertical Upward and Downward Co-Current Two-Phase Flow." *International Journal of Heat and Mass Transfer* 51: 3442–59.

Since January 2020 Elsevier has created a COVID-19 resource centre with free information in English and Mandarin on the novel coronavirus COVID-19. The COVID-19 resource centre is hosted on Elsevier Connect, the company's public news and information website.

Environmental Research 188 (2020) 109807

Contents lists available at ScienceDirect

Environmental Research

journal homepage: www.elsevier.com/locate/envres

Indirect impact of COVID-19 on environment: A brief study in Indian context

Snehal Lokhandwala*, Pratibha Gautam

Department of Environmental Science & Technology, Shroff S.R. Rotary Institute of Chemical Technology, Ankleshwar, Gujarat, 393135, India

ARTICLE INFO

Keywords:
Covid 19
Pandemic situation
Lockdown
Air quality index
Central pollution control board

ABSTRACT

Worldwide spread of COVID-19 in a quite short time has brought a dramatic decrease in industrial activities, road traffic and tourism. Restricted human interaction with nature during this crisis time has appeared as a blessing for nature and environment. Reports from all over the world are indicating that after the outbreak of COVID-19, environmental conditions including air quality and water quality in rivers are improving and wildlife is blooming. India has always been a hub of pollution with huge population, heavy traffics and polluting industries leading to high air quality index (AQI) values in all major cities. But after declaration of lockdown due to COVID-19, quality of air has started to improve and all other environmental parameters such as water quality in rivers have started giving a positive sign towards restoring. This paper provides evidence-based insight into improvement of air quality and environment during pre and post lockdown of this pandemic situation. An attempt has been made to visualize the improvement in the air quality using tools like satellite images of Indian atmosphere, results of onsite real-time monitoring at specific locations (Ghaziabad-highest polluting city of India) and Air quality index (AQI) calculated by central pollution control board of India.

1. Introduction

Coronaviruses (CoVs) are a group of viruses which affects human beings through zoonotic transmission. This is the third time in past two decades that novel virus has created pandemic condition, after Severe Acute Respiratory Syndrome (SARS) in 2003 and Middle East Respiratory syndrome corona virus (MERSCoV) in 2012 (Ramdan and Shaib, 2019; Zhong et al., 2003). Pertaining to the Corona virus (2019), it was on December 31, 2019 wherein first case was reported to WHO Country Office in Wuhan, China with symptoms of unexplained low respiratory infections. This was classified as “pneumonia of unknown etiology” as the cause of infection was not known. On January 12, 2020, WHO found that Corona virus was the reason of this infection in Wuhan and later on 11th February, WHO Director-General announced this novel CoV as ‘COVID-19’ which is an acronym of ‘Corona virus disease 2019’ (Cascella et al., 2020). Covid-19 contain a single-stranded RNA as nuclei material and are 65 nm - 125 nm in diameter (Shereen et al., 2020). The major causes of concern for Covid-19 includes its global scale transmission, repeated emergence, significant number of deaths, infection and mortality to care providers and multiplicative effect in vulnerable or susceptible groups.

Covid-19 was declared pandemic disease by Director General-WHO on 11th March, he also briefed regarding the 13-fold increase in positive cases in China and 114 countries suffering form 1, 18,000 positive cases and 4291 deaths till date (World Health Organization, 2020). In India the first confirmed positive case was reported on 30th January in a student from Thrissur district of Kerala who had returned home for a vacation from Wuhan University in China (India Today, 2020a) followed by two other cases on February 2 and 3 again in Kerala having the same history. As on 14th April, Ministry of Health & Family Welfare (MOHFW) reported 10,815 positive cases and 358 deaths covering 32 states in India. Fig. 1 shows the spread of COVID-19 from January 30, 2020 to April 14, 2020. It is evident from the figure that spread of corona virus became rapid after 15 March and started taking a horrible shape in entire country.

Presently in comparison to the top six affected countries viz USA, Italy, Spain, China, Germany and Iran, we in India have lesser capacity to serve patients. With a population of 1.2 billion, India has only 118 Government approved testing laboratories, 1.1363 beds per thousand patients (China has 4.2) and more than one million tests done. On the contrary, India has the highest recovery rate of 41.39% as compared to Italy (16.91%) and USA (3.17%) which is the direct effect of lockdown. Although, the researchers round the globe are rigorously working to find the cure of the infection caused by this deadly virus but unfortunately, till date no definite cure or vaccine has got developed. The only way to control the spread of this virus at this moment is suggested to be “social distancing”, which is being practiced by many countries at this crisis time and has led to reduction GHG emissions in air

* Corresponding author.
E-mail address: snehal.lokhandwala@srict.in (S. Lokhandwala).

https://doi.org/10.1016/j.envres.2020.109807
Received 20 April 2020; Received in revised form 6 June 2020; Accepted 6 June 2020
Available online 18 June 2020
0013-9351/

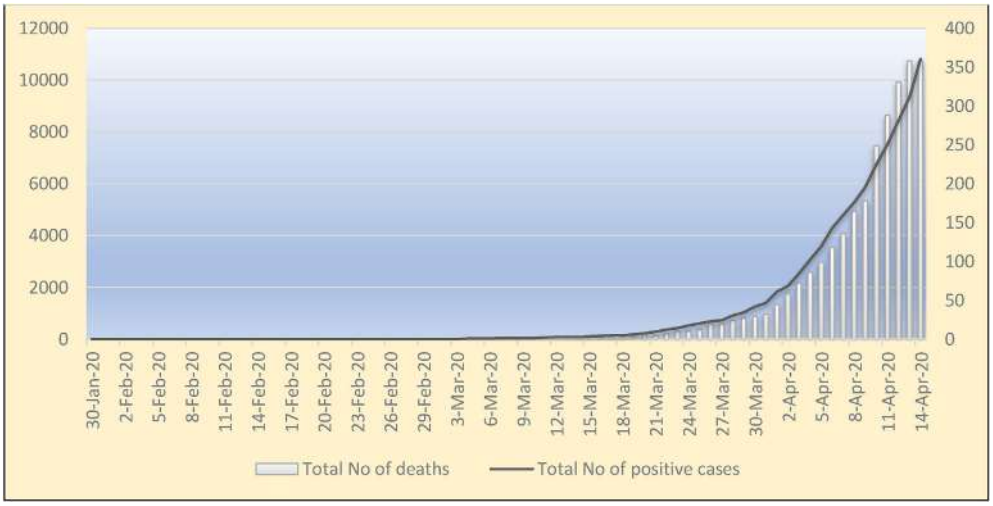

Fig. 1. Covid 19 in India from Jan 30, 2020 to April 14, 2020 (MOHFW-GOI, 2020).

(Zambrano-Monserrate et al., 2020) at global level.

During past two decades, India has witnessed an expeditious industrial growth which has certainly improved the standard of living of its people and it is also evident from the rising vehicular fleet on roads. But we have paid a heavy cost for this development in terms of poisoning the air we breathe. As per press release of World Health Organization (2nd May 2018), around 7 million people die every year from exposure to fine particles in polluted air (World Health Organization, 2018). State of India's Environment (SoE) report, 2019 have declared that 12.5% of all deaths in India are due to Air Pollution (India Today, 2020b). The environment in India was extremely degraded and all the pollutant levels and Air quality index left the limits way behind. Observing the increasing rate of corona cases in India and subsequent looming crisis, honourable prime minister of India, Shri Narendra Modi on March 24, 2020 declared a complete lockdown of 21 days for entire country during his live address to the nation, which was further extended for 19 days on April 14, 2020 in II phase followed by 14 days till 17th May in III phase and more 14 days in Phase IV. Various restrictions posed by GOI and subsequent lockdown, anthropogenic activities like industrial projects, vehicular movement, construction projects, tourism other common transportation activities witnessed a 'never before' stagnant phase. In India, apart from taking necessary administrative measures such as restriction on social gathering events, travel restrictions, containment of corona suspects and their treatment, Government of India (GOI) has directed the citizens to maintain adequate social distancing and to use personal protective equipment like masks. However, the COVID-19 has created a catastrophic situation for all and it would have adverse effect on Indian economy too (The Economic Times, 2020), there is positive side of the coin also which may alleviate the woeful facts of COVID-19. As many of the countries are observing self-quarantine and social distancing for a more than two months now, it has given the nature a "healing time" with reduced human interference in natural environment. Major impact of lockdown due to COVID-19 can be observed on air quality, which is being experienced by everyone and recorded in various official reports. Smog has given way to blue skies in cities like Delhi, marine life is seeing increased activity, pollution levels have dropped in almost all the metro cities and animals as well as birds are moving around on their own accord. It was also observed that in metro cities like Delhi, as the energy foot print was high, the lockdown has improved the air quality at higher scale (Mahato et al., 2020). Mandal and Pal (2020) in their studies on air quality of the four selected stone crushing clusters at Dwarka river basin of Eastern India noticed reduction of PM_{10} concentration from 189–278 μg/m^3 to 50–60 μg/m^3 after 18 days of commencement of lockdown. Analysis using WRF-AERMOD modelling system on actual and unfavourable meteorology revealed that even the predicted $PM_{2.5}$ increases in India due to unfavourable meteorology, the average concentration would still be under CPCB limits (Sharma et al., 2020). Although the pandemic situation is out of control for human beings but the positive side of it has made us to reconsider our lives and reorganize it in a way that has less impact on our planet. The situation today is a "reset" for nature and mankind, giving us a prospect to observe and analyse in and around.

The impact of air pollution on Indian population and their health was extensively studied in past by several researchers. The Urban air quality management strategies were planned which concentrated on emission inventory, control strategies, monitoring network and participation of public (Gulia et al., 2015). A general comparison between the major air pollutants was also studied and the impact of industrialization, transportation and other anthropogenic activities were analysed (Singh et al., 2007). In this paper information from several government and non-government agencies have been collected and analysed to understand the change in quality of various environmental factors such as air and water quality due to lockdown caused by Covid-19. Different tools like satellite images and Air Quality index (AQI) have been used to study the indirect effect of COVID-19 in Indian context. Outcomes of the study will help the policy makers to define the Post-Covid strategy for the country, as the pollution level which we were not able to achieve during last decade (even after applying all sort of technological advancement) have become a real thing due to lockdown. This study can also be used as a baseline study to analyse the health impact (specifically on sensitive receptors) due to reduction in air pollution.

2. Impact on air quality

2.1. Case study of Ghaziabad city

2.1.1. Study area

Ghaziabad is the biggest city of Western Uttar Pradesh, second largest industrial city of Uttar Pradesh and it's a part of National Capital Region. It has more or less the same environmental conditions as that of Delhi (National Capital). The 2011 Census data shows that Ghaziabad has urban agglomeration with population of 46.82 lacs indicating a decadal growth rate of 29.7% and density of 3971 individuals/km^2. District Ghaziabad lies between geo-coordinates 28° 40′ 12″ N and 77°25′12″ E with geographical area of 777.9 sq. km with rectangular dimensions. The city has adverse pollution problems mainly due to traffic congestion and dust. In a recently release IQAir 2019 World Air Quality report, it is found that out of 20 world's most polluted cities, 14

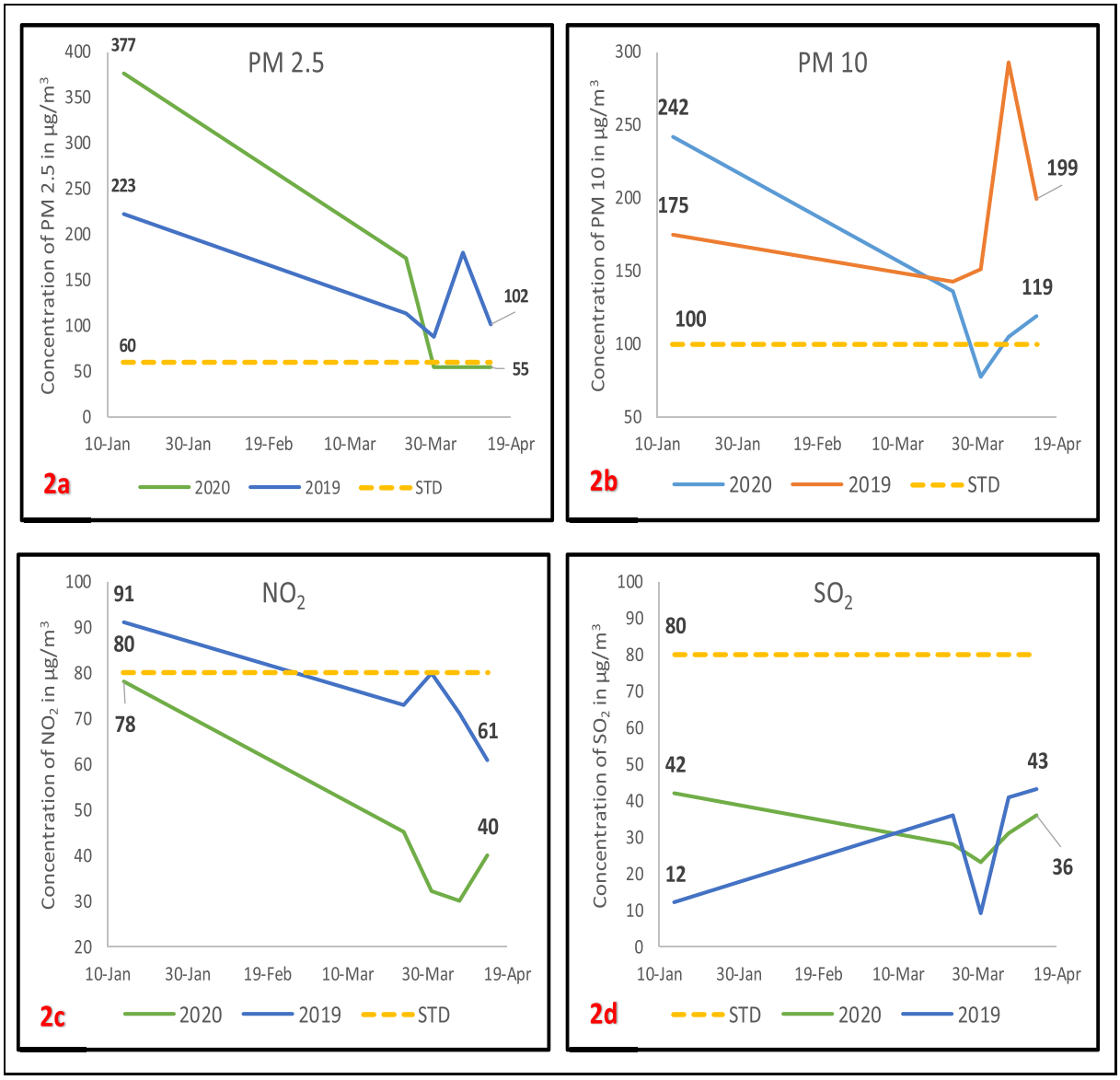

Fig. 2. Trends for pollutant concentration for Ghaziabad City (NAQI-CPCB, 2020).

are from India and Ghaziabad is in first place with $PM_{2.5}$ pollution level of 110.2 µg/m^3 in 2019 compared to the permissible limit of 60 µg/m^3 (for 24 h) (IQAir report, 2019). This indicates severe degree of air pollution which could not be controlled by state and central government even after several efforts. Therefore, Ghaziabad was selected as the study area and the things changed there in early 2020 when Government of India (GOI) declared a complete lockdown in country in order to prevent community transmission of corona virus. Similar steps were also taken in various part of world which negatively influenced the economy of those countries but had a positive impact on overall air quality (World Economic Forum, 2020).

2.1.2. *Environmental impact of lockdown period on Ghaziabad district*

In order to study the environmental impact of lockdown on the air quality of Ghaziabad District, 24 h average concentrations of four major pollutants of specific dates were compared to the concentration data of previous year and the results are compiled in Fig. 2a–d. Where Fig. 2a–d corresponds to the trends for PM2.5, PM10, Nitrogen dioxide (NO_2) and Sulphur dioxide (SO_2) respectively. Dates were randomly selected representing different weeks of different month where, initial three dates (10 January, 30 January and 19 February) show 'before lockdown' condition, fourth date (10 March) represents dates where social distancing was partially and voluntarily followed and last two dates (30 March and 19 April) represent strict lockdown condition during year 2020, whereas same date were selected from year 2019 also to make a comparison with previous year pattern.

The pollutant concentration for selected parameters on selected dates were taken from Loni Ghaziabad, Air quality monitoring station governed by Central Pollution Control Board, and the results summarised in Fig. 2 clearly indicates that due to lockdown of human activities including transportation and industries in Ghaziabad, the pollutant levels dropped down significantly. Concentration of these four pollutants on 14th April 2020 (last day of first lockdown) were also compared to the concentrations on 14th January 2020 (air quality, 3 months back) and 14th April 2019 to assess the percent reduction in pollutant concentration and the results are quite favourable. Table 1 shows the percentage reduction in the concentration of four major pollutants due to lockdown (indirectly due to COVID-19) which indicates that up to 85% reduction in PM2.5 concentration was observed in one of the most polluted cities of India.

Table 1
% Reduction in concentration of four major pollutants at Ghaziabad (NAQI-CPCB, 2020).

Parameter	% Reduction as compared to Jan 14, 2020 (Before 3 months)	% Reduction as compared to April 14, 2019 (Before 1 yr)
$PM_{2.5}$	85.1	46.1
PM_{10}	50.8	40.2
NO_2	48.7	34.4
SO_2	14.3	16.3

Table 2a
Analysis of variance for $PM_{2.5}$.

	Sum of Squares	df	Mean Square	F	Sig.
Between Groups	158461.664	3	52820.555	16.815	.000
Within Groups	75392.356	24	3141.348		
Total	233854.020	27			

2.1.3. Statistical analysis

In order to investigate the effect of lockdown on air quality statistically, daily average data of first week of the month was analysed for four consecutive months (January'20, February'20, March'20 and April'20), in which first three months show normal situation (no lockdown) whereas April month shows the lockdown situation. To arrive convincing conclusion on "effect of lockdown on pollutant concentration", one-way ANOVA test was performed to analyse the data, with a hypothesis that mean pollutant concentration has no effect of lockdown. The result of ANOVA for different parameters including PM2.5, PM10, SO_2, NO_2, O_3, NO, NH_3, CO, Benzene are summarised in Tables 2a–i.

ANOVA results show that only for SO_2, the p value is > 0.05, which lead to acceptance of hypothesis that lockdown has no impact on SO_2 concentration or air quality. The reason behind this may be that there are two major activities which leads to existing concentration of SO_2: first, the vehicular activities, stopping of which is not having much impact on SO_2 concentration because in NCR region already Bharat VI is implemented which does not allow much SO_2 emission from vehicular exhaust and therefore, restriction on vehicular activities does not make much impact on SO_2 concentration. Other sources of SO_2 are industrial activities which were continued during lockdown. For all other parameters the p value < 0.05, leading to rejection of null hypothesis implying that lockdown had significant impact on concentration of most of the parameters including PM2.5, PM10, NO_2, NO, O_3, NH_3, CO and Benzene.

The correlations between the above pollutant concentrations at Ghaziabad during the four weeks i.e. two before and two during lockdown are shown in Table 3. The average concentrations of PM2.5 is highly correlated with NO_2 ($r = 0.93$), NO ($r = 0.84$), NH_3 ($r = 0.91$) and Benzene ($r = 0.90$). Similarly, PM10 has also high correlations with all other pollutants except SO_2. The results imply that control of local transportation and limited industrial activities has decreased the overall pollution load on air. SO_2 has no major correlation with other pollutants which depicts no major decrease in its concentration. All other pollutants have moderate to high correlations with each other.

Table 2b
Analysis of variance for PM_{10}.

	Sum of Squares	df	Mean Square	F	Sig.
Between Groups	195302.906	3	65100.969	10.807	.000
Within Groups	144580.127	24	6024.172		
Total	339883.033	27			

Table 2c
Analysis of variance for SO_2.

	Sum of Squares	df	Mean Square	F	Sig.
Between Groups	42.722	3	14.241	.806	.503
Within Groups	423.839	24	17.660		
Total	466.560	27			

Table 2d
Analysis of variance for NO_2.

	Sum of Squares	df	Mean Square	F	Sig.
Between Groups	5903.236	3	1967.745	19.086	.000
Within Groups	2474.322	24	103.097		
Total	8377.559	27			

Table 2e
Analysis of variance for NO.

	Sum of Squares	df	Mean Square	F	Sig.
Between Groups	4476.535	3	1492.178	8.923	.000
Within Groups	4013.311	24	167.221		
Total	8489.846	27			

Table 2f
Analysis of variance for O_3.

	Sum of Squares	df	Mean Square	F	Sig.
Between Groups	3239.852	3	1079.951	8.756	.000
Within Groups	2960.165	24	123.340		
Total	6200.017	27			

Table 2g
Analysis of variance for NH_3.

	Sum of Squares	df	Mean Square	F	Sig.
Between Groups	8404.867	3	2801.622	34.042	.000
Within Groups	1975.173	24	82.299		
Total	10380.040	27			

Table 2h
Analysis of variance for CO.

	Sum of Squares	df	Mean Square	F	Sig.
Between Groups	4.590	3	1.530	9.628	.000
Within Groups	3.813	24	.159		
Total	8.403	27			

Table 2i
Analysis of variance for Benzene.

	Sum of Squares	df	Mean Square	F	Sig.
Between Groups	8.782	3	2.927	9.056	.000
Within Groups	7.758	24	.323		
Total	16.541	27			

2.2. Study of air quality improvement using satellite images

Aerosols adversely affect human health by degrading the air quality which results to premature mortality through lung cancers and cardiopulmonary diseases (Partanen et al., 2018). MODIS (Moderate Resolution Imaging Spectroradiometer) aboarded Terra and Aqua satellites (Sentinel-5P and AURA) from NASA creates satellite images of optical depth and size distribution of ambient aerosol over the globe on

Table 3
Correlation table for atmospheric pollutants at Loni, Ghaziabad District.

Pollutant ↓	→	PM 2.5	PM10	SO_2	NO_2	O_3	NO	NH_3	CO	C_6H_6
PM 2.5	Pearson coefficient	1	0.95***	0.30	0.93***	−0.56***	0.84***	0.93***	0.91***	0.90***
	P (2 tailed)		0	0.121	0	0.002	0	0	0	0
	N	28	28	28	28	28	28	28	28	28
PM 10	Pearson coefficient	0.95***	1	0.37	0.93***	−0.49***	0.78***	0.90***	0.81***	0.80***
	P (2 tailed)	0		0.05	0	0.008	0	0	0	0
	N	28	28	28	28	28	28	28	28	28
SO_2	Pearson coefficient	0.30	0.37	1	0.17	0.20	0.24	0.26	0.23	0.27
	P (2 tailed)	0.121	0.05		0.375	0.315	0.223	0.189	0.237	0.171
	N	28	28	28	28	28	28	28	28	28
NO_2	Pearson coefficient	0.93***	0.93***	0.17	1	−0.62***	0.79***	0.90***	0.84***	0.84***
	P (2 tailed)	0	0	0.375		0	0	0	0	0
	N	28	28	28	28	28	28	28	28	28
O_3	Pearson coefficient	−0.56***	−0.49***	0.20	−0.62***	1	−0.42***	−0.62***	−0.53***	−0.52***
	P (2 tailed)	0.002	0.008	0.315	0		0.027	0	0.004	0.005
	N	28	28	28	28	28	28	28	28	28
NO	Pearson coefficient	0.84***	0.78***	0.24	0.79***	0.42***	1	0.85***	0.95***	0.91***
	P (2 tailed)	0	0	0.223	0	0.027		0	0	0
	N	28	28	28	28	28	28	28	28	28
NH_3	Pearson coefficient	0.93***	0.90***	0.26	0.90***	−0.63***	0.85***	1	0.88***	0.85***
	P (2 tailed)	0	0	0.189	0	0	0		0	0
	N	28	28	28	28	28	28	28	28	28
CO	Pearson coefficient	0.91***	0.81***	0.23	0.84***	−0.53***	0.94***	0.85***	1	0.95***
	P (2 tailed)	0	0	0.237	0	0.004	0	0		0
	N	28	28	28	28	28	28	28	28	28
C_6H_6	Pearson coefficient	0.90***	0.80***	0.27	0.84***	0.52***	0.91***	0.85***	0.95***	1
	P (2 tailed)	0	0	0.171	0	0.005	0	0	0	
	N	28	28	28	28	28	28	28	28	28

The correlations are expressed as Person's correlation coefficient, where *** denote significant correlations at $p < 0.01$ (two-tailed).

hourly basis. The Aerosol Optical depth (AOD) measures how light is absorbed or reflected by airborne particles. Hazy conditions show optical depth of 1 or above and optical depth of less than 0.1 over entire atmospheric vertical column is considered 'clean'. Fig. 3 shows the AOD measurements over India during 31 March and 5 April for six years (2016–2020) (NASA, 2020). The yellow pixels and bluish pixels showing little or very low concentration of aerosol in 2020 as compared to dark brown and tan pixels, Fig. 3 clearly indicates the impact of lock down period (restricted human activities) due to Covid-19.

European Space agency also revealed that there is a significant reduction in Nitrogen dioxide (NO_2) levels (generally emitted in the atmosphere through vehicular exhausts, power plants and industries) in Indian atmosphere during of the lockdown (ESA, 2020). The Copernicus Sentinel-5P satellite showed averaged NO_2 concentrations in Indian atmosphere from January 1, 2020 to March 24, 2020 and 25 March 2020 to 20 April 2020 (the first lockdown period) compared to the same time frame last year. Fig. 4 show around 40–50% drop in the NO_2 concentrations across major cities of India (yellow-orange colour shows occurrence of NO_2 in atmosphere).

Particulate matter ($PM_{2.5}$ and $PM_{10)}$ is another indicator of air quality and it originates from various emission sources like industries, power plants, refuse burning and road dust re-suspension etc. As lockdown restricted all these activities in entire country, its direct impact on PM concentration is inevitable. To analyse the same, change in PM concentration was observed through satellite images as shown in Figs. 5 and 6; where Fig. 5 shows satellite images taken on 20th March 2020 and April 12, 2020 for PM 2.5 and Fig. 6 shows the same for PM 10.

The satellite views clearly depict how the concentration of $PM_{2.5}$ and PM_{10} has reduced during the span of one month especially in the Northern and eastern states including the capital New Delhi (The hot spot of air pollution).

2.3. Studying the impact on air quality using AQI

Effect of COVID-19 on air quality was also studied through Air Quality index (AQI) which is one of the important tools to measure the level of pollution due to major air pollutants. It is an overall scheme proposed by Central Pollution Control board (CPCB) which transforms the weighted values of seven air pollutants ($PM_{2.5}$, PM_{10}, CO, NH_3, NO_2, SO_2 and Ozone) in to a single number or set of numbers. It categorises the air quality into six categories from Good (with AQI ranging from 0 to 50) to Severe (with AQI more than 401). To analyse the effect of lockdown caused by COVID-19, AQIs before and during lockdown for 10 Indian states were compared in Table 4.

Data summarised in Table 4 demonstrate that air quality in India has been significantly improved after corona outbreak. New Delhi which was in a very bad shape before one month with frequent occurrence of smog and horribly high AQI around 300–400 shows AQI of 94 which is moderate. It is noteworthy that people from Jalandhar (Punjab) are now able to see the 'Dhauldhar mountain range' of Himachal from approximately 200 km after 30 years (CNN Travel, 2020).

3. Other indirect impacts of Covid-19 pandemic

3.1. Impact on river quality

Articles and reports in dailies and other electronic media reveal the improvement in the quality of number of rivers of India including Ganga, Cauvery, Sutlej and Yamuna etc. The primary cause is lack of industrial effluents entering the rivers due to lockdown situation under this pandemic situation. The DO levels of river Ganga as per reports has gone above 8 ppm and BOD levels down below 3 ppm at Kanpur and Varanasi (SANDRP, 2020) which ranged around 6.5 ppm and 4 ppm in 2019 respectively (Pathak and Mishra, 2020) Many other factors have also contributed in enhancing the quality of the rivers like high snowfall now melting with summer, reduction of irrigation water demand, above average rainfall and also human born factors including reduction of religious and cultural activities like puja, bathing, cremations on the banks of the rivers.

The real time water monitoring data provided by CPCB state that 27 out of 36 monitoring units placed at different places wherein the river

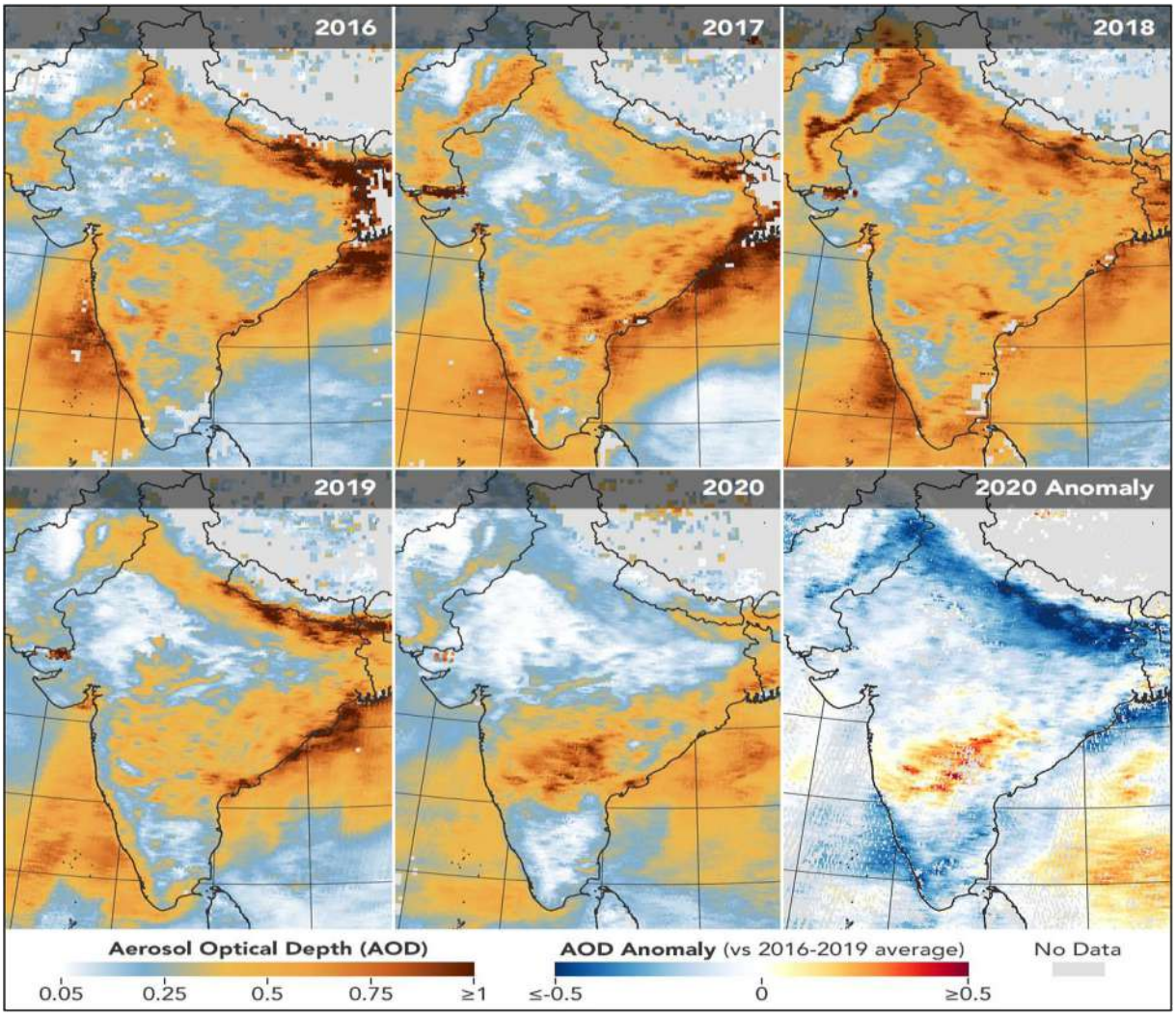

Fig. 3. AOD concentration in India from the period March 31 to April 5 in 2016–2020 (NASA, 2020).

Ganga flows were found suitable for propagation of wildlife and fisheries and bathing (The Tribune, 2020). CPCB also has three real time monitoring stations in Kanpur and Table 5 shows the water quality data as reported through these monitoring stations on 28th March 2020 i.e. during lockdown period.

It is reported that in routine days the total effluent dumped in Ganga is around 6500–6700 MLD and out of which 700 MLD (approximately 10%) come from industries. 30% of total BOD is due to industries situated along the holy river which is 130–150 tons per day. The organic load can be diluted in the river but the industrial pollution destroys the self-cleansing property of water. Researchers believe that the self-cleansing property of river Ganga has improved which has enhanced the water quality by 40–50% during this lockdown (Hindustan Times, 2020a). Scientists have claimed that water quality has remarkably improved at Haridwar Ghats which is up to drinking standards (News18 Buzz, 2020). The Ghats are also closed for people taking holy bath in the water or dumping flowers and other waste in it has stopped. This has resulted in water looking visibly cleaner with aquatic life moving around. Fig. 7 show the clean waters of Ganga at Haridwar.

River Yamuna also in most parts of Delhi is appearing clearer, blue and pristine after years. The toxic foam caused due to mix of detergents, chemicals from industries and sewage has vanished clearly in southeast Delhi's Kalindi Kunj. As per Karnataka State Pollution Control Board, the quality of water in Cauvery and tributaries like Kabini, Hemavati, Shimsha and Lakshamanathirtha is also back to what it used to be before decades (The Hindu, 2020). The pollution discharge has drastically fallen sharply in Buddha nullah which carries effluents from 2423 industrial units into Sutlej River in Punjab during this lockdown (Hindustan Times, 2020b).

3.2. Reconsider and reflect

As adversity always introduces man to himself, this situation has provided an opportunity to reflect on things and give a better understanding of who we are, what we should do and how would we do. The technologies adopted have certainly changed our mode of working and made us aware of how resilient and capable we are to handle such extreme situations. We are learning to be grateful to life and simple things they we usually ignore in routines. The importance of nature, mother earth and the natural resources have clearly been understood by humans in this pandemic situation. The world will have to face many long term and short terms effects of Covid-19. The patients who had developed Acute Respiratory Distress Syndrome (ARDS) being Corona positive, will be at greater risk of long term health issues related to major organs like heart, lungs etc. People who have recovered from this disease may have post-traumatic stress disorder (PTSD), depression and anxiety. Not only health but this pandemic situation will result in to a demand and supply-side crises which would affect entire business ecosystems and consumer behaviour. Every sector will try to develop buffers to deal with future catastrophic situations.

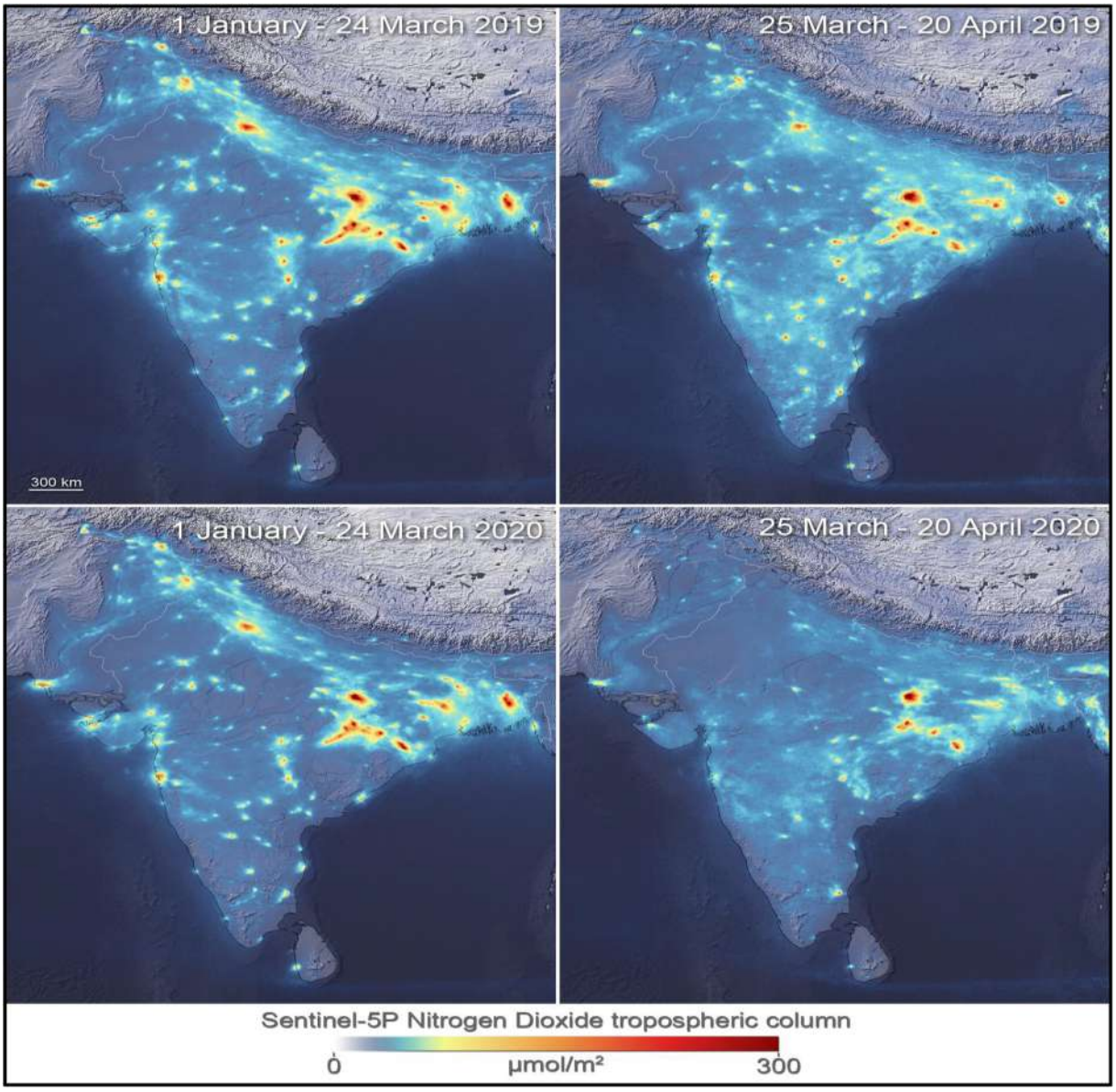

Fig. 4. Satellite images of NO_2 levels in Indian atmosphere (ESA, 2020).

It is a time for policy makers and government to plan strategies to come to normal life in post-Covid era. From previous discussion it is clear that a one-month lockdown has done such a miraculous change in environmental condition which was beyond thinking for us just couple of months back. This is also true that lockdown conditions can not be imposed forever, industries cannot be shut down for infinite time or vehicular movement cannot be restricted for much longer time but the patterns can be changed and a more responsible behaviour can be adopted. It is a known fact that anthropogenic activities are the major cause behind degraded environmental condition and disturbed ecology, but in last two months, it has become evident that still it can be restored significantly if sufficient mitigative measure and strategic government policies are planned before removing all the restrictions.

4. Conclusion

Covid-19 which originated in Wuhan somewhere three months back has now taken refuge in host bodies in 210 countries around the globe infecting 1,968,893 people and 123,783 deaths as on 14th April 2020. On same day, India has also reported to have more than 10,000 positive cases with 350 + death toll. The condition is still uncontrolled and with no proven cure for the virus. Locking down in homes and social distancing is the only preventive step that the entire country is following. But as the human activities are restricted in most of the areas, the natural environment of country has started healing itself. Factories, transport, vehicles and aviation have all ground to a halt. Carbon emissions have decreased and the quality of air has seen an unprecedented improvement. It is remarkable to see a reduction of 85.1% in $PM_{2.5}$ concentration in one of the India's most polluted city (Ghaziabad), as compared to the concentration just three months back. The other parameters lime PM_{10}, NO_2, and CO has also reduced distinctly which is the result of restricted human activities and mechanical movements. Satellite images of Indian atmosphere also reflects the same trend of reduction in air pollution after COVID-19 outbreak. The Air quality index (AQI) in all the states of India are now in two figures (indicating moderately good quality of air) after this lockdown. Not only air but the rivers of India like Ganga, Yamuna, and Cauvery etc. have become clean and clear and marine life is visible. After reviewing various reports as cited earlier, it can be summarised that undoubtedly COVID-19 has brought a fearful devastating scourge for human being

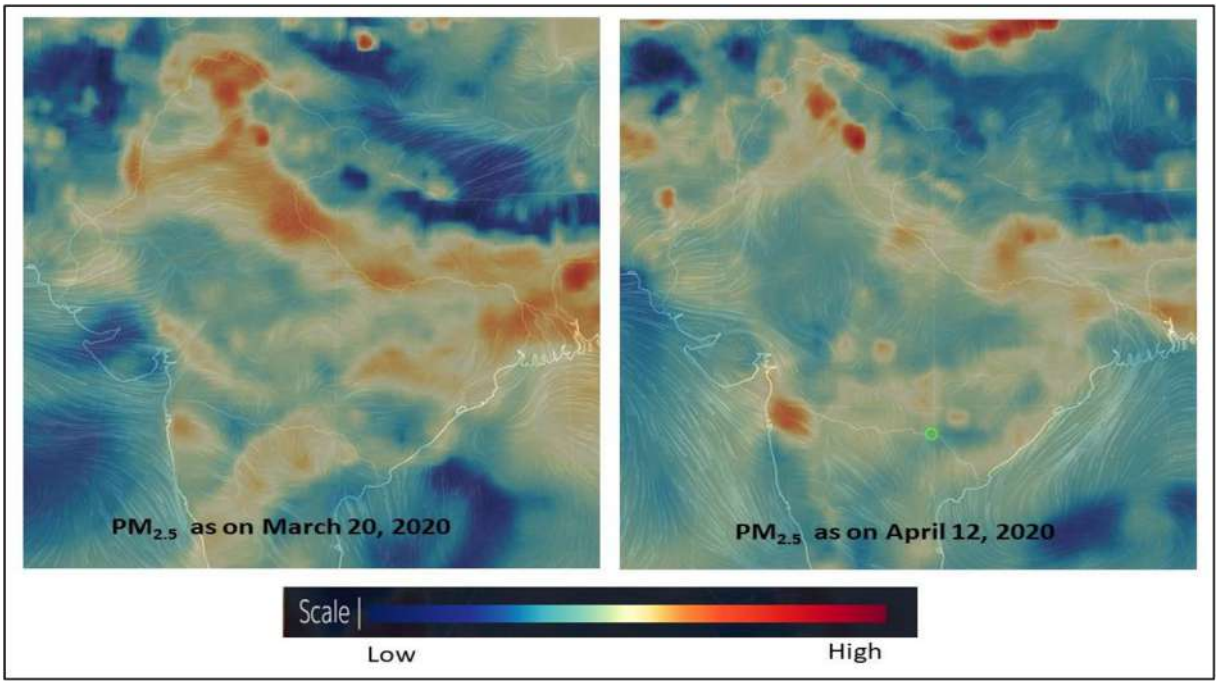

Fig. 5. Levels of $PM_{2.5}$ in Indian atmosphere (Becarrio, 2020a).

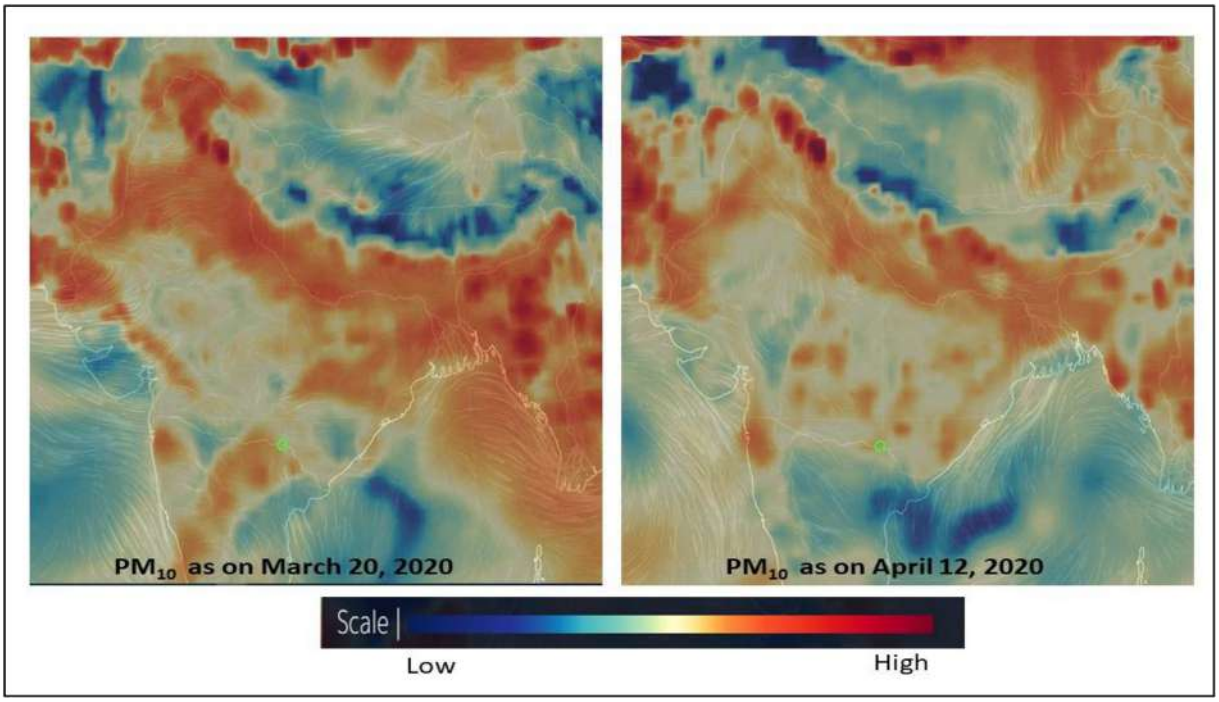

Fig. 6. Levels of PM_{10} in Indian atmosphere (Becarrio, 2020b).

but it has emerged as a blessing for natural environment providing it a "recovery time". We have also learnt that the environmental degradation caused by humans is not totally irreversible. In a period of just 1–2 months, "recovery of nature" is being witnessed by everyone. This is a signal for us to understand and react. Government and Policy makers should take necessary steps so that this healing process does not become a temporary thing. The research focusses on the changes in air quality during the lockdown period. There is a need for rigorous study on the effect of implementation of such short term lockdown as an alternative measure for pollution reduction and its effect on economy. This study may also be used as a reference document to analyse post covid condition as well to analyse effect of reduced pollution on health data of sensitive receptors. At present when entire globe is struggling to frame proper strategies to combat Covid-19, the early lockdown implemented has shown an absolute way towards restoring ecosystem and environment.

Funding sources

This research did not receive any specific grant from funding agencies in the public, commercial, or not-for-profit sectors.

Table 4
Weekly AQI data (before and during lockdown period) (NAQI- CPCB, 2020).

Sl. No	State Name	Station Name	AQI before lockdown	AQI after declaration of lockdown			
			14 January' 2020	24 March' 2020	31 March' 2020	7 April' 2020	14 April' 2020
1	Andhra Pradesh	Anand Kala Kshetram, Rajamahendravaram – APPCB	216	62	69	29	37
2	Bihar	Muzaffarpur Collectorate, Muzaffarpur - BSPCB	367	266	134	65	84
3	Chandigarh	Sector-25, Chandigarh – CPCC	75	35	38	41	45
4	Delhi	IHBAS, Dilshad Garden, Delhi - CPCB	301	99	24	37	53
5	Haryana	Sector- 16A, Faridabad – HSPCB	315	151	121	121	78
6	Karnataka	Peenya, Bengaluru – CPCB	143	105	50	57	63
7	Maharashtra	Chhatrapati Shivaji Intl. Airport (T2), Mumbai – MPCB	122	94	68	55	67
8	Punjab	Model Town, Patiala – PPCB	106	49	26	43	51
9	Tamil Nadu	Alandur Bus Depot, Chennai – CPCB	172	42	40	29	27
10	Telangana	ICRISAT Patancheru, Hyderabad - TSPCB	130	64	64	47	77

Table 5
Water quality data at monitoring stations at Kanpur as on 28th March 2020 (SANDRP, 2020).

Location of monitoring station	DO (mg/l)	BOD (mg/l)	pH	NH_3 (mg/l)	COD (mg/l)
Upstream of Ganga Barrage	8.0	2.1	7.9	0.49	< 9.0
Downstream of Ganga Barrage	7.9	1.21	7.91	1.1	< 9.0
Shuklagunj	8.51	2.1	7.68	0.79	< 9.0

Fig. 7. Clean water of River Ganga at Haridwar as on 13th April 2020 (News18 Buzz, 2020).

Credit author statement

Snehal Lokhandwala: Conceptualization, Validity, Resources, Writing (Original Draft), Writing (Review and editing), Investigation. **Pratibha Gautam**: Conceptualization, Validity, Formal Analysis, Data Curation, Writing (Original Draft), Writing (Review and editing).

Declaration of competing interest

None.

References

Becarrio, C., 2020a. Retrieved from: https://earth.nullschool.net/#current/particulates/surface/level/overlay=pm2.5/orthographic=70.81,22.26,636/loc=77.690,26.756.

Becarrio, C., 2020b. Retrieved from: https://earth.nullschool.net/#current/particulates/surface/level/overlay=pm10/orthographic=70.81,22.26,636/loc=77.690,26.756.

Cascella, M., Rajnik, M., Cuomo, A., Dulebohn, S.C., Napoli, R.D., 2020. Features, Evaluation and Treatment Corona Virus (COVID-19), NCBI Bookshelf. StatPearls Publishing.

CNN Travel, 2020. People in India Can See the Himalayas for the First Time in 'decades,' as the Lockdown Eases Air Pollution. Retrieved from: www.edition.cnn.com/travel/article/himalayas-visible-lockdown-india-scli-intl/index.html.

ESA, 2020. The European State Agency. Retrieved from: http://www.esa.int/Applications/Observing_the_Earth/Copernicus/Sentinel-5P/Air_pollution_drops_in_India_following_lockdown, Accessed date: 2 May 2020.

Gulia, S., Nagendra, S.M.S., Khare, M., Khanna, I., 2015. Urban air quality management – a review. Atmos. Pollut. Res. 6, 286–304. https://doi.org/10.5094/APR.2015.033. 2015.

Hindustan Times, 2020a. Anxiety-more-time-to-study-for-40k-students-stranded-in-Kota. Retrieved from: www.hindustantimes.com/india-news/anxiety-more-time-to-study-for-40k-students-stranded-in-kota/story-LgCluBkrFEITG9qyX16IEI.html.

Hindustan Times, 2020b. Lockdown Effect Effluent Discharge in Ludhiana's Buddha Nullah Drops. Retrieved from: www.hindustantimes.com/cities/lockdown-effect-effluent-discharge-in-ludhiana-s-buddha-nullah-drops/story-uUFPVk7yWWxBRW727eztwK.html.

India Today, 2020a. Coronavirus in India: Tracking Country's First 50 COVID-19 Cases; what Numbers Tell. Retrieved from: www.indiatoday.in/india/story/coronavirus-in-india-tracking-country-s-first-50-covid-19-cases-what-numbers-tell-1654468-2020-03-12.

India Today, 2020b. 1 lakh children under 5 years of age die from air pollution in India every year: Study. Retrieved from: www.indiatoday.in/education-today/latest-studies/story/air-pollution-india-deaths-children-five-years-report-centre-for-science-and-environment-1543779-2019-06-06.

IQAir World Air Quality Report (Region & City PM2.5 Ranking, 2019. IQAir Group. Retrieved from: www.iqair.com/world-most-polluted-cities/world-air-quality-report-2019-en.pdf.

Mahato, S., Pal, S., Ghosh, K.G., 2020. Effect of lockdown amid COVID-19 pandemic on air quality of the megacity Delhi, India. Sci. Total Environ. https://doi.org/10.1016/j.scitotenv.2020.139086.

Mandal, I., Pal, S., 2020. COVID-19 pandemic persuaded lockdown effects on environment over. Sci. Total Environ. 732, 139281. https://doi.org/10.1016/j.scitotenv.2020.139281.
MOHFW (Ministry of Health and Family Welfare) – Government of India (GOI), 2020. Retrieved from: www.mohfw.gov.in/.
NASA, 2020. NASA Earth Observatory. Retrieved from: https://earthobservatory.nasa.gov/image, Accessed date: 6 May 2020.
NAQI (National Air Quality Index) - Central Pollution Control Board (CPCB), 2020. Retrieved from: www.app.cpcbccr.com/AQI_India/, Accessed date: 15 April 2020.
News18 Buzz, 2020. Ganga River Water Has Now Become Fit for Drinking as Industries Remain Shut Due to Lockdown. Retrieved from: https://www.news18.com/news/buzz/ganga-river-water-has-now-become-fit-for-drinking-as-industries-remain-shut-due-to-lockdown-2575507.html.
Partanen, A.I., Landry, J.S., Matthews, H.D., 2018. Climate and health implications of future aerosol emission scenarios. Environ. Res. Lett. 13 (2), 024028. https://doi.org/10.1088/1748-9326/aaa511.
Pathak, S.S., Mishra, P., 2020. A review of the Ganga river water pollution along major urban centres in the state of Uttar Pradesh, India. Int. Res. J. Eng. Technol. 7 (3), 1202–1210.
Ramdan, H., Shaib, H., 2019. Middle East respiratory syndrome Corona virus (MERS-CoV): a review. Germs. PubMed-NCBI 9 (1), 35–42. https://doi.org/10.18683/germs.2019.1155. eCollection 2019 Mar.
SANDRP, 2020. Ganga-Yamuna-Cauvery Flow Cleaner in Lockdown: what Can We Learn?" DRP News Bulletin, South Asia Network on Dams, Rivers and People (SANDRP). Retrieved from: www.sandrp.in/2020/04/06/drp-nb-6-april-2020-ganga-yamuna-cauvery-flow-cleaner-in-lockdown-what-can-we-learn/#more-34730.
Shereen, M.A., Khan, S., Kazmi, A., Bashir, N., Siddique, R., 2020. COVID-19 infection: origin, transmission, and characteristics of human coronaviruses. J. Adv. Res. 24, 91–98.
Sharma, S., Zhang, M., Anshika, Gao, J., Zhang, H., Kota, S.H., 2020. Effect of restricted emissions during COVID-19 on air quality in India. Sci. Total Environ. https://doi.org/10.1016/j.scitotenv.2020.138878.
Singh, A.K., Gupta, H.K., Gupta, K., Singh, P., Gupta, V.B., Sharma, R.C., 2007. A comparative study of air pollution in Indian cities. Bull. Environ. Contam. Toxicol. 78, 411–416. https://doi.org/10.1007/s00128-007-9220-9.
The Economic Times, 2020. World's Biggest Lockdown May Have Cost Rs 7-8 Lakh Crore to Indian Economy. Retrieved from: www.economictimes.indiatimes.com/news/economy/finance/worlds-biggest-lockdown-may-have-cost-rs-7-8-lakh-crore-to-indian-conomy/articleshow/75123004.cms?from=mdr.
The Hindu, 2020. Cauvery, Tributaries Look Cleaner as Pandemic Keeps Pollution Away. Retrieved from: www.thehindu.com/news/national/karnataka/cauvery-tributaries-in-old-mysuru-region-look-cleaner-as-pandemic-keeps-pollution-away/article31210429.ece.
The Tribune, 2020. Lockdown Helps Improve Health of Ganga. Retrieved from: www.tribuneindia.com/news/nation/lockdown-helps-improve-health-of-ganga-64936.
World Economic Forum, 2020. The Deadly Link between COVID-19 and Air Pollution. Retrieved from: https://www.weforum.org/agenda/2020/04/the-deadly-link-between-covid-19-and-air-pollution.
World Health Organization, 2018. 9 Out of 10 People Worldwide Breathe Polluted Air, but More Countries Are Taking Action. Retrieved from: www.who.int/news-room/detail/02-05-2018-9-out-of-10-people-worldwide-breathe-polluted-air-but-more-countries-are-taking-action.
World Health Organization, 2020. WHO-Director-general-s-opening-remarks-at-the-media-briefing-on-covid-19. Retrieved from: www.who.int/dg/speeches/detail/who-director-general-s-opening-remarks-at-the-media-briefing-on-covid-19.
Zhong, N.S., Zheng, B.J., Li, Y.M., Poon, L.L.M., Xie, Z.H., Chan, K.H., Li, P.H., Tan, S.Y., Chang, Q., Xie, J.P., Liu, X.Q., Xu, J., Li, D.X., Yuen, K.Y., Peiris, J.S.M., Guan, Y., 2003. Epidemiology and cause of severe acute respiratory syndrome (SARS) in Guangdong, People's Republic of China. Lancet 362, 1353–1358.
Zambrano-Monserrate, M.A., Ruano, M.A., Sanchez-Alcalde, A., 2020. Indirect effects of COVID-19 on the environment. Sci. Total Environ. 728, 138813. https://doi.org/10.1016/j.scitotenv.2020.138813.

Arabian Journal for Science and Engineering
https://doi.org/10.1007/s13369-020-04652-x

RESEARCH ARTICLE-CHEMICAL ENGINEERING

A Greener Approach to Extract Copper from Fertilizer Industry Spent Catalyst

Sushmita Sharma[1] · Alok Gautam[2] · Shina Gautam[2]

Received: 10 February 2020 / Accepted: 17 May 2020

Abstract
Large quantities of catalysts after their useful life are discarded as waste material from fertilizer industry. Disposal of spent catalyst is a problem as it falls under the category of hazardous industrial waste due to its heavy metals concentration. This investigation applied a novel approach to extract copper from spent low-temperature shift catalyst ($CuO–ZnO–Al_2O_3$) using chelation process. Ethylenediaminetetraacetic acid (EDTA) was used as the chelating agent. Optimum parameters to extract 95% copper were found as: EDTA concentration 0.5 M, reaction temperature 100 °C, solid-to-liquid ratio 1:25 (g/ml), particle size 120 µm and reaction time 4 h. A kinetic analysis of the experimental data was done by shrinking core model which revealed the rate-controlling step of the leaching process as product layer diffusion. The activation energy calculated was 10.58 kJ/mol which supports leaching process to be the product layer diffusion controlled. The process adopted is eco-friendly as the EDTA was recovered after the extraction of copper from the spent catalyst and reused again. The recycled EDTA obtained after the extraction was characterized by NMR and SEM. The activity of the recycled EDTA was found to be consistent with the fresh EDTA.

Keywords Spent catalyst · Low-temperature shift catalyst · Copper extraction · Chelation · Ligand-assisted extraction

1 Introduction

In the nitrogenous fertilizer industry for ammonia production, different types of catalysts are used. All these catalysts have an active life of 5 to 7 years due to the poisoning effect of foreign materials and impurities like sulphur and coke that deposit on the surface of the catalyst and must be replaced [1]. Most of the studies on fertilizer production catalysts focus on recovery of heavy metals and trace elements from spent catalyst due to their potential risks to human health [2].

Various processes for recovery of metals from spent catalyst have been proposed. These include pyrometallurgical, hydrometallurgical and bio-hydrometallurgical methods. In hydrometallurgical extraction, different inorganic and organic acids are used such as HCl, HNO_3 and H_2SO_4, while organic acids such as citric, acetic or oxalic acids can be attractive extracting agents as the leaching is carried out at moderate acidic conditions. However, they are not suitable for less dissolving compounds due to their weak acidities, low boiling temperatures and decompositions, Prajapati et al. [3] and Smith et al. [4]. It was found that 99.95% of copper was dissolved after 14 min with inorganic acids at 0.5 M concentration, 25 °C temperature and 10 ml/g liquid-to-solid ratio, while more drastic operating conditions were needed to reach the same dissolution efficiency with citric acid solution [5].

Swaroopa et al. [6] performed physical separation of different phases of copper and followed by sulphuric acid and alkali roasting resulting in 90% Cu removal in 5 h of acid leaching. The selective leaching of Cu from Cu–Cr catalyst was carried with sulphuric acid, and 67% of Cu was found with different leaching parameters as particle size 45–53 µm, pulp density 2.5%, temperature 90 °C, time 180 min, Dowden and Kemball [7]. Limited studies were found in the literature for the copper extraction from spent catalyst. In the light of all the literature available, therefore it is extremely important to develop a process for the

✉ Shina Gautam
shina.gautam@srict.in

[1] Department of Chemical Engineering, Jaypee University of Engineering and Technology, Guna, Madhya Pradesh 473226, India

[2] Department of Chemical Engineering, Shroff S R Rotary Institute of Chemical Technology, Vataria, Gujarat 393135, India

Published online: 03 June 2020

recovery of copper from spent catalyst. Kinetics of different metals with EDTA and citrate were observed in soil, and comparison of both has been discussed [8].

In the present study, a well-acknowledged chelating agent ethylenediaminetetraacetic acid (EDTA) was used for extracting copper from the low-temperature shift (LTS) catalyst. A few studies have been found where EDTA was used to leach out different metals from the spent catalyst. Goel et al. [9] have used EDTA for the Ni removal from the primary reforming catalyst of fertilizer industry, and 96% nickel was recovered in the form of nickel sulphate with fresh EDTA concentration 0.8 M, reaction time 10 h, temperature 100 °C. Chauhan et al. [10] selectively separated more than 90% Co and Mo with EDTA at conditions: 6 h digestion time, 0.4 M EDTA concentration, 1:25 solid-to-liquid ratio and different pH were maintained to separate the Co and Mo. EDTA was also recovered after leaching. Interactions of parameters were also observed for different parameters for the process of copper extraction by design of experiments, Sharma et al. [11].

The reaction of copper present on the catalyst surface with EDTA follows as Eqs. (1) and (2) in Fig. 1. The Cu in the form of sulphate is left at the end of the process. In this figure first reaction is the chelation of the EDTA with copper oxide where EDTA makes a complex with copper oxide. In the second step or the second reaction, this complex of copper and EDTA was broken and copper is released from EDTA. This EDTA is called recovered EDTA.

2 Materials and Methods

2.1 Catalyst Preparation

The spent catalyst used in this investigation was low-temperature shift catalyst obtained from National Fertilizer Limited, Vijaipur, Madhya Pradesh, India. The catalyst was grounded in a ball mill and sieved up to 120 µm sieve size. The catalyst was washed thoroughly with demineralized water at room temperature and filtered with Whatman filter paper no 42. Later on, it was kept in a porcelain disc and calcined in a muffle furnace for 4 h at 500 °C for coke removal. After calcination, the materials were cooled down to room temperature. The weight loss due to coke deposition and other water dissolved impurities were found to be 18%. The calcined catalysts were kept in desiccators for further use in the experiments.

2.2 Experimental Procedure

The composition of the catalyst was provided to be CuO: 35–37%, ZnO 35–37%, Al_2O_3 15–33%. It was verified by a 5 g sample which was calcined at 500 °C in a muffle furnace followed by digestion for 6 h in 100 ml 98% (v/v) sulphuric acid at 100 °C with stirring. No residue was left after the filtration. The sample was analysed by ICP-OES and confirmed the composition provided.

After assuring the initial chemical composition, a series of experiments were conducted in triplicate manner. The digestion of the spent catalyst was performed batch-wise in a conical

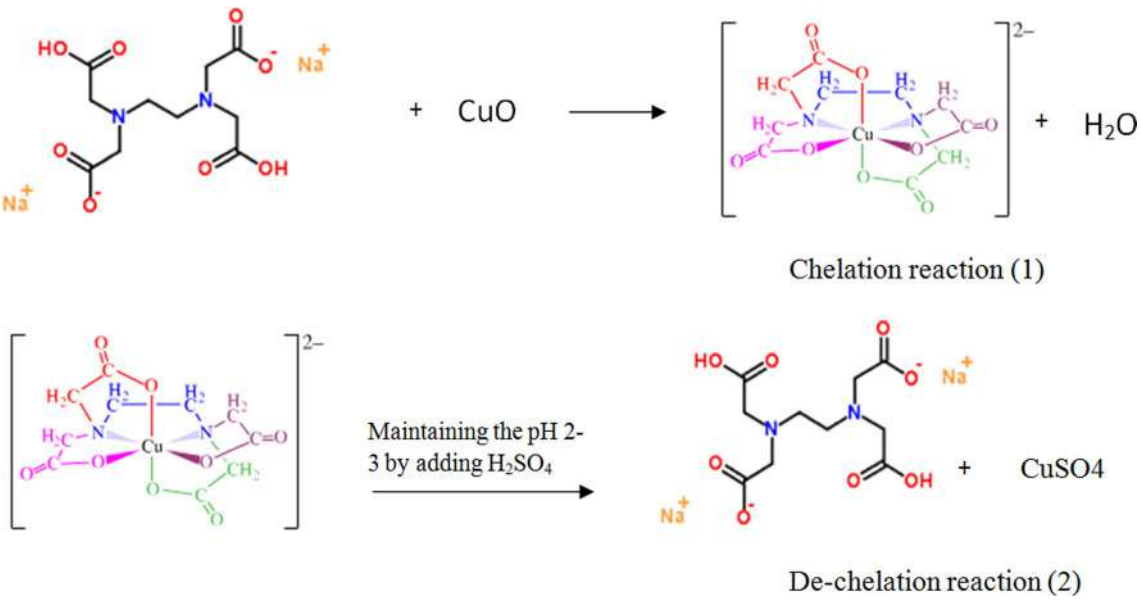

Fig. 1 Reaction of Cu with EDTA and formation of $CuSO_4$

flask of 250 ml equipped with a condenser placed on heating mantle with a magnetic stirrer. Two grams of spent catalyst was added in each experiment for the specified concentration of EDTA prepared in a conical flask. pH of the solution was maintained 8 by adding 25% ammonia solution. After digestion of catalyst for a specified condition, the solution was filtered. Sulphuric acid was added drop-wise in a cold bath to the filtrate to dechelate the EDTA with the copper. The EDTA was precipitated, and the solution was filtered again to estimate the copper recovery. The proposed methodology is given in Fig. 2. The copper present in the filtrate was analysed in UV spectrophotometer (ELICO SL 159). To calibrate the UV spectrophotometer, known concentration of copper sulphate solution in the range of 100–1000 ppm was prepared. The calibration was done with respect to the blank solution. The absorbance of the Cu was obtained at 348 nm wavelength. The calibration curve was prepared by plotting between amount of copper and absorbance. Equation of calibration was obtained as:

$$Y = 12.63x \tag{3}$$

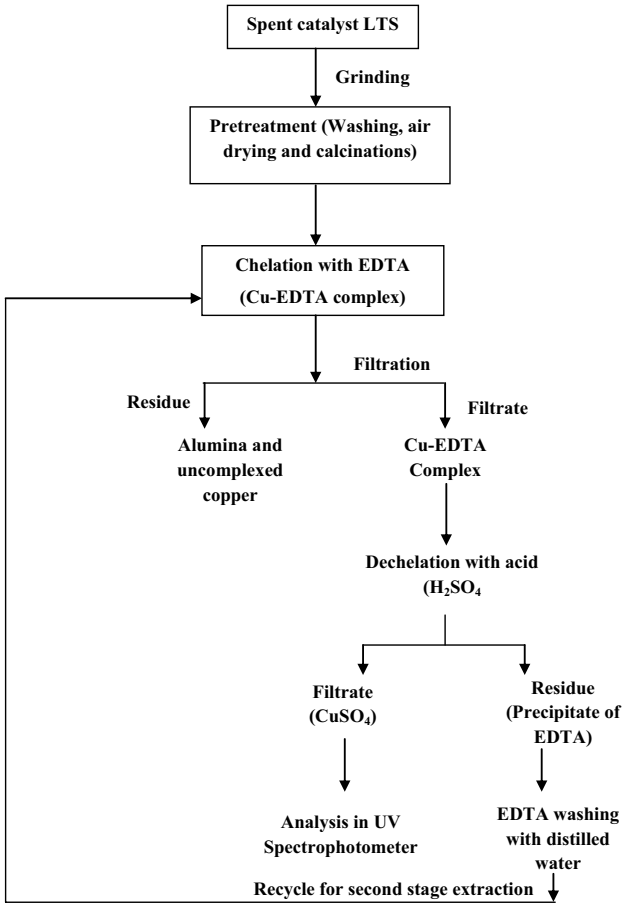

Fig. 2 Proposed methodology for extraction of copper from spent low-temperature shift catalyst

where Y is the absorbance and x is the amount of copper in ppm. After attaining the calibration curve, unknown concentration of copper in different test solutions was analysed with respect to the blank solution and Eq. (3) was used to calculate the concentration with the observed absorbance. The calculation of the copper % extracted in all experiments was done according to Eq. (4)

$$\%\ \text{Extraction of copper} = \frac{\text{Amount of copper in solution (g)}}{\text{Total mass of copper present in catalyst (g)}} \times 100. \tag{4}$$

All the chemical compounds and reagents used were of analytic grade (Merck). H_2SO_4 was of 98% purity, ethylenediaminetetraacetic acid EDTA (disodium salt) 99% and ammonia solution (25%) were 99% and 91% pure, respectively.

3 Results and Discussion

3.1 Effect of Concentration of EDTA

The EDTA concentration dependency for leaching copper is shown in Fig. 3. Concentration of fresh and recovered EDTA was varied from 0.1 M to 0.8 M. Copper leaching experiments were performed under atmospheric reflux conditions at 100 °C for 4 h. The solid-to-liquid ratio of 1:50 (w/v) and particle size of 120 µm were kept constant while varying the concentration of EDTA. Continuous stirring at 600 rpm was provided. It can be explained from Fig. 3 that as the concentration of either EDTA increases the copper recovery increases; however, after 0.5 M concentration, the extraction of the copper was 90% with fresh EDTA. Increasing further the concentration did not affect the extraction

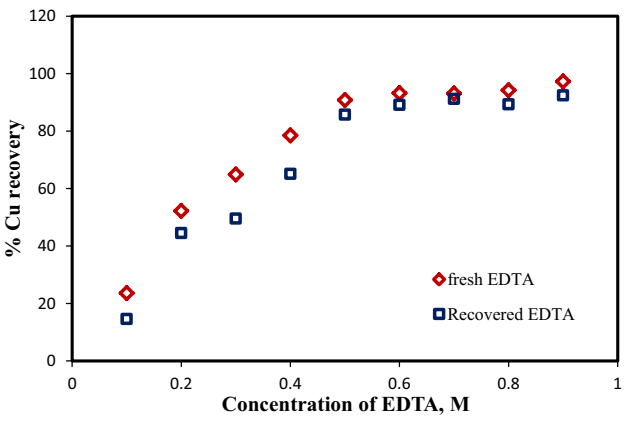

Fig. 3 Effect of concentration of fresh and recovered EDTA on recovery of copper

of copper. One point is to be noted that recovered EDTA which was obtained after fresh EDTA experiments showed slightly less recovery of copper than fresh EDTA. 2–3% less recovery was observed for recovered EDTA than fresh EDTA in all the experiments. Deveci et al. [12] observed less than 2% Cu extraction using H_2SO_4 in the absence of any oxidant, while more than 60% Cu was recovered using H_2O_2 along with H_2SO_4. It was suggested that oxidative leaching is an efficient way to recover base metals, Tuncuk et al. [13]. However, in the present study, no oxidizing agent during copper leaching was used and the recovery was close to 90%. This is the advantage of chelating agent; it can also be recovered and showed considerable amount of recovery. A concentration of 0.5 M fresh EDTA was considered as an optimum concentration for further experiments.

3.2 Effect of Reaction Time

After optimized concentration of EDTA at 0.5 M, the time of reaction was varied from 30 min to 7 h with continuous heating and stirring at 100 °C and 600 rpm in Fig. 4. Other parameters were kept constant as solid-to-liquid ratio 1:50 (w/v) and particle size 120 µm. It was observed that the time had a significant effect on the dissolution of copper, as the time of reaction increasd, the copper makes coordination bond with the EDTA. After 4 h of leaching time, up to 95% of Cu was extracted. A further increase in time could not result so much effect on extraction of copper. Thus, an optimum time of 4 h was chosen. The results are in agreement with the literature where reaction time for the extraction experiment was considered 1–5 h for Zn extraction, Mohapatra et al. [14]. Lee et al. 2013 did the leaching experiment from spent HDS catalyst to recover Co and Mo and used the leaching time from 1 to 5 h at room temperature and considered 1 h as the equilibrium time to leach the metal. The current experiments had found less time for up to 95% of copper recovery in 4 h for fresh EDTA. Similar experiment was performed with recovered EDTA; it was found that extraction of copper was achieved up to 84% in 4 h. The extraction was not observed increasing after 4 h. A comparison of performance of extraction capacity was observed with fresh and recovered EDTA.

3.3 Effect of Solid-to-Liquid Ratio at Varying Concentration

The effect of solid-to-liquid ratio on the dissolution rate of copper was studied as shown in Fig. 5. A wide range of solid-to-liquid ratio was varied from 1:10 to 1:50 by keeping other variables constant. It was observed that the extraction efficiency of copper was greatly increased with increasing solid-to-liquid ratio. The excess amount of EDTA present in solution enhanced the recovery of copper from the spent catalyst. When the solid-to-liquid ratio was increased from 1:10 to 1:50 by keeping other parameters constant as concentration of EDTA 0.5 M, leaching time 4 h, temperature 100 °C and particle size of 120 µm, the recovery of copper was increased with fresh and recovered EDTA. Kim et al. [15] also studied the effect of solid-to-liquid ratio to extract the metal from soil and concluded that there is not much effect after reaching a certain ratio. Beyond a certain amount of extractant in excess does not lead higher extraction. The results indicated that maximum extraction of copper was found 90% at 1:50 solid-to-liquid ratio with fresh EDTA and 85% with recovered EDTA. However, at solid-to-liquid ratio of 1:25, the extraction of the copper with fresh EDTA is 80% and with recovered EDTA was 71% (Fig. 6). The increase in volume of EDTA solution by double did not significantly increase the extraction of copper; therefore, 1:25 solid-to-liquid ratio can be considered as an optimum parameter. By increasing solid-to-liquid ratio to 1:50 from 1:25, amount of EDTA required will be double by weight which will increase the raw material cost when we go for scale-up.

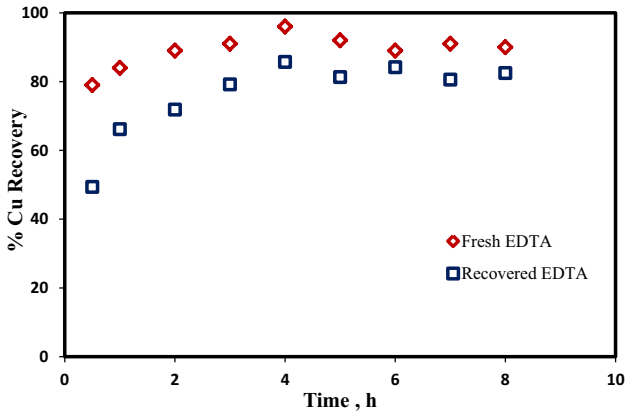

Fig. 4 Effect on recovery of copper with increasing time

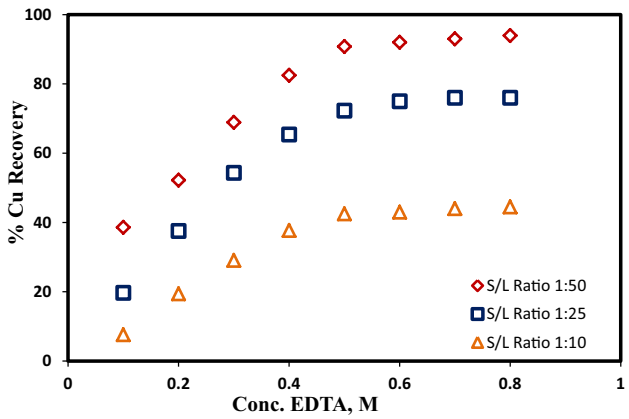

Fig. 5 Effect of solid-to-liquid ratio with varying concentration of EDTA on recovery of copper

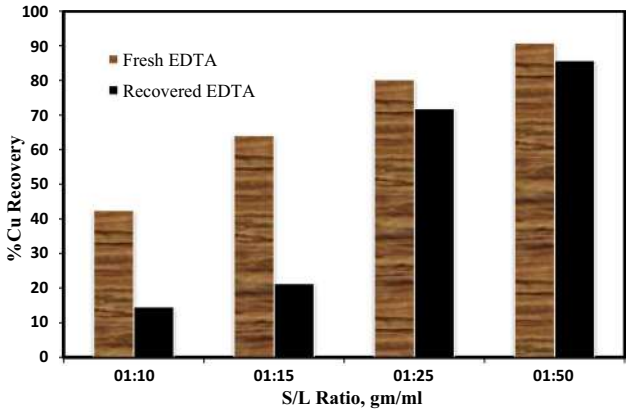

Fig. 6 Effect of solid-to-liquid ratio using fresh and recovered EDTA on recovery of copper

3.4 Effect of Temperature on the Copper Leaching

Temperature plays a significant parameter in leaching due to increase in solubility of solute in solvent. Figure 7 shows the change in copper extraction using fresh EDTA with the temperature in the range of 60 °C to 100 °C. The copper extraction was relatively slow in the experiments carried out at 60 °C (84%) but significantly increased as the leaching temperature raised and a high copper extraction was observed at 100 °C (94%). This increase in extraction can be explained by an increase in reaction rate constant with the development of reaction temperature. The leaching of copper at 100 °C could provide better recovery of copper. Experiments were conducted at atmospheric reflux conditions so this was a maximum temperature that could be attained. The similar trend of the temperature behaviour in leaching experiments of Co and Mo from spent HDS catalyst by HCl was obtained by Banda et al. [16]. Extraction of Zn was carried out in alkaline media with EDTA at very low concentrations and the recovery of Zn was reported up to 93%. The temperature of the reaction was varied between 30 and 90 °C, Mohapatra et al. [14]. Mazurek [17] studied the effect of temperature from spent vanadium catalyst in alkaline media, the leaching of metals including iron and vanadium decreased after 50 °C due to alkaline media. Effect of temperature on leaching was observed in the range of 15–60 °C.

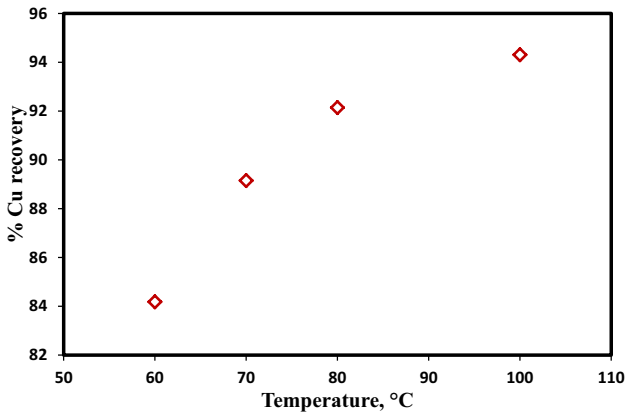

Fig. 7 Effect of temperature using fresh EDTA on recovery of copper

3.5 Effect of Particle Size on Leaching of Copper

Figure 8 shows the effect of particle size on the copper recovery while keeping other parameters constant as EDTA concentration 0.5 M, time of reaction 5 h, solid-to-liquid ratio 1:25, temperature 100 °C. Smaller particle size has more surface area and surface to react with the solvent. However, in the experiments, particle size effect was not observed significant. As the particle size was varied from 180 to 90 µm, it can be observed from the figure that after decreasing the particle size from 120 to 90 µm, the recovery was increased to 2%. The overall increase in copper from 180 µm particle size to 90 µm particle size was only 10–12%. Parhi et al. [18] carried out copper leaching from Cr–Cu spent catalyst with sulphuric acid. The particle size used was less than 150 µm. They reduced the particle size to 50 µm; however, the recovery of the Cu was not increased beyond this particle size. Reducing particle size up to nanometre will increase grinding cost; however, it could be saved as it is not affecting much in the present studies.

4 Kinetic Study

4.1 The Shrinking Core Model (SCM)

The SCM was first developed by Yagi and Kunii [19]. In the establishment of the SCM, the solid reactant is considered to be non-porous and is initially surrounded by a fluid film

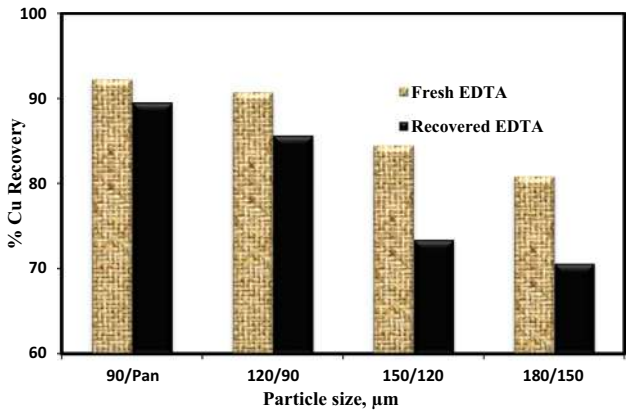

Fig. 8 Effect of particle size of catalyst using fresh and recovered EDTA on recovery of copper

through which mass transfer occurs between the solid particle and the bulk of the fluid. The reaction rate is generally controlled either by diffusion through the liquid film, diffusion through the ash/product layer and the chemical reaction at the surface of the solid particles or a combination of diffusion and chemical reactions. There are few assumptions considered in the model namely Levenspiel [20]:

(1) The particle is spherical.
(2) Solvent reaction forms a porous outer layer and an unreacted core.
(3) The dissolving part is a crystalline phase.
(4) The unreacted core shrinks and the dissolved part diffuses through the porous shell towards the solvent.

The reaction model between a liquid and a solid may be given as:

$$\text{EDTA solution} + \text{Spent catalyst} \rightarrow \text{EDTA-Cu} + \text{Catalyst support}. \quad (5)$$

In the fluid–solid systems, the reaction rate may be generally controlled by one of the following steps, Feng et al. [21]:

(1) Diffusion through the liquid film surrounding the solid particle.
(2) Chemical reaction at the surface of the unreacted core.
(3) Diffusion through the porous product layer.

Chelation experiments were performed at constant stirring speed. The stirring speed was kept enough to make the solution homogeneous, and no solid was settled or channelled at the flask surface. Another reason to keep the stirring speed constant was to disregard the diffusion control through the external mass transport. Therefore, extraction process is expected to be controlled either by surface reaction or diffusion through the product layer. When surface chemical reaction controls,

$$k_r t = 1 - (1 - X)^{1/3} \quad (6)$$

where $k_r = b.k.C_{Ab}/\rho.R$, where k_r is the apparent rate constant for reaction controlled process (h^{-1}), t is the reaction time (h), b is the stoichiometric coefficient of copper in leaching reaction (dimensionless), k is the chemical reaction rate constant (m/h), ρ is the molar density of solid reactant (kg/m^3), X is the reacted fraction of copper, C_{Ab} is the concentration of EDTA in the bulk solution, and R is the radius of spent catalyst particles.

When the fluid–solid system is controlled by diffusion through porous product layer, the expression is given as

$$k_d.t = 1 - \frac{2}{3}X - (1 - X)^{2/3} \quad (7)$$

where $k_d = 6.b.De.C_{Ab}/\rho.R^2$, where De is the effective diffusion coefficient.

The results of copper extraction concentration for varying time at different solid-to-liquid ratios were plotted for the reaction model [Eqs. (6) and (7)]. In Fig. 9, Eq. (6) was plotted as $1-(1-x)^{1/3}$ versus time t. If experimental data follow equation, it must have no intercept means it should pass through origin and it should follow a straight line. However, the line is having an intercept as well as correlation coefficient of straight line is below 0.9. The correlation coefficient represents the data to which extent, it is the closest to the line of best fit. Therefore, the data cannot be correlated with model [Eq. (6)]. It can be concluded that chemical reaction is not a controlling step of the reaction.

To evaluate the dominance of the other resistance which is applicable in fluid–solid systems, i.e. the product layer diffusion. The same kinetic data of different solid-to-liquid ratios was plotted for model [Eq. (7)]. Figure 10 shows the plot between $1-\frac{2}{3}X-(1-X)^{2/3}$ and t. The results reveal that the correlation coefficients (R^2) are closer to 1 than those in Fig. 9, and intercepts are close to zero which confirms the well-fitted diffusion-controlled extraction process. It can be suggested that extraction of copper is controlled by product layer diffusion.

In spite of the surface degradation generated by the leaching process, it was suggested that the particle surface does not present a reaction product layer. In other words, a diffusion-controlled mechanism will be dominant, Levenspiel [20] and Wadsworth and Miller [22]. In present experiments, the support material acts as a product layer and supposed to be stable and invariable in particle size. So copper is selectively leached, while the alumina remains as a product layer. In another study, the product layer diffusion was observed as a controlling reaction for

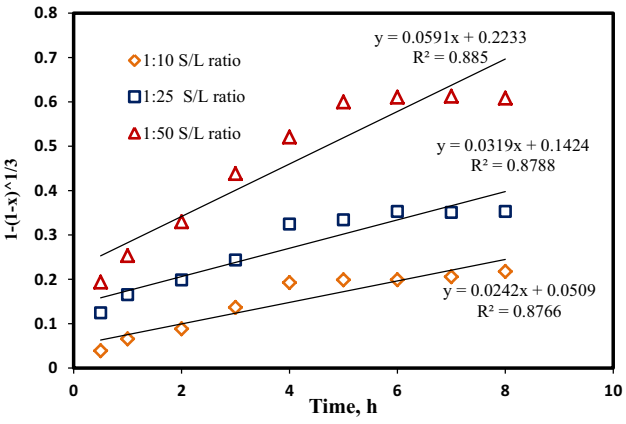

Fig. 9 $1-(1-x)^{1/3}$ versus time (h) for extraction of copper with EDTA when chemical reaction is the rate-controlling step

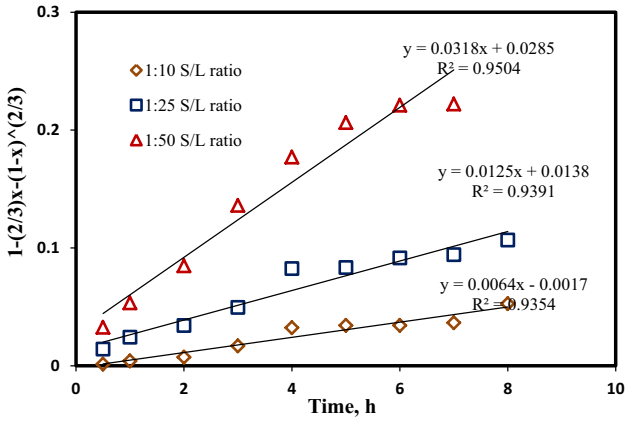

Fig. 10 $1-(2/3)x-(1-x)^{2/3}$ versus time (h) for extraction of copper with fresh EDTA when diffusion through the solid product layer is controlling step

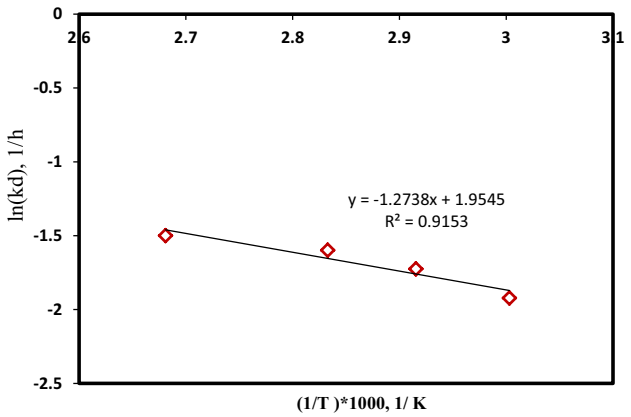

Fig. 11 Calculation of activation energy by Arrhenius plot for leaching of copper

pressure leaching experiments carried out with limonitic laterite ores, Georgiou and Papangelakis [23].

4.2 Calculation of Activation Energy

Arrhenius equation was applied to calculate the activation energy for a diffusion-controlled extraction process. In order to calculate the activation energy, the plot of $\ln(k_d)$ against $1/T$ should be a straight line with a slope of $-E/R$ and an intercept of $\ln k$, according to Arrhenius equation as shown

$$\ln K_d = \ln k - \left(\frac{E}{RT}\right). \tag{8}$$

The activation energy of the overall reaction is calculated as 10.58 kJ/mol from Fig. 11. The activation energy of a diffusion-controlled process is characterized as from different studies as 4–13 kJ/mol, Anand et al. [24], 8–21 kJ/mol, Lozano and Juan [25] and 13–25 kJ/mol, Mulak and Miazga [26]. However, for chemical reaction controlled process, it is usually greater than 40 kJ/mol, Abdel [27]. For a mixed control process, it is in a range of 13–43 kJ/mol, Feng et al. [27]. The magnitude of this activation energy clearly confirms that the leaching of copper is most likely controlled by diffusion of ions through the product layer. Furthermore, this activation energy is in consistent with 15.7 kJ/mol calculated for nickel leaching from spent catalyst in sulphuric acid solution, Feng et al. [28], 13.4 kJ/mol calculated for sulphuric acid leaching of low-grade zinc silicate ore, Abdel [27] and 18.4 kJ/mol calculated for vanadium leaching from spent sulphuric acid catalysts by sulphuric acid solution, Mulak and Miazga [26].

5 Possibility of Recycling the Solvent (EDTA)

The present study is advantageous in terms of solvent recovery. In the current investigation, 98% EDTA could be recovered and the recovered EDTA was reused in the copper extraction experiments to investigate the possibility of EDTA. The recovery of the EDTA was investigated up to 2 cycles and the efficiency of the recycled EDTA was reduced by 2–3% in each cycle. However, significant metal extraction capability was observed with the recovered EDTA. EDTA was recovered in the leaching process by dechelation reaction of 8–10 h. Further cold conditions were given to let precipitate the EDTA and 1–1.5% EDTA was recovered after 2 days of precipitation of leached solution. The reason of the slightly decreased efficiency can be explained as the interference of cations which precipitate during dechelation process with EDTA, Chauhan et al. [29]. However, moisture was removed completely and the samples were kept in desiccators until further use. Figures 3, 4, 6 and 8 show the recovered EDTA extraction. It can be said that EDTA process is a more eco-friendly solvent due to recoverability than the acid leaching process and other non-recoverable process having higher extraction ability.

To confirm the integrity of the structure of EDTA, proton nuclear magnetic resonance (NMR) of recycled EDTA was done. It revealed two types of hydrogen as shown in Fig. 12. The solvent used for the proton NMR was D_2O. Hydrogen impurities were present in this sample as shown by a peak in Fig. 12a, b in the spectrum (peak C). There are three types of hydrogen in the EDTA structure. Due to the reaction with deuterium, the acidic hydrogen was replaced by the deuterium and the other two hydrogen atoms ethylene in acetic acid and ethylene with amine are labelled A and B, respectively. The structure of the EDTA is symmetric if divided down the middle. It should show a total of three peaks in the spectrum. The hydrogen atoms present at ethylene of acetic acid are twice of ethylene with amine. Peak B shows the hydrogen of ethylene of acetic

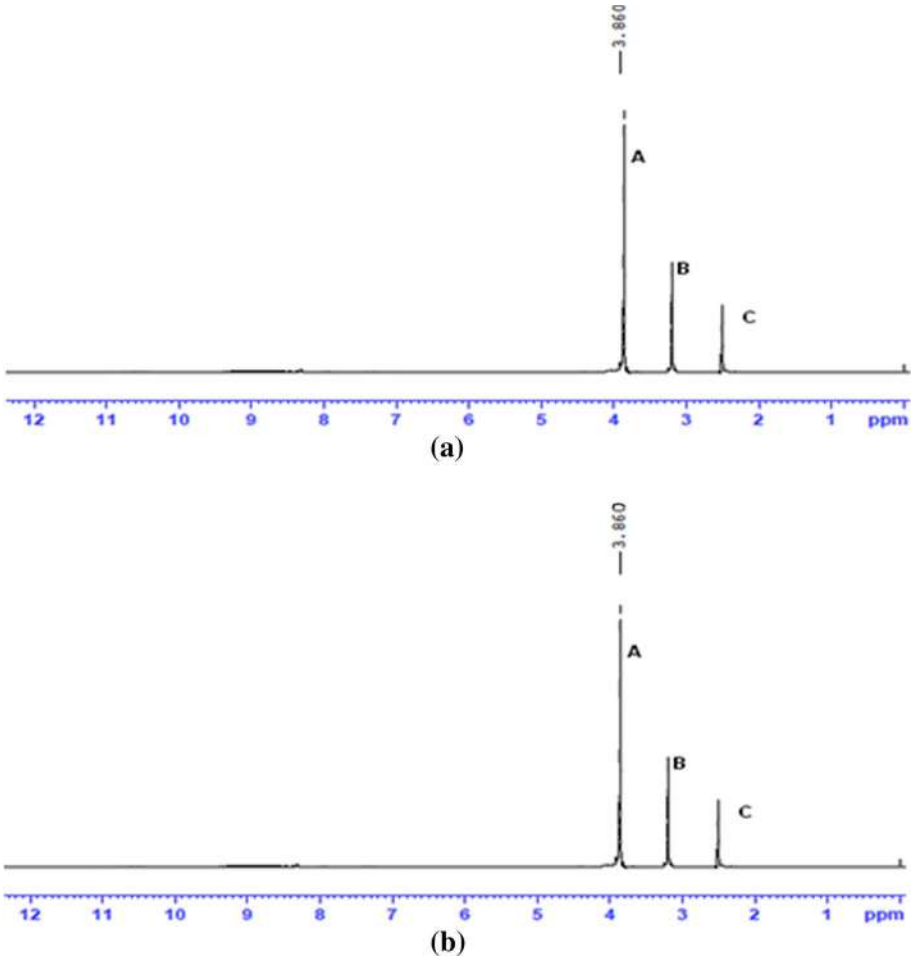

Fig. 12 Proton NMR spectrum of **a** first time recovered EDTA, **b** second time recovered EDTA

acid, and peak A shows the hydrogen of ethylene with amine groups. The area of peaks B and A is in the ratio of 1:2 due to the number of hydrogen atoms in the EDTA structure. The fresh and recycled EDTA shows the same behaviour and did not change during repetitive usage, Goel et al. [9].

Scanning electron microscopy of the recycled EDTA was done to magnify the molecules of the EDTA. It was done at two different magnifications to investigate the morphology. Figure 13a, c is taken at 500 times magnification, and Fig. 13b, d is taken at magnification 3000 times. Figure 13a, b is for first time recycled EDTA, and Fig. 13c, d is for second time recycled EDTA. It can be deduced from Fig. 13 that first time recycled EDTA has more number of small particles; however, the morphology of the particle is changed for the second time recycled EDTA and particles seem more agglomerated than the previous recycle. The pallet diameter for the first time recycled EDTA is 3.93 µm, while second time recovered EDTA has pallet diameter of 11.33 µm. That may be the reason of less leaching efficiency of EDTA in successive cycles. As the particle size increases for the recycled EDTA, the diffusion coefficient of EDTA to spent catalyst may be reduced. The morphology may change further as the cycles of EDTA would be increased.

6 Conclusions

The present investigation demonstrates the possibility of Cu removal from low-temperature shift spent catalyst with EDTA and its recoverability to use it again. Optimum conditions for the Cu leaching with fresh EDTA were obtained by the experiments as 0.5 M concentration of EDTA, 4 h of reaction time, reaction temperature 100 °C, particle size 120 µm and 1:25 solid-to-liquid ratio. The recovered EDTA was used again, and concentration of EDTA, time of digestion, solid-to-liquid ratio and particle size were investigated. At optimum conditions with fresh EDTA, 95% Cu was obtained; however, 91% Cu was obtained with recycled EDTA. In first recycle, 98% EDTA was recovered, and in second cycle, similar yield of the EDTA was observed. A kinetic analysis of the experimental data with shrinking core model revealed that the extraction of Cu from spent catalyst is controlled by the product layer diffusion which is nothing

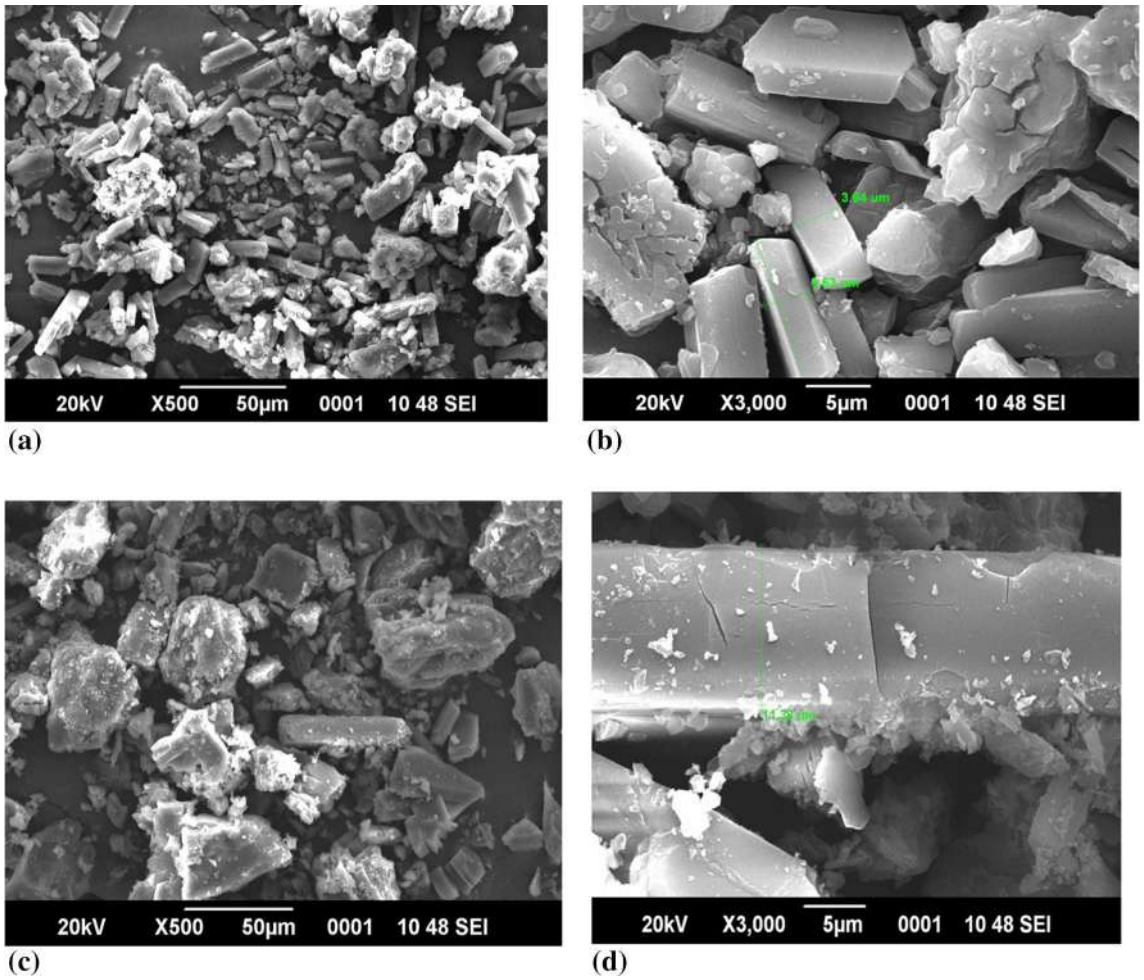

Fig. 13 **a** and **b** SEM images of first time recovered EDTA, **c** and **d** SEM images of second time recovered EDTA

but the porous structure of the catalyst. It is also confirmed by the activation energy. In the later part of the study, characterization of the recycled EDTA was done to investigate the morphology by SEM and bonding of hydrogen in the structure. The SEM analysis realized that the particles get agglomerated and particle size increases 3 to 4 times in successive recycles. However, bonding among the hydrogen and quantity within EDTA structure remain same as confirmed by NMR.

Acknowledgements Authors are very grateful to National Fertilizer Limited, Vijaipur, Madhya Pradesh, for providing the spent catalyst. Authors also acknowledge Sophisticated Analytical Instrument Facility Kochi, India, to provide assistance in characterization of EDTA.

References

1. Jadhav, U.U.; Hocheng, H.: A review of recovery of metals from industrial waste. J. Achiev. Mater. Manuf. Eng. **54**, 159–167 (2012)
2. Oza, R.; Patel, S.: Recovery of nickel from spent Ni/Al_2O_3 catalysts using acid leaching, chelation and ultrasonication. Res. J. Rec. Sci. **1**, 434–443 (2012)
3. Prajapati, R.P.; Sharma, A.; Tiwari, D.R.: Utilization of spent catalyst (solid waste) from the nitrogeneous chemical plant. Orient. J. Chem. **27**(3), 1289–1292 (2011)
4. Smith, B.; Muruganandam, R.J.; Murthy, L.; Shantha, S.: A review of the water gas shift reaction kinetics. Int. J. Chem. React. Eng. **8**, 1–34 (2010)
5. Singh, B.: Treatment of spent catalyst from the nitrogenous fertilizer industry—a review of the available methods of regeneration, recovery and disposal. J. Hazard. Mater. **167**(1–3), 24–37 (2009)
6. Swaroopa, S.; Ghosh, M.K.; Sanjay, K.; Mishra, B.K.: Extraction of Cu and Cr from a spent Cu–Cr catalyst: recovery enhancement through mechanical activation. Hydrometallurgy **136**, 8–14 (2013)
7. Dowden, D.A.; Kemball, C.: Catalysis, vol. 2, p. 1. Specialist Periodical Report of the Chemical Society, London (1978)
8. Labanowski, J.; Monna, F.; Bermond, A.; Cambier, P.; Fernandez, C.; Lamy, I.; Van Oort, F.: Kinetic extractions to assess mobilization of Zn, Pb, Cu, and Cd in a metal-contaminated soil: EDTA vs. citrate. Environ. Pollut. **152**(3), 693–701 (2008)
9. Goel, S.; Pant, K.K.; Nigam, K.D.P.: Extraction of nickel from spent catalyst using fresh and recovered EDTA. J. Hazard. Mater. **171**, 253–261 (2009)

10. Chauhan, G.; Pant, K.K.; Nigam, K.D.: Metal recovery from hydroprocessing spent catalyst: a green chemical engineering approach. Ind. Eng. Chem. Res. **52**(47), 16724–16736 (2013)
11. Sharma, S.; Dutta, N.N.; Agrawal, G.K.: Optimization of copper extraction from spent LTS catalyst ($CuO–ZnO–Al_2O_3$) using chelating agent: Box–Behnken experimental design methodology. Russ. J. Non-Ferrous Met. **58**(1), 22–29 (2017)
12. Deveci, H.; Yazici, E.Y.; Aydin, U.; Yazici, R.; Akcil, A.: Extraction of copper from scrap TV boards by sulphuric acid leaching under oxidising conditions. In: Proceedings of Going Green-Care Innovation Conference, 8–11 Nov. Vienna, Austria (2010)
13. Tuncuk, A.; Stazi, V.; Akcil, A.; Yazici, E.; Deveci, H.: Aqueous metal recovery techniques from e-scrap: hydrometallurgy in recycling. Min. Eng. **25**, 28–37 (2012)
14. Mohapatra, M.; Nayak, B.; Sanjay, K.; Subbaiah, T.; Mishra, B.K.: Ligand mediated eco-friendly leaching of zinc from spent catalyst in alkaline media. J. Ind. Eng. Chem. **20**(4), 2217–2223 (2013)
15. Kim, C.; Lee, Y.; Ong, S.K.: Factors affecting EDTA extraction of lead from lead contaminated soils. Chemosphere **51**, 845–853 (2003)
16. Banda, R.; Nguyen, T.H.; Sohn, S.H.; Lee, M.S.: Recovery of valuable metals and regeneration of acid from the leaching solution of spent HDS catalysts by solvent extraction. Hydrometallurgy **133**, 161–167 (2013)
17. Mazurek, K.: Recovery of vanadium, potassium and iron from a spent vanadium catalyst by oxalic acid solution leaching, precipitation and ion exchange processes. Hydrometallurgy **134–135**, 26–31 (2013)
18. Parhi, P.K.; Sethy, T.R.; Sarangi, P.C.K.: Selective dissolution of copper from copper-chromium spent catalyst by baking–leaching process. J. Ind. Eng. Chem. **21**, 604–609 (2015)
19. Yagi, S.; Kunii, D.: Studies on combustion of carbon particles in flames and fluidized beds. In: Fifth Symposium (International) on Combustion, Reinhold, New York, pp. 231–244 (1955)
20. Levenspiel, O.: Chemical Reaction Engineering, 2nd edn, pp. 364–365. Wiley, New York (1972)
21. Feng, X.; Long, Z.; Cui, D.; Wang, L.; Huang, X.; Zhang, G.: Kinetics of rare earth leaching from roasted ore of bastnaesite with sulfuric acid. Trans. Nonferrous Met. Soc. China **23**(3), 849–854 (2013)
22. Wadsworth, M.E.; Miller, J.D.: Hydrometallurgical processes. In: Sohn, H.Y., Wadsworth, M.E. (eds.) Rate Processes of Extractive Metallurgy, pp. 133–199. Plenum Press, New York (1979)
23. Georgiou, D.; Papangelakis, V.G.: Sulphuric acid pressure leaching of a limonitic laterite: chemistry and kinetics. Hydrometallurgy **49**, 23–46 (1998)
24. Anand, S.; Das, S.C.; Das, R.P.; Jena, P.K.: Leaching of manganese nodules at elevated temperature and pressure in the presence of oxygen. Hydrometallurgy **20**(2), 155–167 (1988)
25. Lozano, L.J.; Juan, D.: Leaching of vanadium from spent sulphuric acid catalysts. Min. Eng. **14**(5), 543–546 (2001)
26. Mulak, W.; Miazga, B.; Szymczycha, A.: Kinetics of nickel leaching from spent catalyst in sulphuric acid solution. Int. J. Min. Process. **77**(4), 231–235 (2005)
27. Abdel, E.A.: Kinetics of sulfuric acid leaching of low-grade zinc silicate ore. Hydrometallurgy **55**(3), 247–254 (2000)
28. Feng, Q.M.; Shao, Y.H.; Ou, L.M.; Zhang, G.F.; Lu, Y.P.: Kinetics of nickel leaching from roasting-dissolving residue of spent catalyst with sulfuric acid. J. Central South Univ. Technol. **16**, 0410 (2009)
29. Chauhan, G.; Pant, K.K.; Nigam, K.D.P.: Extraction of nickel from spent catalyst using biodegradable chelating agent EDDS. Ind. Eng. Chem. Res. **51**, 10354–10363 (2012)

Chemical Engineering Journal Advances 7 (2021) 100132

Contents lists available at ScienceDirect

Chemical Engineering Journal Advances

journal homepage: www.elsevier.com/locate/ceja

Study on empirical models of isobaric heat capacities and conductivities for ammonium salt-based DESs

K.J. Suthar, M.H. Joshipura*

Department of Chemical Engineering, Nirma University, Ahmedabad, India

ARTICLE INFO

Keywords:
DES
Heat capacity
Conductivity
Empirical models
Mass connectivity
ANN

ABSTRACT

In this research, a comparative evaluation of empirical models for the fundamental transport properties of DESs is presented. The detailed knowledge about the properties of DESs is critically important to rationally extend the utilization of DESs. The accurate information about these properties plays a vital role in transferring the laboratory scale applications to large industrial scale. In this regard, the ammonium salt-based 5 DESs were synthesized to study empirical models for conductivities within the temperature range of 298.15 to 323.15 K. The experimental isobaric heat capacity data of 17 ammonium salt-based DESs covering 326-data points with a temperature range of 293.15 to 353.15 K were collected from the open literature. Six models including group contribution – mass connectivity index (GC-MCI) and artificial neural network (ANN) were applied for modeling and predicting heat capacities. The GC-MCI and ANN showed good agreement with the experimental data. The error values of the GC-MCI model (R^2 = 0.9863), and AAD = 2.25%) and ANN model (R^2 = 0.9982 and AAD = 0.55%) were calculated. Three models were employed for studying conductivities of DESs. Results for conductivities show that the 4-parameters GH model gave low deviation (R^2 = 0.9984 and AAD = 2.63%) compared to VFT (R^2 = 0.9950 and AAD = 3.11%) and ARH (R^2 = 0.9942 and AAD = 5.30%).

1. Introduction

There is a proliferation in research on Deep Eutectic Solvents (DESs) since last two decades as it is considered to be inexpensive environmentally benign alternative to ionic liquids [1]. The ILs have attracted the researchers due to the desirable solvation properties, high thermal stability, low vapor pressure and good ionic conductivity with electrochemical stability [2,3]. Despite attractive properties, ILs are not commercialized to the extent of its potential. Few of the reasons hindering the commercialization of ILs are the non-biodegradable nature and the need of expansive raw materials for synthesizing it. ILs, as reported are even toxic in some cases [4,5]. Unlike ILs, DESs are biodegradable, relatively lass expansive and easy to synthesize [1]. Due to these unique features, the DESs has shown a practical use in applications such as biodiesel purification [6,7], microextraction [8,9], capturing CO_2 [10,11], synthesis of organic compounds [12], bio-catalysis [13,14] and electroplating of metals [15]. The quaternary ammonium salts-based DESs finds the applications in the diversified fields of science and engineering which includes extraction, biotechnology, microextraction, batteries, nanoscience, membrane technology applications, etc. [16-18]. These applications are all reported at the laboratory scale. The knowledge of thermophysical properties is important to rationally extend the applications and transfer the laboratory scale DES applications to large industrial scale. The molar heat capacity and conductivity are fundamental properties that are necessary to assess the appositeness of DESs for engineering applications of heat transfer and thermodynamic.

The molar heat capacities (C_p) can be used to calculate various thermodynamic properties, such as enthalpy, entropy, and Gibbs free energy as a function of temperature [19]. The accurate knowledge of these properties is required for the designing the unit operations such as evaporation, separation column and heat transfer commonly found in the chemical process industries [20]. The electrical conductivity indicates the resistance of a material and it also useful in various industrial instruments. The information of electrical conductivity of DESs is crucial in engineering applications for designing, controlling and optimizing the processes associated with electrolysis and electrochemical power sources. Conductivity is an important property as it provides information for assessing the corrosivity of aqueous media and for cathodic protection system. The measurement and prediction of conductivity are significant as one of the major applications of DESs is electrochemical fields.

A generalized and easy-to-use model for estimating molar heat capacity and conductivity are important as experimental determination of large variety of DESs is strenuous. Chen et al. employed group contribution method (GCM) for estimating molar heat capacity of 61 ILs ranging from 189.66–524.87 K [21]. Further, Gardas et al. used GCM for the

* Corresponding author at: Chemical Engineering, Nirma University, Ahmedabad, India.
E-mail address: milind.joshipura@nirmauni.ac.in (M.H. Joshipura).

https://doi.org/10.1016/j.ceja.2021.100132
Received 3 February 2021; Received in revised form 27 April 2021; Accepted 29 May 2021

prediction of 19 ILs [22]. Similarly, Ge and co-workers corrected the GCM for 9 ILs with temperature ranging from 293 to 358 K resulting in 2.9% deviation when tested over 53 ILs [23]. Strechan et al. proposed a model for six ILs for estimating molar heat capacities based on intramolecular vibrational contribution which requires intricate calculations [24]. Recently, Taherzadeh et al. (TM) developed a correlation to estimate heat capacities of 28 DESs which resulted in 4.7% overall deviation [25]. Valderrama et al. (VRM) developed a prediction model for 146 ILs using a concept of mass connectivity index (MCI) [26]. The VR-model predicted heat capacities with good agreement but the model was dependent on the molar volume with six universal constants involved. The same group of researchers modified the MCI based model combining the group contribution method with the concept of MCI [27]. The combination of group contribution and mass connectivity index (GC-MCI) model was trained for 126 organic solvents along with 36 ILs resulting in a higher degree of agreement. The majority of the models reported aimed at the prediction of heat capacity for ILs but the estimation work for DESs is scarce. Moreover, to the best of the author's knowledge, the data-driven ANN model was reported to be employed for the first time over heat capacity.

Most of the researchers have adopted the well-defined molar ratio of HBD and HBA for synthesizing DESs. It is often argued that the formation of complex DESs is connected to the fixed stoichiometric ratio of HBAs and HBDs which is also a proof of solvent formation [28,29]. A good explanation of relaxing the fixed stoichiometries proportions of DESs and the resulting major advantages is published by Coutinho and co-workers [30]. The consideration of molar ratios of HBAs and HBDs allowing the existence of liquid phase of DESs at room temperature leads to an extra degree of freedom enhancing tunability and designer characteristic of DESs [31]. Changing the initial material or their molar ratio leads to the new DESs with difference thermo-physical properties. These facts, leads to the possibilities of preparing a sizable number of DES for which the experimental investigation is impractical. Therefore, there is a need to have a simple, yet easy-to-use model for estimation of transport properties. Moreover, the majority of the property estimation work is focussed on ILs. The present study of empirical models of isobaric heat capacities and conductivities is inspired by these facts to fill the mentioned gap in the literature. The six models including the artificial neural network were employed for estimating the molar heat capacities of DESs and three models were employed for correlating conductivities. The study on the thermophysical properties is reported as per the guidance given in the IUPAC Technical Report [35].

2. Material and methodology

The Hydrogen Bond Acceptors (HBAs), Choline chloride (ChCl) [CAS 67–48–1] and Tetra-n-butylammonium bromide (TBABr) [CAS 1643–19–2] were purchased from Loba chemie with purities >98.5% and the HBDs, glycerol [CAS 56–81–5], ethylene glycol (EG) [CAS 107–21–1], triethylene glycol (TEG) [CAS 112–27–6] and urea [CAS 57–13–6] were purchased from Rankem chemicals (purities >99%).

DESs were synthesized in a 100 mL glass vessel with a self-mount motored agitator to mix HBAs and HBDs in different molar ratios with temperature maintained at 353.15 K using a water bath. The mixing was done at 300 rpm until a clear homogeneous colourless liquid was formed. The synthesized DESs were stored in a tightly packed sample bottle to avoid contamination. The conductivity was measured using conductometer EI101. The cell was calibrated using aqueous (0.01 M) KCL as per standard method. The conductivity was measured at an interval of 5 K for temperature range of 298.15–323.15 K. The temperature was monitored using UNIX PPI96 (self-tuned PID temperature controller) and maintained using a water bath. The experiments were performed in triplicate. The relative deviation in the data of three replicated experiments was found to be less than 1%. The presented values of conductivities in the present study are the average of the result measured from the three repeated experiments with similar experimental condition. The standard uncertainties of temperature and conductivity were within the range of 0.004 mS cm-1 and ±0.05 K respectively.

The moisture content was measured using Karl Fisher titration and the values were found to be less than 0.0065 mass faction for all synthesized DESs. The IR spectroscopy and water content of 5 synthesized DESs were determined using Shimatzu IR-Pristige21.

The heat capacities of ammonium-salt based DESs available in the open literature were collected covering 17 DES and 326 data points ranging from the temperature of 298.15 to 353 K at atmospheric pressure [32-34]. The collected DESs consisted of 3 quaternary ammonium salts including choline chloride (ChCl), N,N-diethylethanolammonium (DEAC) and tetrabutyle ammonium chloride (TBAC). The considered 13 hydrogen bond donors (HBDs) included citric acid (CA), ethylene glycol (EG), fructose, glucose, glycerol, malonic acid (MA), oxalic acid (OA), phenol, tryethylene glycol (TEG) and urea. The molecular structure of all the components is shown in Fig. 1.

The DESs synthesized and considered in the present study are listed in Table 1 along with molar ratio and molecular weight. The basic information, including molar mass, functional groups, number of groups and MCI values of the compounds considered in the present study are made available in the supplementary data Table 1S.

The FTIR was studied for synthesized DESs, and the plots are shown in Fig. 2. The IR spectroscopy study revealed the presence of $O-H$ stretching bands between the wavelength of 3200 and 3500 cm^{-1}. The O–H stretching bond can be found prominently in all the 5 synthesized DESs. The FTIR of DES_{10} was compared and the peaks were confirmed to be same with the previous published study [36]. The existence of Cl^- halide ions is depicted by the peak at the wavelength of 725 – 722cm^{-1} [37]. The peak at the wavelength 2869 cm characterizes the N–H stretching bond which is common for the studied ammonium based DESs [38].

The models evaluated for its capabilities of predicting heat capacities and conductivities are listed in Table 2. [39-42].

2.1. Heat capacity models

The GM and TM models requires the critical properties and acentric factor of DESs for prediction of heat capacities. The critical properties and acentric factors were calculated using the modified Lydersen and Joback-Reid method (LJR) [43] for ammonium-based salt and HBDs separately. Later, the Lee-Kesler (LK) mixing rule suggested by Khapp et al. [44] was employed over DESs. The estimated values of critical properties and acentric factor for DESs are available in the supplementary data Table 2S.

The two methods (VRM and GC-MCI) considered in the study were based on the concept of mass connectivity originally introduced Valdrrama and Rojas for prediction of density of ILs [45]. The concept of mass connectivity allows the contribution of molecular branching which is vital for complex liquids (ILs and DESs). The MCI was easily calculated using the following equation with an exact knowledge of molecular structure.

$$\lambda_m = \sum \left(\frac{1}{\sqrt{m_i m_j}} \right)_{ij} \quad (1)$$

In the above equation-1, the λ_m is the mass connectivity index, m_i and m_j are the mass of neighbouring groups i and j in a considered molecule. The calculation of MCI was illustrated in the density prediction work of Valdrrama and Rojas [45].

The ANN model architecture was adopted and developed for the estimation of heat capacity using a computational tool SPSS by IBM. The ANNs are powerful input-out based mathematical models with an ability to solve simple and complex problems in the diversified fields of science and engineering [46]. The developed ANN model used 70% of the overall heat capacities database as training data set and the other 30% data points were used for the testing purpose. The training and tested datapoints were randomly selected from the overall database. The network

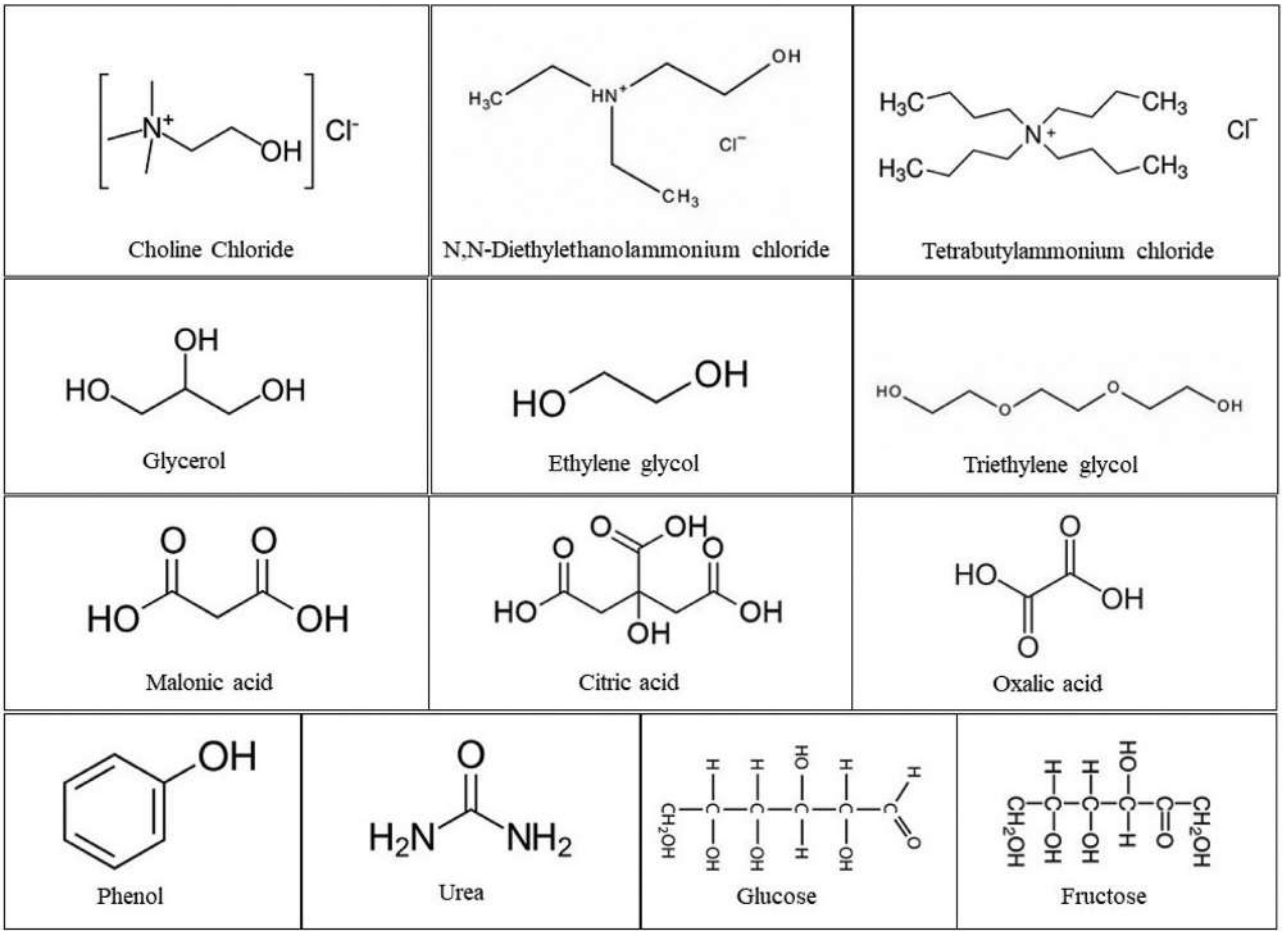

Fig. 1. Molecular structure of the quaternary ammonium salts and HBDs.

Table 1
List of DESs considered in the present study.

DESs	Salt	HBD	MR	[a]T_r (K)	[b]M_w (g mol^{-1})	[c]N_p
DES_1	ChCl	CA	1:2	298.15 – 353.15	174.62	23
DES_2*	ChCl	EG	1:2	303.15 – 353.15	86.58	11
DES_3	ChCl	Fructose	2:1	298.15 – 353.15	153.13	23
DES_4	ChCl	Glucose	2:1	298.15 – 353.15	153.13	23
DES_5*	ChCl	Glycerol	1:2	303.15 – 353.15	107.93	11
DES_6	ChCl	MA	1:1	298.15 – 353.15	121.84	23
DES_7	ChCl	OA	1:2	298.15 – 353.15	106.56	23
DES_8	ChCl	Phenol	1:2	298.15 – 353.15	105.49	23
DES_9*	ChCl	TEG	1:2	298.15 – 353.15	146.65	23
DES_{10}*	ChCl	Urea	1:2	308.15 – 353.15	86.58	10
DES_{11}	DEAC	EG	1:2	303.15 – 353.15	92.60	11
DES_{12}	DEAC	Glycerol	1:2	303.15 – 353.15	112.61	11
DES_{13}	TBAC	EG	1:3	298.15 – 353.15	116.03	23
DES_{14}	TBAC	Glycerol	1:5	298.15 – 353.15	123.06	23
DES_{15}	TBAC	MA	1:3	298.15 – 353.15	147.52	23
DES_{16}	TBAC	TEG	1:1	298.15 – 353.15	214.04	23
DES_{17}	TBAC	Urea	4:1	298.15 – 353.15	214.04	19
DES_{18}*,[d]	TBAB	Glycerol	1:3	298.15 – 323.15	149.67	06

* DESs synthesized in the present study.
[a] Temperature range for heat capacity.
[b] molecular weight.
[c] Number of points and.
[d] DES_{18} was not considered for heat capacity study.

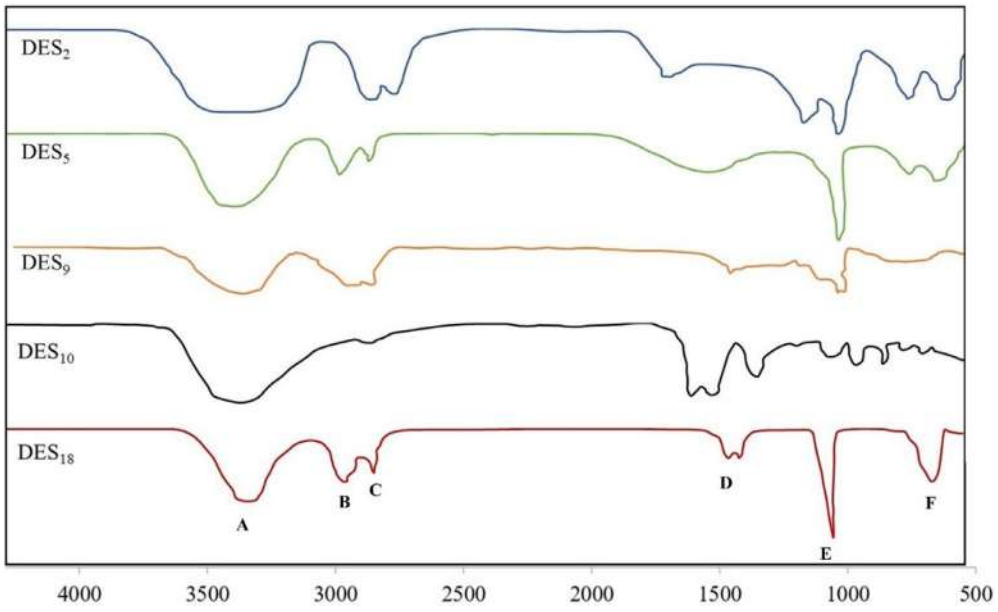

Fig. 2. FTIR of 5 synthesized DESs. (A) O–H stretching (B) C–H stretching (C) N–H stretching (D) C–H bending (E) C–O stretching/O–H bending (F) Cl^- halide.

Table 2
Predictive heat capacity and conductivity models considered in the present study.

Model	Equation	References
Group Contribution Method (GCM)	$C_{pL} = R[A_{Cp} + B_{Cp}\frac{100}{T} + D_{Cp}(\frac{100}{T})^2]$ $A_{Cp} = \sum_{i=1}^{k} n_i a_{i,Cp} \quad B_{Cp} = \sum_{i=1}^{k} n_i b_{i,Cp} \quad D_{Cp} = \sum_{i=1}^{k} n_i d_{i,Cp}$ R is the gas constant 8.314 J mol^{-1} K^{-1} and T is the absolute temperature (in Kelvin) n_i is the number of groups of type i and $a_{i,Cp}$, $b_{i,Cp}$, and $d_{i,Cp}$ are the group contributions parameters	21
Ge et al. (GM)	$\frac{C_{pL}}{R} = 1.586 + \frac{0.49}{1-T_r} + \omega[4.2775 + \frac{6.3(1-T_r)^{1/3}}{T_r} + \frac{0.49}{1-T_r}]$ R is the gas constant 8.314 J mol^{-1} K^{-1}, T_r is the reduced temperature and T is the absolute temperature (in Kelvin)	23
Taherzadeh et al. (TM)	$C_{PL} = A + BT^{1/4}$ $A = A_1\frac{M_w^3}{P_c^6} + A_2 M_w^{2\omega} + \frac{A_3}{M_w} + A_4$ A_1, A_2, A_3, A_4 and B are the adjustable parameter Mw, Pc, ω are the molecular weight (g. mol^{-1}), critical pressure (bar), and acentric factor respectively	24
Valderrama et al. (VMR)	$C_{pL} = a + bV + c\lambda + d\eta + \lambda[e(T - T_o) + f(T^2 - T_0^2)]$ Where a, b, c, d, e and f are the constants fitted for ILs, λ is the MCI and η is ratio between the mass of the cation and that of the anion for ILs	26
GC-MCI	$C_{pL} = \Sigma n_i G_i + A + B\lambda + \lambda[CT + DT^2]$ A = 9.0045, B = −100.70, C = 0.3918 and D = -1.952×10^{-4} are the constants adjusted for ILs n_i is the number of functional groups, G_i is the value of group and λ is the MCI	27
Arrhenius equation (ARH)	$k = k_0 e^{(\frac{E_k}{RT})}$ Where, where κ is the conductivity in mS cm^{-1}, k_0 is the constant parameter and E_k is the activation energy of conductivity in kJ mol^{-1}; R is the gas constant in J.$mol^{-1}K^{-1}$ and T is the temperature in Kelvin	39, 40
Vogel-Fulcher-Tammann (VFT)	$ln\kappa = lnA + {B}/{T - T_0}$ where κ is the conductivity in $mScm^{-1}$, A, B and T_0 are the constant parameter and T is the temperature in Kelvin.	41, 42
Ghaedi Hosein (GH)	$ln(\frac{\kappa}{\rho M}) = A_0 + \frac{A_1}{T} + \frac{A_2}{T^2} + \ldots \frac{A_n}{T^n} = \sum_{i=0}^{n}\frac{A_i}{T^i}$ where κ is the conductivity in $mScm^{-1}$, A_i ia the constant parameter, ρ is density, M is average molar mass of DES and T is temperature in Kelvin.	40

has three layers: an input layer, single or multiple hidden layers and an output layer which is connected to each other through the direct communication links. These links consist of the neural network parameter in terms of weights (w_i) and biases (b_i) [47]. The weight and biases along with the selected activation function passes the network information in forward direction defining the output of neural. In mathematical terms, the output of a neuron is evaluated by following equation;

$$n_i = f\left(\sum_{i=1}^{N} w_i c_i + b_i\right) \tag{2}$$

where, n_i is the net input to node i, $w_i$is the weight of the link between subsequent layer, c_i is the covariant or the input parameter, b_i is called bias and f is the activation function. The selection of activation function is dependent on the type of the scaling method selected for the output parameters.

2.2. Conductivity models

The ARH, VFT and GH models listed in Table 2 were employed to estimate conductivities in the present study. The conductivity increases with increasing temperature and increasing molar ratio of HBDs as reported Mjalli et al. [48]. The study on conductivities of TEG as HBD-based DESs was carried out within the temperature range of 298.15 to 353.15. The Arrhenius-like equation was used to successfully predict

the conductivities as a function of temperature [49]. Siongco and co-workers measured conductivities of two ammonium based DESs with temperature range of 298.15 to 343.15 K and used the Arrhenius-like equation to predict conductivities resulting in overall 1.13%AAD [33]. AlOmar et al. also employed Arrhenius-like equation correlating conductivities within the temperature range 293.15 K–343.15 K with coefficient of determination (R^2) greater than 0.96 [50]. Ghaedi et al. proposed a new model predicting conductivities for six phosphonium based DESs resulting in 1.97%AAD [40]. Bagh et al. developed artificial neural network for predicting conductivities of 18 DESs resulting in overall average absolute relative deviation of 4.40%AAD [51]. Saoudi et al. studied conductivity-viscosity correlation and found that the conductivity does not strictly control the viscosity variation [39].

In the present work, three empirical models were employed to predict conductivities. The ARH is the most commonly employed model for estimating conductivity. The VFT model has one extra parameter compared to ARH. The truncated GH-model with three terms on right hand side was employed. The data of density and molar mass of considered DESs were prerequisite to employ GH model. The required density was predicted using VR-model [52]. The predicted densities are provided in supplementary information Table-6S. The molar mas was estimated using following expression.

$$M_w = X_{HBA} M_{HBA} + X_{HBD} M_{HBD} \tag{3}$$

In this equation, X_{HBA} and M_{HBA} are the mole fraction and molecular weight of HBA respectively. X_{HBD} and M_{HBD} are the mole fraction and molecular weight of HBD respectively.

3. Results and discussions

The statistical and graphical analysis for the evaluation of correlations to validate accuracy and reliability were carried out using the correlation coefficient (R^2), percentage average absolute deviation (%AAD) and percentage relative deviation (%RD).

$$R^2 = 1 - \frac{\sum_{i=1}^{n} \left(P_i^{pred} - P_i^{exp} \right)^2}{\sum_{i=1}^{n} \left(P_i^{pred} - \overline{P_i} \right)^2} \tag{4}$$

$$\%AAD = \frac{100}{n} \sum_{i=1}^{n} \left| \frac{P_i^{pred} - P_i^{exp}}{P_i^{exp}} \right| \tag{5}$$

$$\%RD = 100 \left(\frac{P_i^{pred} - P_i^{exp}}{P_i^{exp}} \right) \tag{6}$$

In the above equations, n is the number of datapoints, $\overline{P_i}$ is the mean value of experimental data, P_i^{pred} and P_i^{exp} are the predicted and experimental properties for component, i respectively.

3.1. Heat capacity

The six empirical models considered in the study gave varying results. Thus, further the prediction capabilities were evaluated and the model was recommended considering the following criteria and facts: (i) correlation coefficient, (ii)%AAD, (iii)%RD, (iv) number of data with relative derivation less than 1% and (v) easy-to-estimate input parameters. Based on these performance criteria, the models were evaluated.

The 14-functional groups present in the 13-components used to synthesize the considered DESs were regressed for estimation of heat capacity using GCM method. The calculated results of group contribution parameters within the temperature range of 298.15–353.15 K are listed in supplementary data Table 3S. The model resulted in overall 8.5%AAD with maximum deviation of 50% observed for DES_{16}. The GCM estimated 42.33% and 73.93% of the overall dataset with less than 1% and 10% AAD respectively.

Table 3
Generated values of functional groups and constant used in GC-MCI model.

Groups and constants	$a_{i,Cp}$
$-CH_3$	296.82
$-CH_2-$	−331.54
-OH	−122.97
Cl-	−1476.44
>*N*-	−676.54
>CH-	−383.48
>*C*<	−516.64
-O-	−181.73
>*C* = *O*	−155.03
$-NH_2$	−306.59
=CH- (ring)	−1.68
=*C*< (ring)	−619.92
OH (ring)	−523.81
-CHO	1148.93
A	399
B	2002
C	0.6663
D	−8.40E-04

The GM correlations utilized the principle of corresponding states which required the values of critical properties. The GM was the oldest model considered in the present study. The model resulted in 14.94% overall AAD. The third model (TM) considered in the present study was a function of molecular weight, critical properties and acentric factor. The model predicted the heat capacities with an overall 5% AAD (R^2 = 0.9643) with 77.6% overall data resulting in deviation less than 10%. Like GM, the (TM) model required the critical properties and acentric factor. The calculation of critical properties and acentric factor using LJR method was arduous with certain degree of inaccuracy involved.

The MCI-based VRM model considered the contribution of structural bonding. The two versions of VMR model were originally developed for estimating heat capacities of ILs. The first required at least one reference value for estimating heat capacity and the second model was a function of molar volume. The model utilizing the reference value showed an obvious superior predictive capability of overall 3.31% AAD. The second version of VMR considered molar volume along with six adjustable constants. The molar volume in the present study was assumed to be ideal and the six universal constants were adjusted to the collected experimental values of heat capacities. The adjusted constants are listed in the supplementary data Table 4S. Despite the large number of adjustable parameters, the VMR model predicted heat capacities with relatively poor accuracy.

The GC-MCI model considered the structural bonding of DESs eliminating the use of reference value as in the case of VRM model. The first term in the GC-MCI model was calculated using group contribution method. The values of 13 functional groups were corrected using central derivatives mathematical approach. The 3 universal constants which are functions of MCI and temperature were fitted against the collected experimental database. Table 3 shows the generated values of functional groups and universal constants used in GC-MCI model. The model resulted in the overall 2.2% AAD (R^2 = 0.9863). The GC-MCI method result showed good agreement with the considered criterion for selection of empirical model for estimation of heat capacities. The values of heat capacities for all 17-DESs were estimated using GC-MCI. The experimental and predicted values of randomly selected 5-DESs are shown in the Fig. 4.

The adopted ANN architecture (5–9–1) model for heat capacity estimation is shown in Fig. 3. In this study, the easy-to-estimate covariances (temperature, molecular weight, MCI, mole fraction of HBAs and HBDs) were used as input to the ANN architecture. The single output variable was selected, namely the heat capacity of DESs. The increase in the neutron in hidden layer resulted in a significantly low value of

Table 4
Network information of ANN model.

Input Layer	Covariates	1	Temperature (T)
		2	Average molecular weight (AvgMW)
		3	MCI
		4	Mole fraction of HBA (X_{salt})
		5	Mole fraction of HBD (X_{hbd})
	Number of Units		5
	Rescaling Method for Covariates		Standardized
Hidden Layer(s)	Number of Hidden Layers		1
	Number of Units in Hidden Layer-1		9
	Activation Function		Hyperbolic tangent
Output Layer	Dependent Variables	1	Cp
	Number of Units		1
	Rescaling Method for Scale Dependents		Normalized
	Activation Function		Sigmoid
	Error Function		Sum of Squares

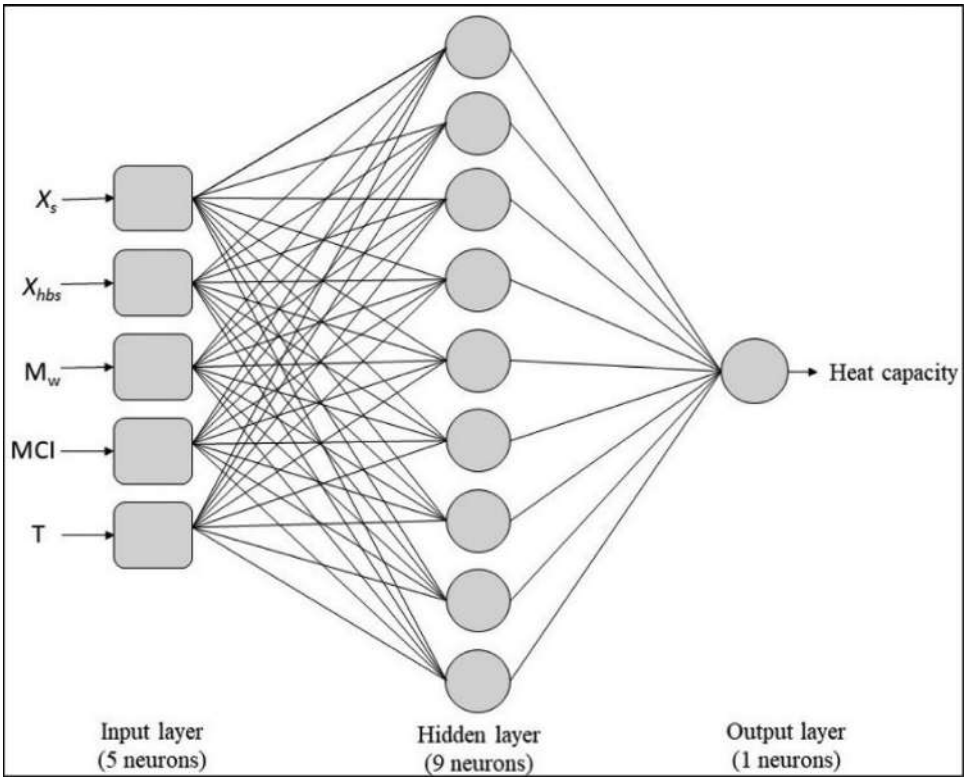

Fig. 3. Adopted (5–9–1) ANN architecture for heat capacity.

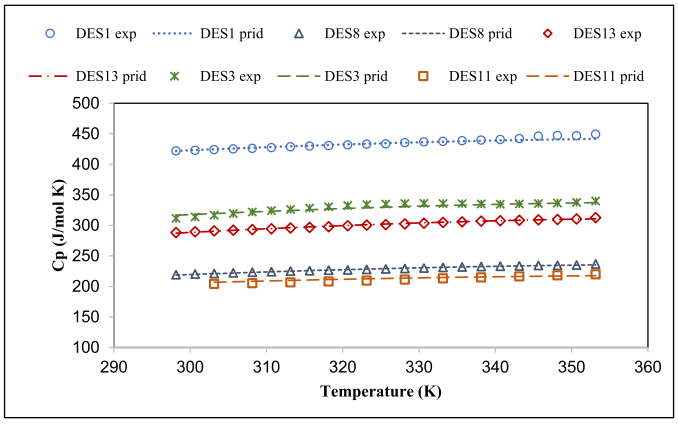

Fig. 4. Plot of heat capacities as a function of temperature using GC-MCI.

a bias neuron which suggested the overestimation of the model with more than 9 units in the hidden layer. It was observed that less than 9-neural of hidden layer ware under fitting the model and resulted in poor estimation of heat capacity. In such cases, it is recommended to add more hidden layer, increase neurons to the hidden layer and increase more input parameters to avoid the under filling of the model. The addition in the hidden layer showed similar results. The multilayer perceptron approach was adopted to test the available learning algorithms (steepest descent and scaled conjugate gradient) and activation function (hyperbolic tangent, identity, sigmoid and softmax) in a computational tool. Based on the minimum%AAD and maximum R^2 output values, the scaled conjugate gradient algorithm was adopted. The activation function connecting the input to a hidden layer was selected as hyperbolic tangent and the one connecting hidden layer to the output layer was linear activation function. Based on the statistical assessment, the optimum neural network was selected. The network information of the optimized ANN model is given in Table 4. The parameters (weights and biases) of the optimized ANN architecture are available as

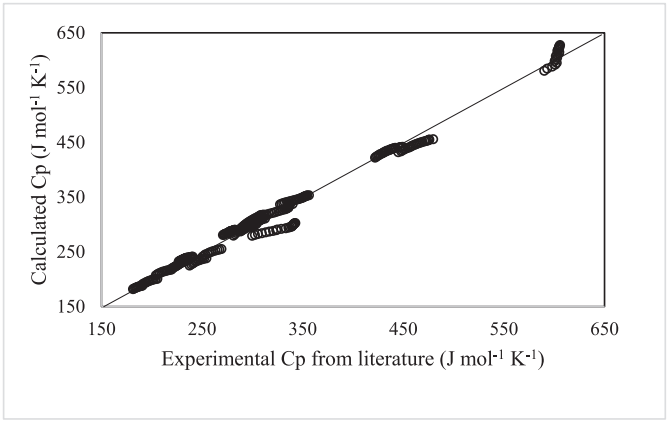

(a)

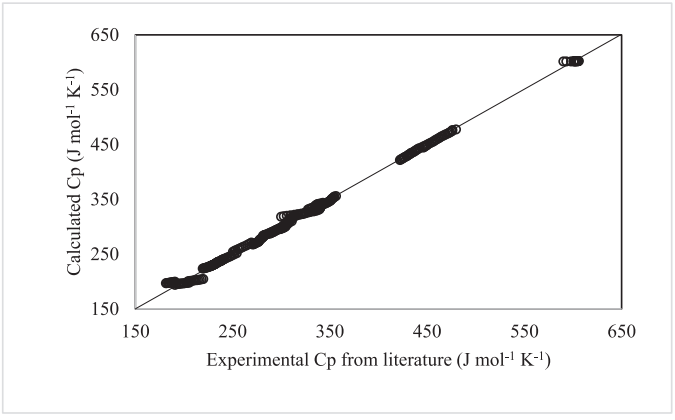

(b)

Fig. 5. (a) Scatter plot comparing calculated versus experimental for heat capacities using GC-MCI model.
(b) Scatter plot comparing calculated versus experimental for heat capacities using ANN model.

Table 5
Result summary of models used for estimation of heat capacity.

Models →	GCM	GM	TM	VMR	GC-MCI	ANN
Avg.%AAD	8.48	14.94	5.00	15.28	2.25	0.55
% data <1% AAD	48.33	4.91	32.82	13.50	42.33	80.68
% data >5% AAD	37.42	75.15	36.50	73.61	10.12	0.00

supplementary information. The AAD were given 0.49% (R^2 = 0.9985), 0.69% (R^2 = 0.9978) and 0.55% (R^2 = 0.9983) for, trained, tested and all overall datasets, respectively. Based on the assessment using the performance criteria, GC-MCI and ANN model clearly shows better predictive capability for heat capacities of ammonium salt-based DESs. The scatter diagram of estimated values versus experimental data points of heat capacities collected from literature was plotted in Fig. 5 for GC-MCI and ANN models. The distributing of%RD of estimated heat capacities was plotted against temperature for GC-MCI and ANN models in Fig. 6 showing the narrower range of the relative deviation for ANN compared to GC-MCI. Table 5 summarizes the results, showing various ranges of deviation for models considered in the present study. Similar results (as depicted in Table 5) are shown in the form of distribution of%RD over temperature for 5 correlations (except ANN) in Fig. 6.

These overall results of heat capacity predictive studies suggest that the prediction capability of ANN model is higher than the GC-MCI model. Though, the GC-MCI model has an advantage of simple and easy-to-estimate (chemical structure based) input parameters having some physical significance and capable of capturing the non-ideality of DESs.

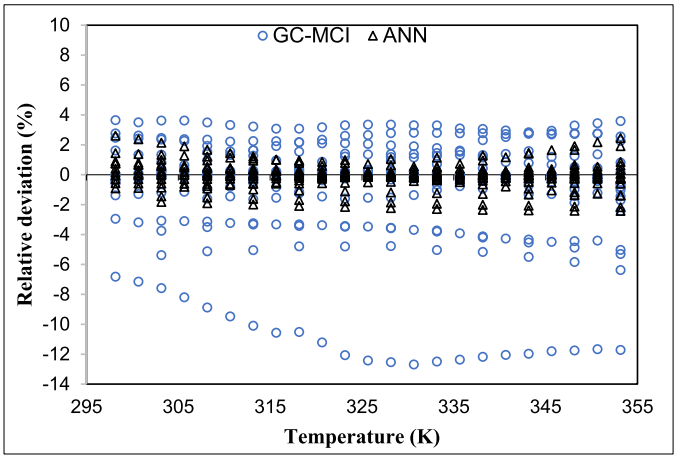

Fig. 6. Distribution of%RD against temperature for heat capacities.

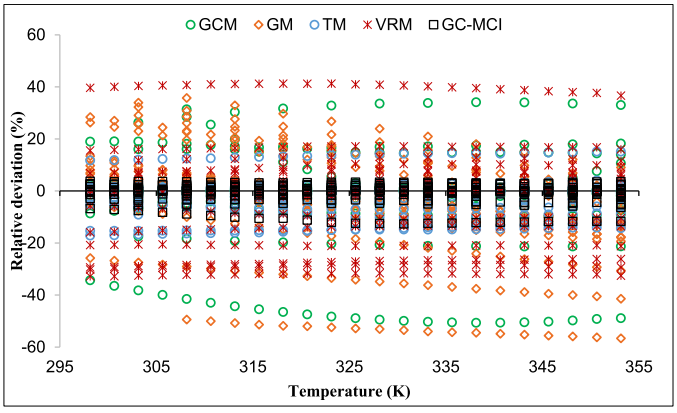

Fig. 7. Distribution of%RD against temperature for correlations used for heat capacity.

3.2. Conductivity

The electrical conductivity exponentially increased with increasing in temperature. The conductivity reported by Harif-Mood and co-workers for DES_2 was 11 $mScm^{-1}$ – 17.36 $mScm^{-1}$ for temperature range of 308.15K-323.15 K. Similarly, Bagh et al. [48] reported conductivity for DES_5 in the range of 1.75 $mScm^{-1}$ – 5.12 $mScm^{-1}$ for a temperature range of 298.15K-323.15 K. For the same temperature range, the conductivity of DES_5 was measured in the range of 1.69 $mScm^{-1}$ - 4.45 $mScm^{-1}$ in the present study. The measured conductivities are in line with the published and available database in an open literature.

The tendency of the six DESs for conductivities at a temperature of 298.15 K are as follows: DES_2 > DES_{11} > DES_5 > DES_9 > DES_{10} > DES_{12} > DES_{18}. The of DES_{18} resulted in the low conductivities compared to the other studied DESs. The low range of conductivities attributes to the chemical composition of HBAs an HBDs. The higher molar proportion of quaternary salt increases the number of charge-carriers in the eutectic solution. The DESs with lower conductivity than 0.1 $mScm^{-1}$ is not recommended for the electrochemical applications [53]. The conductivity of DES made from TBAB and glycerol (DES_{18}) with a higher molar proportion of glycerol (1:3 molar ratio) was not found to be in the aforesaid range. Also, the DES_{12} formed using DEAC and glycerol (1:2 molar ratio) shows the lower electrical conductivity (0.75 $mScm^{-1}$) at 298.15 K. The

Table 6
Estimated parameters and%AAD of the models for DESs conductivities.

Models	DES_2	DES_5	DES_9	DES_{10}	DES_{11}	DES_{12}	DES_{18}
ARH							
K_0	1.49E-03	2.15E-05	3.00E-05	8.00E-07	7.45E-06	1.90E-06	3.00E-08
E_k/R	2.89E-02	3.79E-02	3.63E-02	4.80E-02	4.44E-02	4.44E-02	4.59E-02
%AAD	2.28	2.09	4.98	4.89	7.02	12.93	3.09
VFT							
A	34.02	22.22	12.79	25.30	32.47	13.83	30.53
B	−44.00268.78	−107.69257.32	−78.28263.11	−118.79	−67.62264.45	−73.72272.86	−881.96174.06
T_0	268.78	257.32	263.11	259.18	264.45	272.86	174.06
%AAD	3.49	2.39	1.02	1.38	3.54	8.18	1.79
GH							
A_0	−309	−330	−324	−323	−330	−331	−337
A_1	2.89E+05	2.96E+05	2.90E+05	2.93E+05	2.96E+05	2.98E+05	2.93E+05
A_2	8.96E+07	8.81E+07	8.65E+07	8.55E+07	8.80E+07	8.85E+07	8.55E+07
A_3	9.18E+09	8.61E+09	8.47E+09	8.13E+09	8.61E+09	8.57E+09	8.13E+09
%AAD	1.56	1.63	1.85	1.38	2.37	7.56	2.09

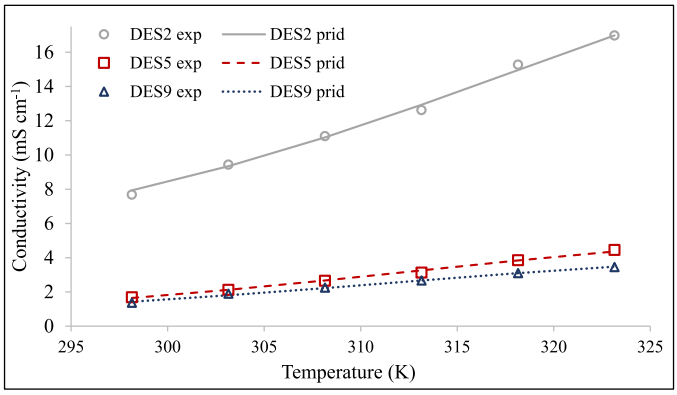

Fig. 8. Experimental vs estimated conductivities as a function of temperature.

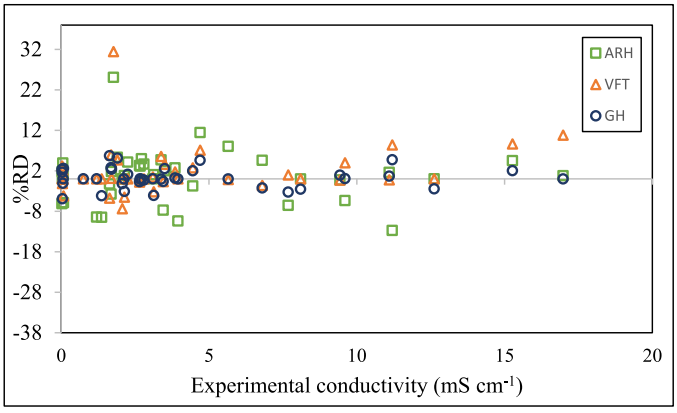

Fig. 9. Distribution of%RD against temperature for correlations used for conductivity.

probable reason for low conductivity of DESs having high salt concentration is due to reduced overall mobility caused by the strong influence of ion pair.

The error values of ARH model (R^2 = 0.9942, AAD = 5.30%), VFT model (R^2 = 0.9950, AAD = 3.11%) and GH model (R^2 = 0.9984, AAD = 2.66%) were calculated. The results showed that all three studied models showed good agreement with an experimental data, but four-parameter GH model was more reliable than the other two. The estimated constant parameters and%AAD of all three models are listed in Table-7. GH and VFT model estimated 66.67% overall conductivity data with less than 1% deviation, whereas ARH estimated 54.76% of the overall data with less than 1% deviation. The experimental and estimated values are plotted in Fig. 8. The overall percentage relative deviation was plotted against temperature in Fig. 9 which clearly showed that the GH model is superior than the other two considered models. The model employed over ammonium salt-based DESs family showed promising results and the model can be further extended over a variety of DESs making it a more generalized one for DESs.

4. Conclusions

The heat capacities and conductivity were estimated using empirical models for ammonium based DESs. It was revealed that the TM, GC-MCI and ANN model have ability to predict heat capacities of DESs. Among these models, the TM correlation requires the value of critical properties and acentric factor which are not readily available. A GC-MCI correlation and data driven ANN model resulted in an overall 2.25% and 0.55% AAD. Based on the performance criteria, the ANN model showed higher prediction capabilities. In the performance criteria, if more weightage is given to the easy estimation and significance of input parameters, the GC-MCI model is recommended for predicting heat capacities of DESs. The GC-MCI model is function of mass connectivity, molar ratio and temperature and it can be confidently used to predict heat capacities of the variety of ammonium salt-based DESs. The other influencing factors such as molecular weight, water and impurity content can contribute in further improving the prediction capability.

Furthermore, the study on conductivity prediction models revealed that the VFT correlation (3.11%AAD) can be used for fitting of the experimental data with higher prediction capability compared to ARH model (5.30%AAD). Based on the statistical assessment, the 4-parameter GH model showed the least deviation (2.63%AAD) but the model is density dependent. Among the models studied, GH model is recommended for fitting the experimental conductivities if accurate density data are available at the temperatures. The results also revealed that the values of conductivity increase significantly with increase with temperature and a decrease with the HBA composition for DESs. As an outcome of this study, the strengths and weaknesses of studied models are summarized in Table 7a for heat capacity and Table 7b for conductivity. The studied empirical models can be further extended considering a larger database for a wide variety of DESs particularly for conductivity.

Declaration of Competing Interest

The authors declare that they have no known competing financial interests or personal relationships that could have appeared to influence the work reported in this paper.

Table 7a
Strengths and weakness of considered heat capacity models.

Model	Strengths	Weakness
GCM	• Less input data requirement • Simple to apply and universal model	• Requirement of components specific constants • Completely empirical in nature and • More computational burden
GM	• Simple and generalized model in nature • Accurate prediction for conventional organic solvents	• Requires critical properties which are not readily available, • Poor prediction capability
TM	• Employable over wide range of DESS, • Good predictive capability and • Generalized in nature	• Requirement of critical properties which are not readily available and estimation of critical properties depends on group contribution method
VMR	• Good accuracy if reference values are available, • Limited input parameters	• Requirement of molar volume • Poor prediction capability considering ideal molar volume
GC-MCI	• Simple and accurate, • Input variables readily available	• Can be employed for specific family of DESs for which the initial parameter (GC) is regressed.
ANN	• Accurate prediction, • Quick and reduces human error	• Requirement of large volume of data • No significance of physical parameter

Table 7b
Strengths and weakness of considered conductivity models.

Model	Strengths	Weakness
ARH	• Very simple in nature	• Poor estimation compared to other two models.
VFT	• Additional third parameter (T_0) accounts for the variability of activation energy for conductivity • Provides a good fitting of experimental data	• Moderate prediction accuracy and • Requires 3 parameters (an additional parameter compared to ARH model)
GH	• Can fit experimental data accurately • Powerful to correlate experimental conductivity data • Good predictive capability	• Larger number of parament • Model is dependent on density data

Acknowledgement

The authors thank the Institution of Engineers (India) research grant No. R.5/2/PG/2018–19/RDPG2018008 for their support to this research. The authors are thankful to Bharuch Enviro Infrastructure Ltd., Ankleshwar for allowing us to analyze the water content of DESs.

Supplementary materials

Supplementary material associated with this article can be found, in the online version, at doi:10.1016/j.ceja.2021.100132.

References

[1] J. Płotka-Wasylka, M. Guardia, V. Andruch, M. Vilkova, Deep eutectic solvents vs ionic liquids: similarities and differences, Microchem. J. 159 (2020) 105539, doi:10.1016/j.microc.2020.105539.
[2] M.J. Earle, K.R. Seddon, Ionic liquids. Green solvents for the future, Pure Appl. Chem. 72 (2000) 1391–1398, doi:10.1351/pac200072071391.
[3] J. Anthony, E.J. Maginn, J.F. Brennecke, Solution thermodynamics of imidazolium-based ionic liquids and water, J. Phys. Chem. B 105 (2001) 10942–10949, doi:10.1021/jp0112368.
[4] T.J. Trivedi, J.H. Lee, H.J. Lee, Y.K. Jeong, J.W. Choi, Deep eutectic solvents as attractive media for CO_2 capture, Green Chem. 18 (2016) 2834–2842, doi:10.1039/C5GC02319J.
[5] S.K. Shukla, J.P. Mikkola, Intermolecular interactions upon carbon dioxide capture in deep-eutectic solvents, Phys. Chem. Chem. Phys 20 (2018) 24591–24601, doi:10.1039/C8CP03724H.
[6] A.P. Abbott, P.M. Cullis, M.J. Gibson, R.C. Harris, E. Raven, Extraction of glycerol from biodiesel into a eutectic based ionic liquid, Green Chem. 9 (2007) 868–872, doi:10.1039/B702833D.
[7] M.A. Farajzadeh, M. Abbaspour, R. Kazemian, Synthesis of a green high density deep eutectic solvent and its application in microextraction of seven widely used pesticides from honey, J. of Chromatography A. 1603 (2019) 51–60, doi:10.1016/j.chroma.2019.06.051.
[8] A. Zeid, A.L. Othman, M.A. Habila, E. Yilmaz, E.A. Alabdullkarem, M. Soylak, A novel deep eutectic solvent microextraction procedure for enrichment, separation and atomic absorption spectrometric determination of palladium at ultra-trace levels in environmental samples, J. Measurement. 153 (2020) 107394, doi:10.1016/j.measurement.2019.107394.
[9] N. Altunay, A. Elik, S. Kaya, Alcohol-DES based vortex assisted homogenous liquid-liquid microextraction approach for the determination of total selenium in food samples by hydride generation AAS: insights from theoretical and experimental studies, Talanta 215 (2020) 120903, doi:10.1016/j.talanta.2020.120903.
[10] R.B. Leron, M.H. Li, Solubility of carbon dioxide in a eutectic mixture of choline chloride and glycerol at moderate pressures, J. Chem. Thermodyn. 57 (2013) 131–136, doi:10.1016/j.jct.2012.08.025.
[11] X. Li, M. Hou, B. Han, X. Wang, Z. Zou, Solubility of CO_2 in a choline chloride + urea eutectic mixture, J. Chem. Eng. Data. 53 (2008) 548–550, doi:10.1021/je700638u.
[12] S.Z. Abedin, F. Endres, Ionic liquids: the link to high-temperature molten salts, Acc. Chem. Res. 40 (2007) 1106–1113, doi:10.1021/ar700049w.
[13] M.C. Gutiérrez, M.L. Ferrer, L. Yuste, F. Rojo, F.D. Monte, Bacteria incorporation in deep-eutectic solvents through freeze-drying, Angew. Chem. Int. Ed. 49 (2009) 2158–2162, doi:10.1002/anie.200905212.
[14] A.P. Abbott, G. Capper, K.J. McKenzie, K.S. Ryder, Voltammetric and impedance studies of the electropolishing of type 316 stainless steel in a choline chloride based ionic liquid, Electrochim. Acta. 51 (2006) 4420–4425, doi:10.1002/anie.200905212.
[15] A.P. Abbott, K.J. McKenzie, Application of ionic liquids to the electrodeposition of metals, Phys. Chem. Chem. Phys. 8 (2006) 4265–4279, doi:10.1039/B607329H.
[16] S. Benabid, Y. Benguerba, I.M. AlNashef, N. Haddaoui, Theoretical study of physico-chemical properties of selected ammonium salt-based deep eutectic solvents, J. Mol. Liq. 285 (2019) 38–46, doi:10.1016/j.molliq.2019.04.052.
[17] Y. Geng, Z. Xiang, L.V. Cheng, N. Wang, Y. Wang, Y. Yang, Recovery of gold from hydrochloric medium by deep eutectic solvents based on quaternary ammonium salts, Hydrometallurgy 188 (2019) 264–271, doi:10.1016/j.hydromet.2019.06.013.
[18] B. Sharma, N. Singh, J.P. Kushwaha, Ammonium-based deep eutectic solvent as entrainer for separation of acetonitrile–water mixture by extractive distillation, J. Mol. Liq. 285 (2019) 185–193, doi:10.1016/j.molliq.2019.04.089.
[19] A. Ahmadi, R. Haghbakhsh, S. Raeissi, V. Hemmati, A simple group contribution correlation for the prediction of ionic liquid heat capacities at different temperatures, Fluid Phase Equilib 403 (2015) 95–103 https://doi.org/10.1016/j.fluid.2015.06.009.

[20] R. Ceriani, R. Gani, J.A. Meirelles, Prediction of heat capacities and heats of vaporization of organic liquids by group contribution methods, Fluid Phase Equilib. 283 (2009) 49–55, doi:10.1016/j.fluid.2009.05.016.
[21] Y. Chen, G.M. Kontogeorgis, J.M. Woodley, Group contribution based estimation method for properties of ionic liquids, Ind. Eng. Chem. Res. 58 (2019) 4277–4292 https://doi.org/10.1021/acs.iecr.8b05040.
[22] R.L. Gardas, J.A. Coutinho, A group contribution method for heat capacity estimation of ionic liquids, Ind. Eng. Chem. Res. 47 (2008) 5751–5757, doi:10.1021/ie800330v.
[23] R. Ge, C. Hardacre, J. Jacquemin, P. Nancarrow, D.W. Rooney, Heat capacities of ionic liquids as a function of temperature at 0.1MPa. Measurement and prediction, J. Chem. Eng. Data. 53 (2008) 2148–2153, doi:10.1021/je800335v.
[24] A.A. Strechan, Y.U. Paulechka, A.V. Blokhin, G.J. Kabo, Low temperature heat capacity of hydrophilic ionic liquids [BMIM][CF_3COO] and [BMIM][CH_3COO] and a correlation scheme for estimation of heat capacity of ionic liquids, J. Chem. Thermodyn. 40 (2008) 632–639, doi:10.1016/j.jct.2007.11.004.
[25] M. Taherzadeh, R. Haghbakhsh, A.R.C. Duarte, S. Raeissi, Estimation of the heat capacities of deep eutectic solvents, J. Mol. Liq. 307 (2020) 112940, doi:10.1016/j.molliq.2020.112940.
[26] J.O. Valderrama, G. Martinez, R.E. Rojas, Predictive model for the heat capacity of ionic liquids using the mass connectivity index, Thermochim Acta 513 (2011) 83–87, doi:10.1016/j.tca.2010.11.015.
[27] J.O. Valderrama, A. Toro, R.E. Rojas, Prediction of the heat capacity of ionic liquids using the mass connectivity index and a group contribution method, J. Chem. Thermodynamics. 43 (2011) 1068–1073, doi:10.1016/j.jct.2011.02.014.
[28] A.P. Abbott, E.I. Ahmed, K. Prasad, I.B. Qader, K.S. Ryder, Liquid pharmaceuticals formulation by eutectic formation, Fluid Phase Equilib. 448 (2017) 2–8, doi:10.1016/j.fluid.2017.05.009.
[29] A.P. Abbott, P.M. Cullis, M.J. Gibson, R.C. Harris, E. Raven, Extraction of glycerol from biodiesel into a eutectic based ionic liquid, Green Chem. 9 (2007) 868–872, doi:10.1039/B702833D.
[30] J.A.P. Coutinho, A.R. Martins, S.P. Pinho, Insights into the nature of eutectic and deep eutectic mixtures, J. Sol. Chem. 48 (2019) 962–982, doi:10.1007/s10953-018-0793-1.
[31] B. Tang, K.H. Row, Recent developments in deep eutectic solvents in chemical sciences, Monatsh. Chem. 144 (2013) 1427–1454, doi:10.1007/s00706-013-1050-3.
[32] J. Naser, F.S. Mjalli, Z.S. Gano, Molar Heat Capacity of Selected Type III Deep Eutectic Solvents, J. Chem. Eng. Data. 61 (2016) 1608–1615, doi:10.1021/acs.jced.5b00989.
[33] K.R. Siongco, R.B. Lerona, A.R. Caparanga, M.H. Li, Molar heat capacities and electrical conductivities of two ammonium-based deep eutectic solvents and their aqueous solutions, Thermochim Acta 566 (2013) 50–56, doi:10.1016/j.tca.2013.05.023.
[34] F. Chemat, H. Anjum, A.M. Shariff, P. Kumar, T. Murugesan, , Thermal and physical properties of (choline chloride + urea + L-arginine) deep eutectic solvents, J. Mol. Liq. 218 (2016) 301–308, doi:10.1016/j.molliq.2016.02.062.
[35] A. Bazyleva, J. Abildskov, A. Anderko, et al., Good reporting practice for thermophysical and thermochemical property measurements (IUPAC Technical Report), Pure Appl. Chem. 93 (2021) 253–272, doi:10.1515/pac-2020-0403.
[36] A.F. Arkawazi, A.A. Barzinjy, S.M. Hamad, Physical, thermal and structural properties of 1 choline chloride: 2 urea based ionic liquids, Singapore J. Sci. Res. 10 (2020) 417–424, doi:10.3923/sjsres.2020.417.424.
[37] J. Luo, O. Conrad, I.F.J. Vankelecom, Physicochemical properties of phosphonium-based and ammonium-based protic ionic liquids, J. Mater. Chem. 38 (2012) 20574–20579, doi:10.1039/C2JM34359B.
[38] B.H. Stuar, Infrared Spectroscopy: Fundamentals and Applications, John Wiley and Sons Ltd, England, 2005.
[39] O. Saoudi, N. Ghaouara, T. Othman, Electrical conductivity-viscosity correlation for the solution of the laccase from Trametes versicolor, J. Mol. Liq. 246 (2017) 149–152, doi:10.1016/j.molliq.2017.09.062.
[40] H. Ghaedi, M. Ayoub, S. Sufian, S.M. Hailegiorgis, G. Murshid, S.N. Khan, Thermal stability analysis, experimental conductivity and pH of phosphonium-based deep eutectic solvents and their prediction by a new empirical equation, J. Chem. Thermodynamics. 116 (2018) 50–60, doi:10.1016/j.jct.2017.08.029.
[41] H.Z. Su, J.M. Yin, Q.S. Liu, C.P. Li, Properties of four deep eutectic solvents: density, electrical conductivity, dynamic viscosity and refractive index, Acta Phys. -Chim. Sin. 31 (2015) 1468–1473, doi:10.3866/PKU.WHXB201506111.
[42] A.R. Harifi-Mood, R. Buchner, Density, viscosity, and conductivity of choline chloride + ethylene glycol as a deep eutectic solvent and its binary mixtures with dimethyl sulfoxide, J. Mol. Liq. 225 (2017) 689–695, doi:10.1016/j.molliq.2016.10.115.
[43] J.O. Valderrama, P.A. Robles, Critical properties, normal boiling temperatures, and acentric factors of fifty ionic liquids, Ind. Eng. Chem. Res. 46 (2007) 1338–1344, doi:10.1021/ie0603058.
[44] H. Knapp, R. Doring, I. Oellrich, U. Plocker, J.M. Prausnitz, Vapor-liquid equilibria for mixtures of low boiling substances, DECHEMA Chem. Data Ser. 4 (1982).
[45] J.O. Valderrama, R.E. Rojas, Mass connectivity index, a new molecular parameter for the estimation of ionic liquid properties, Fluid Phase Equilib 297 (2010) 107–112, doi:10.1016/j.fluid.2010.06.015.
[46] G. Sodeifian, S.A. Sajadian, N.S. Ardestani, Evaluation of the response surface and hybrid artificial neural network-genetic algorithm methodologies to determine extraction yield of Ferulago angulata through supercritical fluid, J. Taiwan Inst. Che. Eng. 60 (2016) 165–173, doi:10.1016/j.jtice.2015.11.003.
[47] G. Sodeifian, S.A. Sajadian, N.S. Ardestani, Optimization of essential oil extraction from Launaea acanthodes Boiss: utilization of supercritical carbon dioxide and cosolvent, J. Supercrit. Fluids, 116 (2016) 46–56. https://doi.org/10.1016/j.supflu.2016.05.015.
[48] F.S. Mjalli, J. Naser, B. Jibril, S.S. Al-Hatmi, Z.S. Gano, Ionic liquids analogues based on potassium carbonate, Thermochim. Acta 575 (2014) 135–143.
[49] M. Hayyan, T. Aissaoui, M.A. Hashim, M.A. AlSaadi, A. Hayyan, Triethylene glycol based deep eutectic solvents and their physical properties, J. Taiwan Inst. Chem. Eng. 50 (2015) 24–30, doi:10.1016/j.tca.2013.10.028.
[50] M.K. AlOmar, M. Hayyan, M.A. Alsaadi, S. Akib, A. Hayyan, M.A. Hashim, Glycerol based deep eutectic solvents: physical properties, J. Mol. Liq. 215 (2016) 98–103, doi:10.1016/j.jtice.2015.03.001.
[51] G. Bagh, K. Shahbaz, F.S. Mjallic, I.M. AlNashef, M.A. Hashima, Electrical conductivity of ammonium and phosphonium based deep eutectic solvents: measurements and artificial intelligence-based prediction, Fluid Phase Equilib. 356 (2013) 30–37, doi:10.1016/j.fluid.2013.07.012.
[52] K. Shahbaz, F.S. Mjalli, M.A. Hashima, I.M. AlNashef, Prediction of deep eutectic solvents densities at different temperatures, Thermochim Acta 515 (2011) 67–72, doi:10.1016/j.tca.2010.12.022.
[53] M.R.G. Farnoush Faridbod, P. Norouzi, S. Riahi, H. Rashedi, Application of room temperature ionic liquids, in: A. Kokorin (Ed.), Electrochemical Sensors and Biosensors, Ionic Liquids, Applications and Perspectives, 2011, doi:10.5772/14702.